The Astrophysical Journal Supplement Series, 230:23 (38pp), 2017 June https://doi.org/10.3847/1538-4365/aa72ed

The Extended IRTF Spectral Library: Expanded Coverage in Metallicity, Temperature, and Surface Gravity

Alexa Villaume[1], Charlie Conroy[2], Benjamin Johnson[2], John Rayner[3], Andrew W. Mann[4], and Pieter van Dokkum[5]
[1] Department of Astronomy and Astrophysics, University of California, Santa Cruz, CA 95064, USA; avillaum@ucsc.edu
[2] Harvard-Smithsonian Center for Astrophysics, Cambridge, MA 02138, USA
[3] Institute for Astronomy, University of Hawaii, Honolulu, HI 96822, USA
[4] The University of Texas at Austin, Austin, TX, USA
[5] Yale University Astronomy Department, New Haven, CT 06511, USA
Received 2016 December 13; revised 2017 May 10; accepted 2017 May 11; published 2017 June 16

Abstract

We present a 0.7–2.5 μm spectral library of 284 stars observed with the medium-resolution infrared spectrograph, SpeX, at the 3.0 m NASA Infrared Telescope Facility (IRTF) on Maunakea, Hawaii. This library extends the metallicity range of the IRTF Cool Star library beyond solar metallicity to $-1.7 < [\mathrm{Fe/H}] < 0.6$. All of the observed stars are also in the MILES optical stellar library, providing continuous spectral coverage for each star from 0.35 to 2.5 μm. The spectra are absolute flux calibrated using Two Micron All Sky Survey photometry, and the continuum shape of the spectra is preserved during the data reduction process. Synthesized JHK_S colors agree with observed colors at the 1%–2% level, on average. We also present a spectral interpolator that uses the library to create a data-driven model of spectra as a function of T_{eff}, log g, and [Fe/H]. We use the library and interpolator to compare empirical trends with theoretical predictions of spectral feature behavior as a function of stellar parameters. These comparisons extend to the previously difficult to access low-metallicity and cool dwarf regimes, as well as the previously poorly sampled super-solar metallicity regime. The library and interpolator are publicly available.

Key words: atlases – galaxies: stellar content – infrared: stars – planets and satellites: fundamental parameters – stars: fundamental parameters – techniques: spectroscopic

1. Introduction

Stellar libraries, whether empirical or theoretical, are foundational to several different fields of astrophysics. In stellar population synthesis (SPS) models, stellar libraries are needed to convert the stellar evolution predictions of stellar parameters of effective temperature (T_{eff}), surface gravity (log g), and metallicity ([Fe/H]) into spectral energy distributions (Conroy 2013). Stellar spectra can be used to compute the line-of-sight velocity distributions in galaxies (Cappellari & Emsellem 2004; Emsellem et al. 2004). Well-characterized stellar spectra are also a key ingredient in exoplanet studies (e.g., Newton et al. 2014; Mann et al. 2015).

The goal for any stellar library is extensive coverage in stellar parameter space and large wavelength coverage at comparable or better resolution than typical observations to which they are compared. Large wavelength coverage is important because different wavelength regimes probe different stellar populations in the integrated light of galaxies. The optical is the most well-studied wavelength regime but there is important information that is only available in other regimes. For example, the ultraviolet (UV) probes the populations of hot, massive stars (e.g., Vazdekis et al. 2016, and the references therein), and the near-infrared (IR) probes the populations of cool, evolved stars such as those on the asymptotic giant branch (Athey et al. 2002; Martini et al. 2013; Villaume et al. 2015; Simonian & Martini 2016). Furthermore, the endeavor to characterize biological signatures of exoplanets must consider the effect and characteristics of the host stars, which requires UV–IR coverage (France et al. 2015). Moreover, uniform coverage in parameter space is also necessary to ensure accurate stellar population models. Unfortunately, there is still no single stellar library that covers the entire range of wavelength and parameter space.

Empirical stellar libraries have been available for over 30 years (e.g., Gunn & Stryker 1983; Pickles 1985; Diaz et al. 1989; Silva & Cornell 1992; Pickles 1998; Worthey et al. 1994; Jones 1999; Lançon & Wood 2000; Cenarro et al. 2001; Prugniel & Soubiran 2001; Le Borgne et al. 2003; Valdes et al. 2004; Sánchez-Blázquez et al. 2006; Mármol-Queraltó et al. 2008; Rayner et al. 2009; Ardila et al. 2010; Sharon et al. 2010). A key limitation of existing stellar libraries is their often limited coverage in stellar parameter space. This is in some respects a fundamental problem because not all stars of interest are close enough to enable detailed observations (e.g., hot metal-poor stars). Standard observational constraints such as atmospheric absorption and sky emission, which is especially prominent in the IR, flux calibration, wavelength coverage, and spectral resolution further challenge the development of comprehensive empirical stellar libraries.

Theoretical libraries offer the advantage of dense coverage in parameter space, arbitrarily high spectral resolution, and no need to correct for atmospheric absorption or flux calibration (e.g., Coelho et al. 2005; Martins et al. 2005; Munari et al. 2005). However, theoretical stellar libraries are only as good as the available atomic and molecular line lists and the approximations made in computing the models, e.g., the assumption of local thermodynamic equilibrium (LTE) and 1D plane-parallel atmospheres. The effect of non-LTE is generally taken into account where it matters most (e.g., hot stars and metal-poor stars, Lanz & Hubeny 2003; Lind et al. 2012) and some 3D theoretical models (e.g., Magic et al. 2013) have begun to emerge, but these techniques have not been widely adopted because they are very expensive computationally. Theoretical stellar spectra are most unreliable for very cool

stars and very hot stars (Allard et al. 1997; Martins & Coelho 2007; Bertone et al. 2008; Allard et al. 2013; Rajpurohit et al. 2014, 2016). The former is a particularly acute problem for both exoplanet and galaxy studies. All the habitable zone planes found by *TESS* will be around M dwarfs (France et al. 2015), and counting cool dwarf stars in the absorption lines of integrated spectra of galaxies has emerged as a way to constrain the initial mass function (Spinrad 1962; Wing & Ford 1969; Cohen 1978; Frogel et al. 1978; Kleinmann & Hall 1986; Diaz et al. 1989; Ivanov et al. 2004; Conroy & van Dokkum 2012) in unresolved stellar populations. The limitations of the theoretical stellar spectra in the cool star regime makes it necessary to turn to empirical stellar libraries.

Sánchez-Blázquez et al. (2006) created a landmark empirical optical stellar library, the MILES library. The MILES library, consisting of nearly 1000 stars, covers a wide range of stellar parameter space over the wavelength range 0.35–0.75 μm. The MILES library enabled the creation of more precise SPS models, which in turn facilitated a greater understanding of galaxies beyond the reach of resolved stellar population studies.

However, as stated previously, the optical window does not contain a complete picture of a stellar population. A major advance occurred with the release of the Rayner et al. (2009) Infrared Telescope Facility (IRTF) spectral library. The creation of this near-IR library was a great step forward for SPS models (e.g., Conroy & van Dokkum 2012; Spiniello et al. 2012; Meneses-Goytia et al. 2015; Röck et al. 2016). A limitation of the IRTF stellar library is its narrow stellar parameter range, all stars have approximately solar metallicity. Furthermore, there is very little overlap in the stars between the MILES and IRTF stellar libraries. The X-Shooter Spectral Library is observing many stars with continuous spectral coverage from 0.35 to 2.5 μm and will be another valuable library once it is complete (e.g., Chen et al. 2014).

In this work we present the Extended IRTF Library. The extension is twofold: we expanded the metallicity coverage to $-1.7 < [\mathrm{Fe/H}] < 0.6$, a large expansion from the just solar-metallicity coverage of the original IRTF library, and we selected all of our objects from the MILES stellar library to provide continuous coverage from the optical through near-IR. In addition to the new stellar library, we also present an interpolator that uses a data-driven model created from the new stellar library. The interpolator generates a stellar spectrum as a function of $T_{\rm eff}$, $\log g$, and [Fe/H]. This interpolator provides smooth variation in stellar spectra across the parameter space and is an important component in the creation of stellar population models.

The rest of this paper is organized in the following manner: Section 2 details our sample selection, observational strategy, data reduction, and characteristics of the objects and data. In Section 3 we describe our interpolator and assess its quality. In Section 4 we explore the behavior of the library and the interpolator and compare both to theoretical predictions. Finally, in Section 5 we summarize the main points of this work.

2. The Extended IRTF Library

2.1. Sample Selection

We selected our target stars from the MILES stellar library (Sánchez-Blázquez et al. 2006), avoiding known spectroscopic binary stars, to provide continuous coverage from the optical to the near-IR. We selected our targets to span stellar parameters that would enable the creation of stellar population models for intermediate and old population ages as determined with stellar isochrones from the MIST project (Choi et al. 2016) .

In Figure 1 we compare the MILES coverage in $T_{\rm eff} - \log g$ space and the stars observed with IRTF for this work. Each panel shows the stars in a given metallicity bin where the stars from the MILES library are represented as blue circles and the stars observed for this library are represented as red circles. Each panel also displays 13.5 Gyr (black line) and 3 Gyr (gray line) MIST isochrones. Selecting targets by eye, we achieved relatively uniform coverage along the intermediate-age isochrones for all but the lowest metallicity bins and the old-age isochrones across all the metallicity bins. In particular, we have well-sampled turn-offs for all except the intermediate-age low-metallicity stellar tracks. The metallicity distribution of the library is summarized in panel f of Figure 1.

Throughout this work we use the stellar parameters determined by Prugniel et al. (2011) and Sharma et al. (2016) instead of those reported by Cenarro et al. (2007). The stellar parameters determined by Cenarro et al. (2007) were determined heterogeneously, depending on which additional literature data were available for a given star. As a result, the stellar parameters from Cenarro et al. (2007) vary in quality and trustworthiness. Prugniel et al. (2011) sought to revise the stellar parameters of the stars in the MILES library in a more robust and homogeneous way. They used ELODIE spectra to perform full-spectrum χ^2 minimization fits (Koleva et al. 2009) between the MILES spectra and templates built from the ELODIE 3.2 library (Wu et al. 2011). Sharma et al. (2016) revised the stellar parameter values of MILES library stars with $T_{\rm eff} < 4800$ K with an improved interpolator.

It is important to note that the accuracy of SPS models is predicated upon the accuracy of the stellar parameters. Percival & Salaris (2009) found that a change of 100 K in the effective temperature of stars in a stellar library can propagate into a 20% error in absolute ages estimated from stellar population models. Furthermore, derived exoplanet properties are a direct function of the stellar parameters of the host star (e.g., Mann et al. 2015). These examples underly the need for accurate stellar parameters in empirical stellar libraries.

We do not make use of the Rayner et al. (2009) library (except for comparison with reobserved stars) for two reasons. First, as we we discuss later, the detectors on SpeX have been upgraded since the IRTF library of Rayner et al. (2009). A significant component of the upgrade included a blueward extension to 0.70 μm. The original IRTF library had a blue cutoff of 0.8 μm, which meant that there was no overlap with the red cutoff of the MILES library. Second, there were few stars that were in both the MILES stellar library and the Rayner et al. (2009) library. Our requirement for continuous coverage from the optical to the near-IR for a common set of stars led us to eschew the original IRTF library.

2.2. Observations

We carried out 24 nights of observations from 2014 August to 2016 June using the upgraded SpeX instrument on IRTF. For details on SpeX we refer the reader to Rayner et al. (2003). In short, SpeX is a medium-resolution cross-dispersed spectrograph equipped with a 2048 × 2048 Hawaii-2RG array. All stars were observed in the short-wavelength

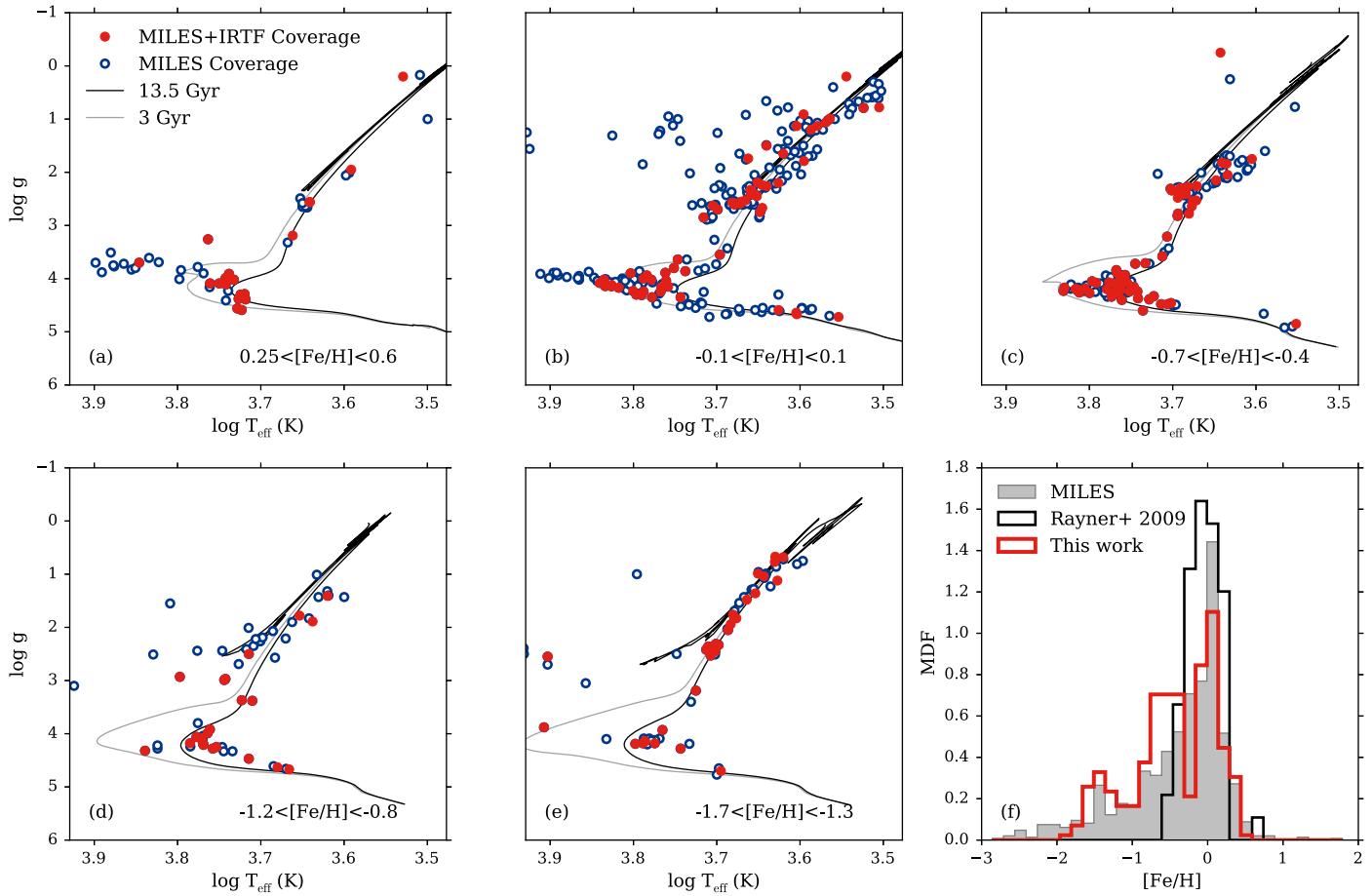

Figure 1. (Panels a-e) Comparison of the MILES spectral library (blue) with the library presented in this work (red). All the stars in this work were selected from the MILES library. Stars were chosen to sample isochrones spanning from 3 Gyr (gray line) to 13.5 Gyr (black line) with metallicities [Fe/H] = 0.25, 0.00, −0.50, −1.00, and −1.50. (f) Comparison of the metallicity density functions (MDFs) of the MILES spectral library (solid gray), the Rayner et al. (2009) (black line), and the library presented in this work (red line). The different libraries have different total numbers of stars, so the MDFs were normalized such that the integral over the range of metallicity values is 1 for each library, indicating the probability at any given metallicity value that a given star has this metallicity for each library.

cross-dispersed mode (SXD) using the 0.″3 (2 pixel) slit, providing a nominal resolving power of $R \sim 2000$. We observed every star at the parallactic angle. The upgraded detectors extended the wavelength coverage further into the blue, giving a wavelength range from 0.7 to 2.55 μm. The upgraded detectors also remove the 0.06 μm gap that used to exist between the *H* and *K* bands (Rayner et al. 2009).

An A0 V star (or a star of similar spectral type) was observed either before or after each science object to correct for absorption due to the Earth's atmosphere and to flux calibrate the science object spectra. For most stars the airmass difference between the target star and the standard star was smaller than 0.1. Standard stars were also chosen to be located within 10 degrees of the target object whenever possible to minimize the effects of any differential flexure in the instrument between the observations of the target and standard. Owing to a shortage of standard stars near some targets, in a few cases airmass differences between the two reached 0.15.

We took a set of internal flat field and argon arc lamp exposures with each target-standard pair. This procedure helps minimize the possible effects of flexure of the detector on the quality of the flat-fielding and the final wavelength solution.

A table summarizing the content of the library including the object names, K_S-band magnitudes, associated telluric standard stars, and various other characteristics for all the 284 library stars is presented in Table 2.

2.3. Data Reduction

Data were reduced following the same procedure as described in Rayner et al. (2009) using the facility IDL-based reduction package for SpeX, Spextool v4.0.4 (Cushing et al. 2004). Cushing et al. (2004) provide a comprehensive explanation of the data reduction process, and so here we summarize and highlight the main steps.

The science images were processed by correcting for nonlinearity, subtracting the pairs of images taken at two different slit positions, and dividing the pair-subtracted images by a normalized flat field. Any residual sky signal left over from the pair subtraction is removed from the image, and the spectra in individual orders were then optimally extracted. Argon lines were used to wavelength calibrate the data. For the SXD observing mode, several arc exposures are combined to increase the signal-to-noise ratio (S/N).

We used the A0 V standard star observed with each science object to correct for the telluric absorption and flux calibrate the science object using the method described by Vacca et al. (2003). In brief, the method uses a theoretical spectrum of Vega to determine the intrinsic spectrum of any A0 V star by scaling

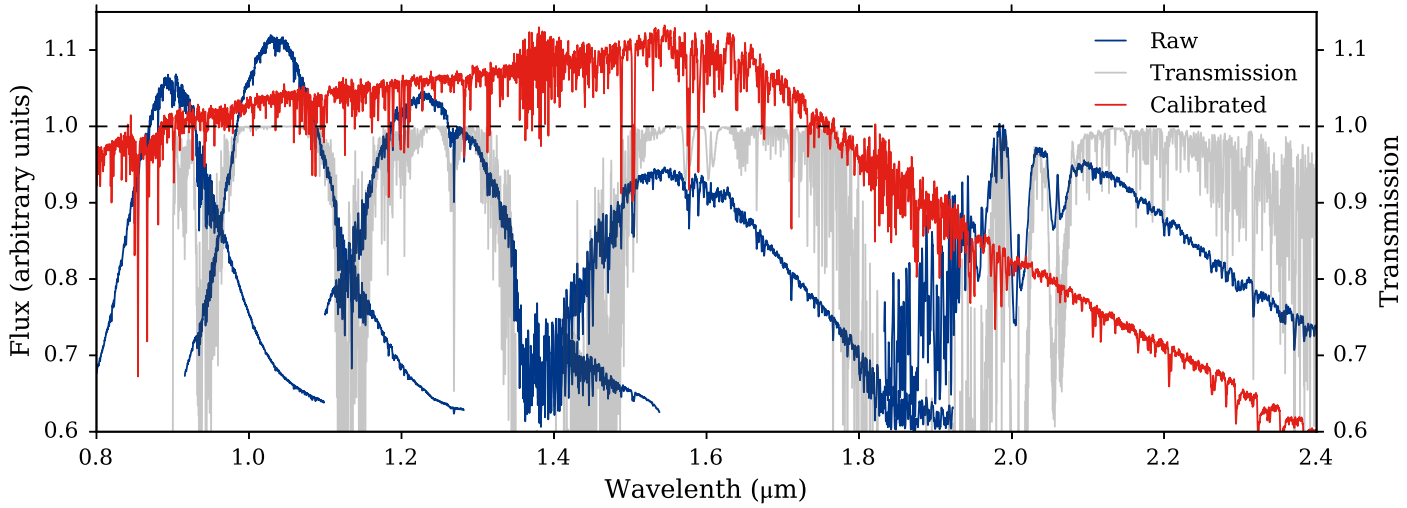

Figure 2. Demonstration of the telluric correction for the star BD+053080. We show the atmospheric transmission spectrum (gray), the spectrum for BD+053080 before the telluric correction (blue), and the spectrum after telluric correction and flux calibration (red).

and reddening the Vega model to match the near-IR magnitudes of the observed A0 V stars and modifying the model to account for differences in line strengths, radial and rotational velocities, and spectral resolution. This method also corrects for instrument throughput and flux calibrates the spectra of the target stars.

In Figure 2 we show the SpeX spectrum for the library star BD +0503080 before (blue) and after (red) the telluric correction. The before and after spectra have been vertically scaled to clarify the comparison. Also shown is atmospheric transmission at Mauna-kea for an airmass of 1.5 and precipitable water vapor of 3 mm (Lord 1992). The before spectrum has areas of very low signal and features in wavelength regions that align with the deepest parts of absorption in the atmospheric transmission spectrum. The red line demonstrates that much of the noise in this region is decreased after the telluric correction. We subsequently mask the regions in the IRTF spectra where the atmospheric absorption is most prominent, 1.32–1.41 μm and 1.82–1.94 μm.

This telluric correction procedure is quite effective in removing the effects of the atmosphere. However, A0 V stars have prominent hydrogen absorption lines and weak metal features, which can complicate the telluric correction. In Figure 3 we show a theoretical spectrum of an A0 V star (purple) comparef to an atmospheric transmission (black, the model for the first three panels is from Lord 1992 and the model for the fourth panel is from Clough et al. 2005) and an example of a telluric spectrum used to correct the library stars (gray). The A0 V and transmission spectra have both been degraded to a resolution of $R \equiv 2000$. The top panel shows the region around the Paschen break, which can be particularly difficult to fit with models at the percent level. We also see that there are features in the telluric spectrum that are likely spurious and are associated with the metal lines in A0 V stars. We have labeled several of the metal features in Figure 3. Our telluric correction method also relies on modeling and removing the A0 V spectrum by modifying the model spectrum of Vega to match the A0 V star. This method is better than interpolating over the hydrogen lines, as there are telluric features at those wavelengths, but there are imperfections to this process. We address the uncertainties associated with these difficulties shortly. The telluric correction appears to be well behaved in regions away from hydrogen lines and the weak metal lines.

After the telluric correction, the spectra extracted from different orders were merged into a single continuous spectrum. In Rayner et al. (2009) an additional scale factor was needed to match the flux levels of the different orders but the updates to the SpeX detector made this step unnecessary. All wavelengths are in vacuum. Spextools provides a measure of uncertainty for each reduced spectrum and the typical formal S/N of the library is very high with a mean value ∼500. However, the quoted S/N only includes statistical (photon counting) uncertainty, not correlated noise or any source of systemic uncertainty. Most importantly, we are interested in the uncertainty our telluric correction method introduces (see above).

To empirically measure the uncertainty of the library stars, we compare five stars with repeat observations: HD 007106, HD 021197, HD 138776, HD 201891, and HD 204613. For all of these observations we followed the same observing and reduction strategies as described above. The repeat observations were made with the same standard star. We computed the difference between the normalized spectra of the same star and divided by a factor of $\sqrt{2}$ (black line in Figure 4). The Poisson uncertainty is the inverse of the wavelength-dependent average of the S/N for each pair of target observations (red line in Figure 4).

While Figure 4 demonstrates that the Poisson uncertainty underpredicts the empirical uncertainty for most of the wavelength range, the empirical uncertainty is almost always ∼0.2%–0.3%. The exceptions to this are in regions that are heavily affected by telluric absorption (upper right and lower left panels) or where there are many broad hydrogen absorption and metal lines in the A0 V standard stars (upper left panel). Still, even in these regions the uncertainty is 1%–2%.

The empirical uncertainty presented here encompasses differences in weather and/or observing conditions, potential human error in the reduction process, and correlated noise. It does not assess the uncertainty associated with using different standard stars or using different techniques for telluric correction (e.g., van Dokkum & Conroy 2012; Kausch et al.

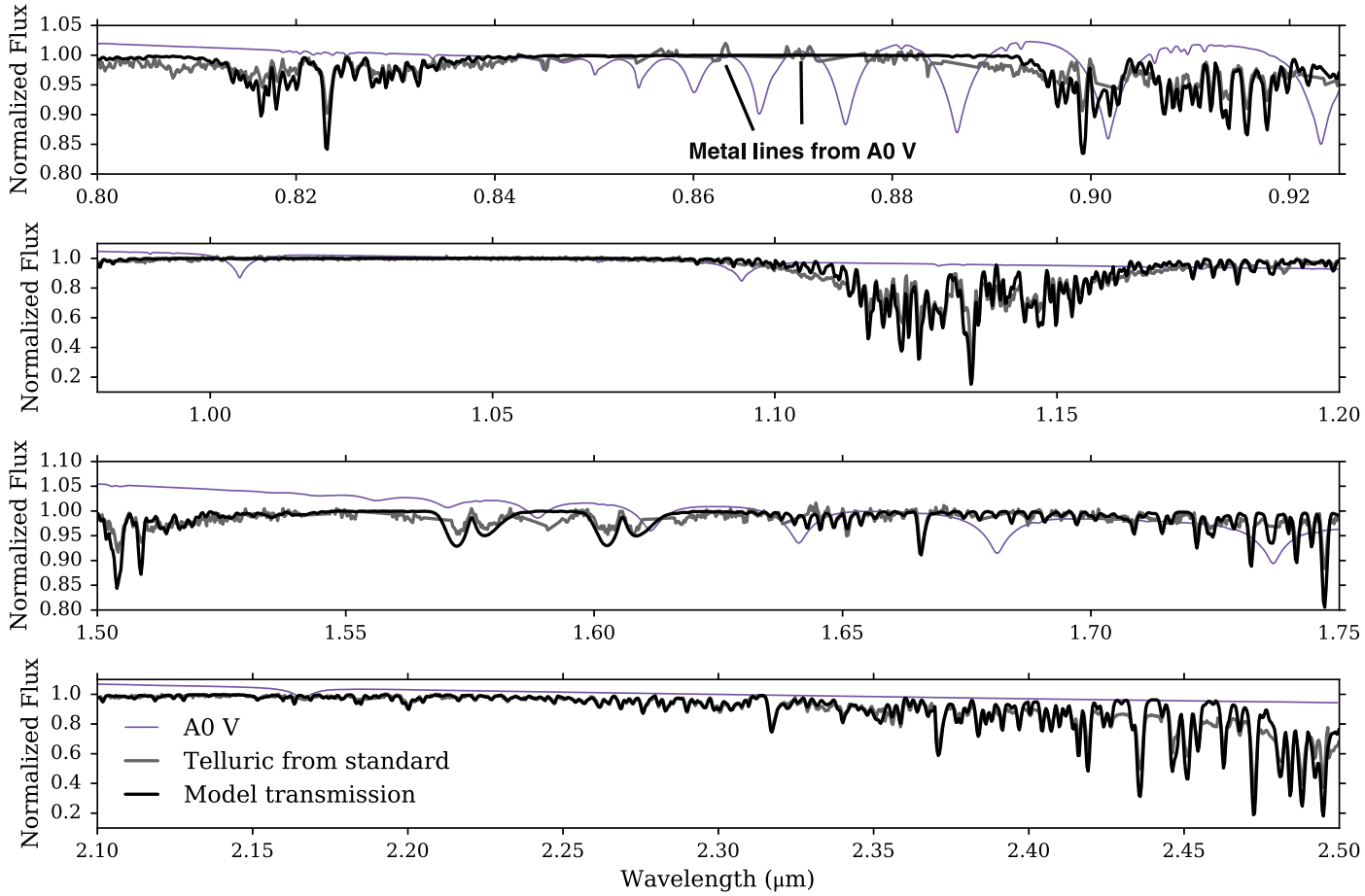

Figure 3. Comparison of a theoretical atmospheric transmission spectrum (black) to an example of a telluric spectrum (gray) used to telluric correct the library spectra and a theoretical spectrum of an A0 V star (purple). In regions of the A0 V spectrum containing strong hydrogen and metallic lines (top panel), the telluric spectrum includes unphysical features. We indicate a few of these features introduced by the metal lines in the A0 V stars in the top panel. Note that no attempt was made to fit the model transmission spectrum to the observations; the model is meant only to guide the eye.

2015). It is not known whaich effect using a different telluric correction technique would have on the quality of SpeX spectra. Assessing the impact of these additional sources of uncertainty is beyond the scope of this work, but will be pursued in the future.

To demonstrate the quality of the individual features, noise in the continuum after the full reduction, and qualitative metallicity trends, we show a sequence of stars ordered by metallicity over the *IYJHK* photometric bands in Figures 5–9. The left panel shows stars roughly on the main-sequence turn-off, and the right panel shows stars roughly on the subgiant branch. We highlight a selection of prominent lines in each bandpass. We qualitatively see general trends with metallicity. However, we are not completely controlling for temperature and surface gravity effects, and so it is difficult to say anything definitively about potential trends. In Section 4 we look at equivalent-width trends as a function of temperature and surface gravity.

2.3.1. Correcting to Restframe Wavelength

We used the code `Prospector` (B. Johnson et al. 2017, in preparation)[6] to determine line-of-sight velocities for each star, which were used to correct the final reduced spectra to the restframe. Prospector is a code for inference of physical parameters from spectroscopic data via Markov chain Monte Carlo (MCMC) sampling of the posterior probability distributions. To obtain estimates of the posterior velocity distribution using Prospector, a spectral model is constructed for each star by linearly interpolating the C3K theoretical spectral models[7] to the Prugniel et al. (2011) and Sharma et al. (2016) parameters, which are then broadened to the resolution of IRTF. At each MCMC step, this spectrum is shifted in velocity, and the likelihood of the data given the redshifted model is calculated after masking regions of strong telluric lines.

2.4. Flux Calibration

To deredden the flux-calibrated spectra, we used the $E(B-V)$ values given in the MILES stellar library (P. Sánchez-Blázquez 2017, private communication),

$$f_{\lambda}^{\rm cor}(\lambda) = f_{\lambda}(\lambda) \times 10^{(0.4 \times A_{\lambda})}, \quad (1)$$

where $f_{\lambda}(\lambda)$ is the observed spectrum and A_{λ} is the extinction law as a function of wavelength. We adopted the near-IR law

[6] https://github.com/bd-j/prospector

[7] This is the theoretical library described in Conroy & van Dokkum (2012) with some minor updates to the line lists.

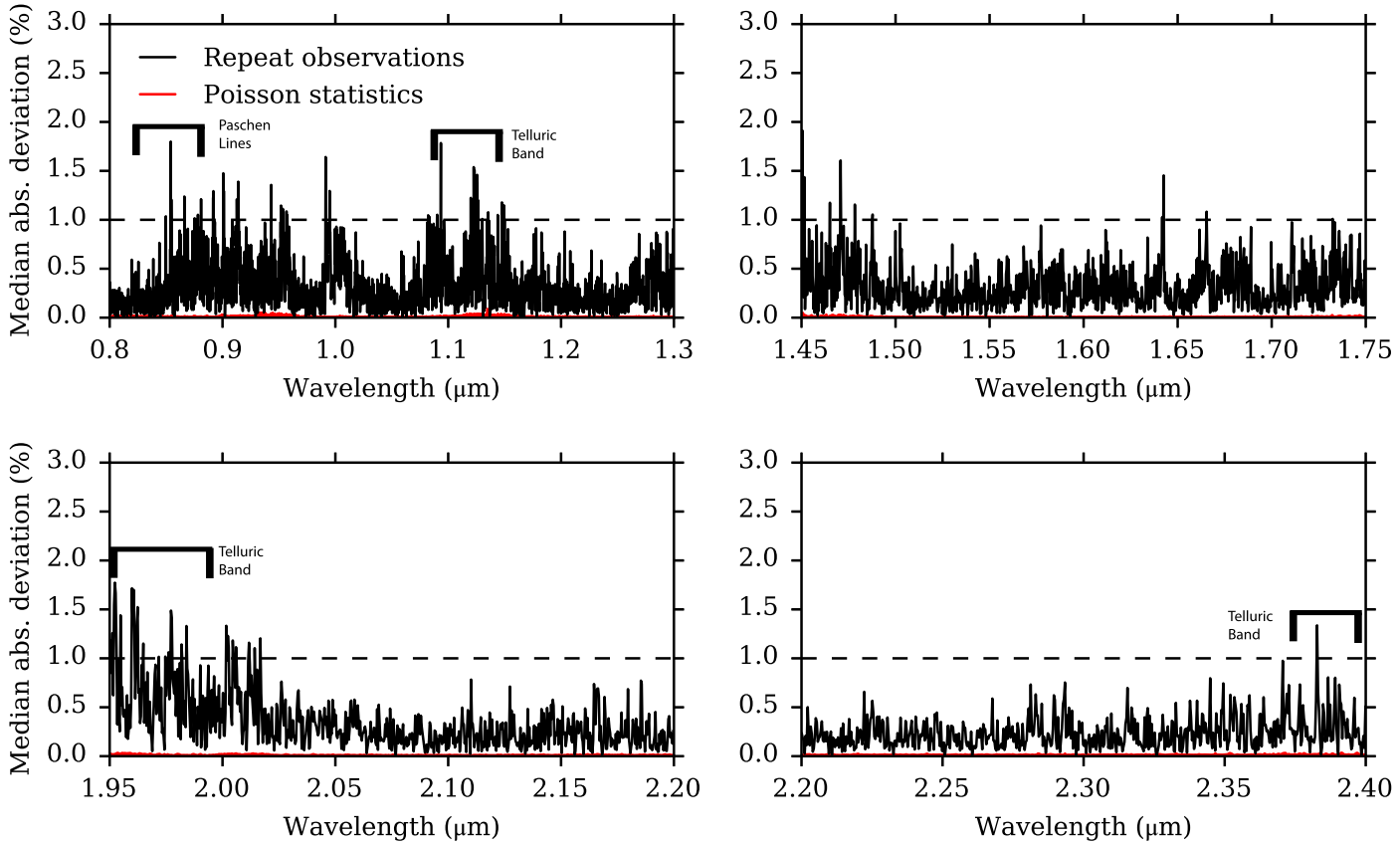

Figure 4. Comparison of the median absolute deviation of the Poisson and empirical uncertainty values of five library stars with repeat observations with the same standard star. We indicate the 1% uncertainty with the dashed line as a guide. The Poisson uncertainty is ∼0.2% throughout the wavelength range and underpredicts the empirical uncertainty (difference between the two observations), but nonetheless, the median empirical uncertainty is generally <1%. The regions where the uncertainty exceeds 1% are regions contaminated by telluric absorption or where there exist prominent hydrogen absorption features in the A0 V standard stars.

given by Fitzpatrick & Massa (2007) with $R_V = 3.1$,

$$A_\lambda = 1.056 \times E(B-V)\lambda^{-1.84}. \quad (2)$$

The MILES spectra were dereddened using the same $E(B-V)$ values.

We absolutely flux calibrated the IRTF spectra using a correction factor based on 2MASS JHK_S photometry. We computed the correction factor for each star by using the reported 2MASS magnitude, μ, and error, σ, to create a random normal distribution for each bandpass, $\mathcal{N}(\mu, \sigma^2)_{X_{\rm obs}}$, where X denotes a given bandpass. We created a distribution of calibration factors using the following expression,

$$f(C_X) = 10^{(X_{\rm syn} - \mathcal{N}_{X_{\rm obs}})/2.5}, \quad (3)$$

$X_{\rm syn}$ is the AB synthetic magnitude computed from the spectrum. The observed spectrum for each star is multiplied by a single correction factor,

$$\langle C \rangle = \frac{\sum_X w_X {\rm Peak}[f(C_X)]}{\sum_X w_X}, \quad (4)$$

where the weight, w_X, is the inverse variance given by the 1σ deviations from $f(C_X)$, and Peak$[f(C_X)]$ is the peak of the distribution of calibration factors. As in Rayner et al. (2009), this scaling has the effect of shifting the entire spectrum up or down so that the overall absolute flux level is correct, while simultaneously preserving the relative flux calibration of each spectral order derived from the observations and telluric correction procedures.

The publicly available MILES spectra are normalized to unity, so in addition to absolutely flux calibrating the IRTF spectra, we needed to absolutely flux calibrate the MILES spectra. We corrected the MILES spectra in a similar manner to the IRTF spectra using the average of the available BV photometry. We preferentially used Tycho (Høg et al. 2000b, 2000a) $B_T V_T$ photometry, and for stars where that is not available, we used Johnson BV photometry taken from Simbad. However, uncertainties in the observed photometry and the different epochs at which the optical and near-IR photometry were taken means that for most stars this correction of the IRTF and MILES spectra does result in perfect agreement in the overlap region. Since we are eventually going to stitch the two spectra together, we need them to be at the same flux level, and any incongruity would affect the derived bolometric luminosities and spectral shapes around 0.7 μm. We forced the MILES and IRTF spectra by computing the percent difference of the flux in the overlap region assuming that the IRTF spectra are at the correct level. Then, to ensure that the flux does not move into the negative, if the difference was negative, we shifted the IRTF spectrum by that factor. If the difference was positive, we shifted the MILES spectrum by that factor.

When no 2MASS photometry is available (e.g., HD 134439) but near-IR photometry from Simbad exists, we used the same basic method as described above, but only considered the K_S-band photometry, using the raw difference between the observed and

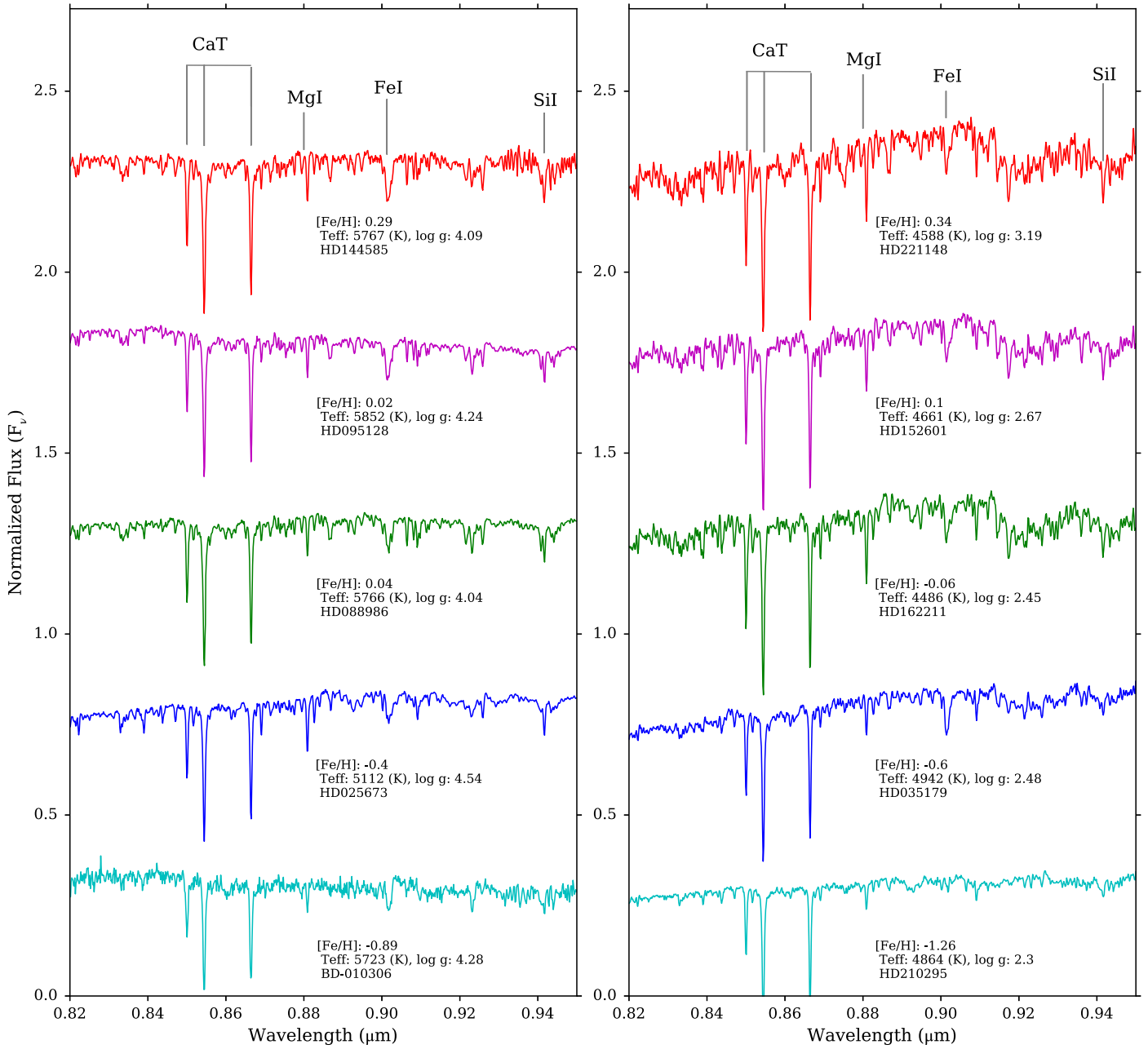

Figure 5. Sequence of stars on the main-sequence turn-off (left) and subgiant branch (right) plotted as a function of metallicity over the *I* band (0.82–0.95 μm). The spectra have been divided by the median flux value over the wavelength region shown and are offset by constants.

synthetic magnitudes. For variable stars in the sample, the absolute flux calibration is only approximate since the 2MASS photometry was obtained at an earlier epoch than the SpeX spectroscopy. However, consistency between the MILES spectra and IRTF spectra is a natural check of the calibration.

2.4.1. Quality of Flux Calibration

We assess the quality of the spectral shape of the IRTF spectra in Figure 10. Here we show a histogram of the error-normalized color differences between the observed and synthesized 2MASS (Skrutskie et al. 2006) $J - H$ (left), $H - K_S$ (middle), and $J - K_S$ (right) colors. We also show in each panel of Figure 10 a Gaussian distribution of $\sigma = 1$. Overall, the differences between observed and synthesized colors are consistent with the errors in the observed colors. There is some tension in the $J - H$ and $H - K_S$ colors but not in $J - K_S$, suggesting that there might be some modest issue with the *H*-band normalization.

We further examine the quality of the flux calibration by computing the residuals between observed and synthetic photometric colors. For this exercise we choose stars with 2MASS photometry better than 3% for the JHK_S bands and with good quality spectra and well-determined stellar parameters (see Table 2 and later for how we determine this); 124 stars in total. In Figure 11 we show these residuals as a function of effective temperature for the colors $H - K_S$ (upper right), $J - K_S$ (lower left), $B_T - V_T$ (we only display stars with Tycho photometry in this plot) and $V_T - K_S$ (lower right). The observed photometry have been reddened corrected using the same $E(B - V)$ values used to correct the spectra. Points are

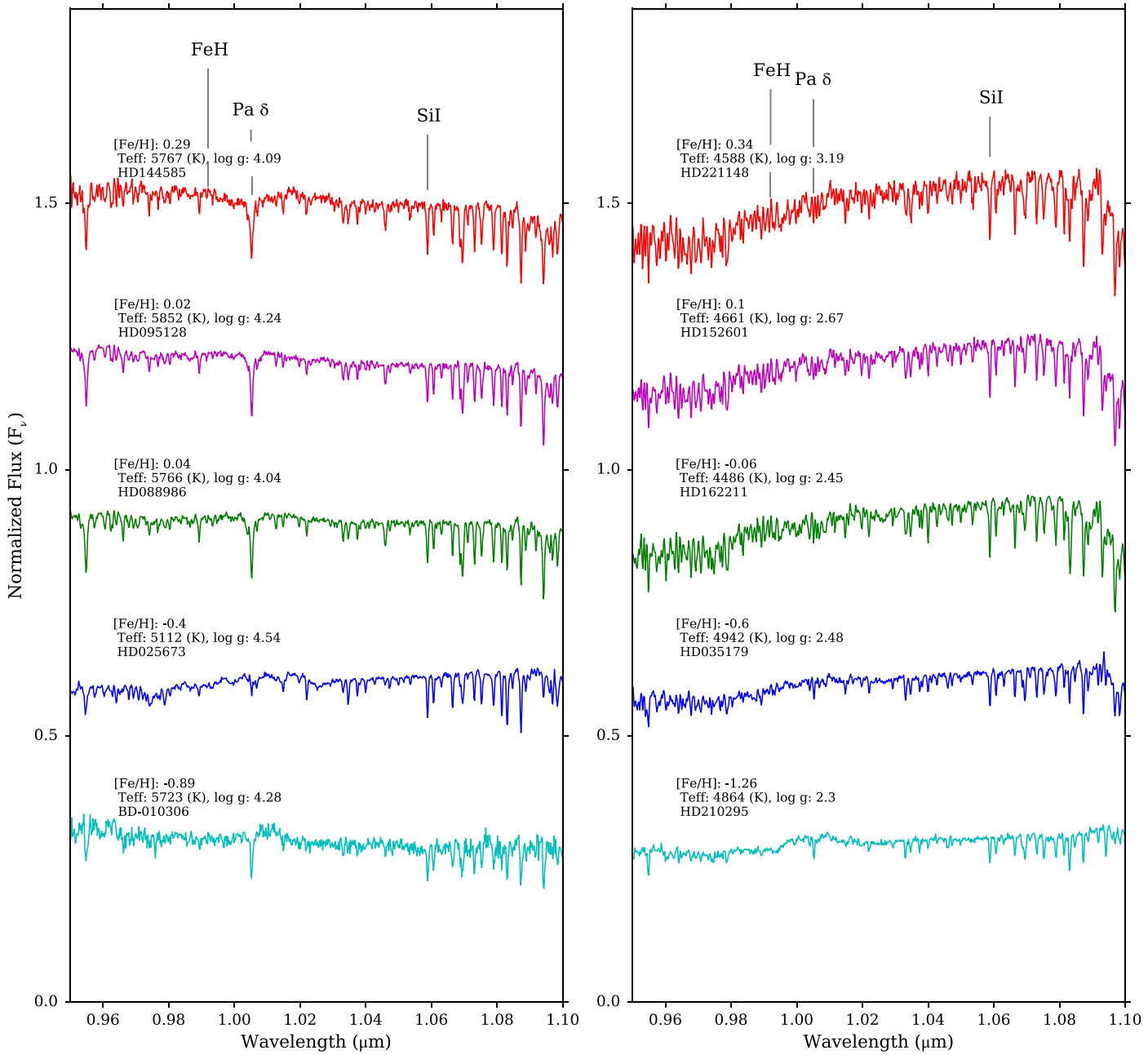

Figure 6. Same as Figure 5, except over the *Y* band (0.95–1.10 μm).

color-coded by *J*-band magnitudes because at $J \sim 9$ and $J \sim 4.5$ the 2MASS observing strategy changed to avoid nonlinearity and saturation for bright stars. This will affect the photometry and corresponding error bars.

For each color we find mean residuals of 0.022, −0.015, −0.026, and 0.041, respectively. The residuals for the near-IR colors are consistent with those of Rayner et al. (2009) and the $B_T - V_T$ residuals are consistent with the result from Sánchez-Blázquez et al. (2006). The $V_T - K_S$ residuals are a reflection of the overall uncertainty of the absolute flux calibration and stitching of the MILES and IRTF spectra. Given the large wavelength baseline and the complications associated with stitching together different spectral data sets, it is not surprising that this color shows the largest offsets between synthesized and observed data.

We explore the reliability of the IRTF spectra further in Figure 12, where we compare our new IRTF spectra to the spectra in the Rayner et al. (2009) IRTF library for four stars in common between the two libraries. In this figure we also compare to $BVJHK_S$ photometry and the MILES spectra. The bottom panel for each star shows the ratio between the old and new IRTF spectra. The agreement in the shape is excellent for HD 076151 and HD 036003, except at the blue end for the former, where we see a small unphysical bump in the flux at $\sim$0.8 μm. This is caused by the difficulty of modeling the Paschen break in the A0 V standard and occurs in a small subset (4%) of our sample. We found that the stars showing this bump were flux calibrated with standard stars that show nebulosity (labeled A0 Vn in Simbad). This was not an issue in the Rayner et al. (2009) library since the detectors did not

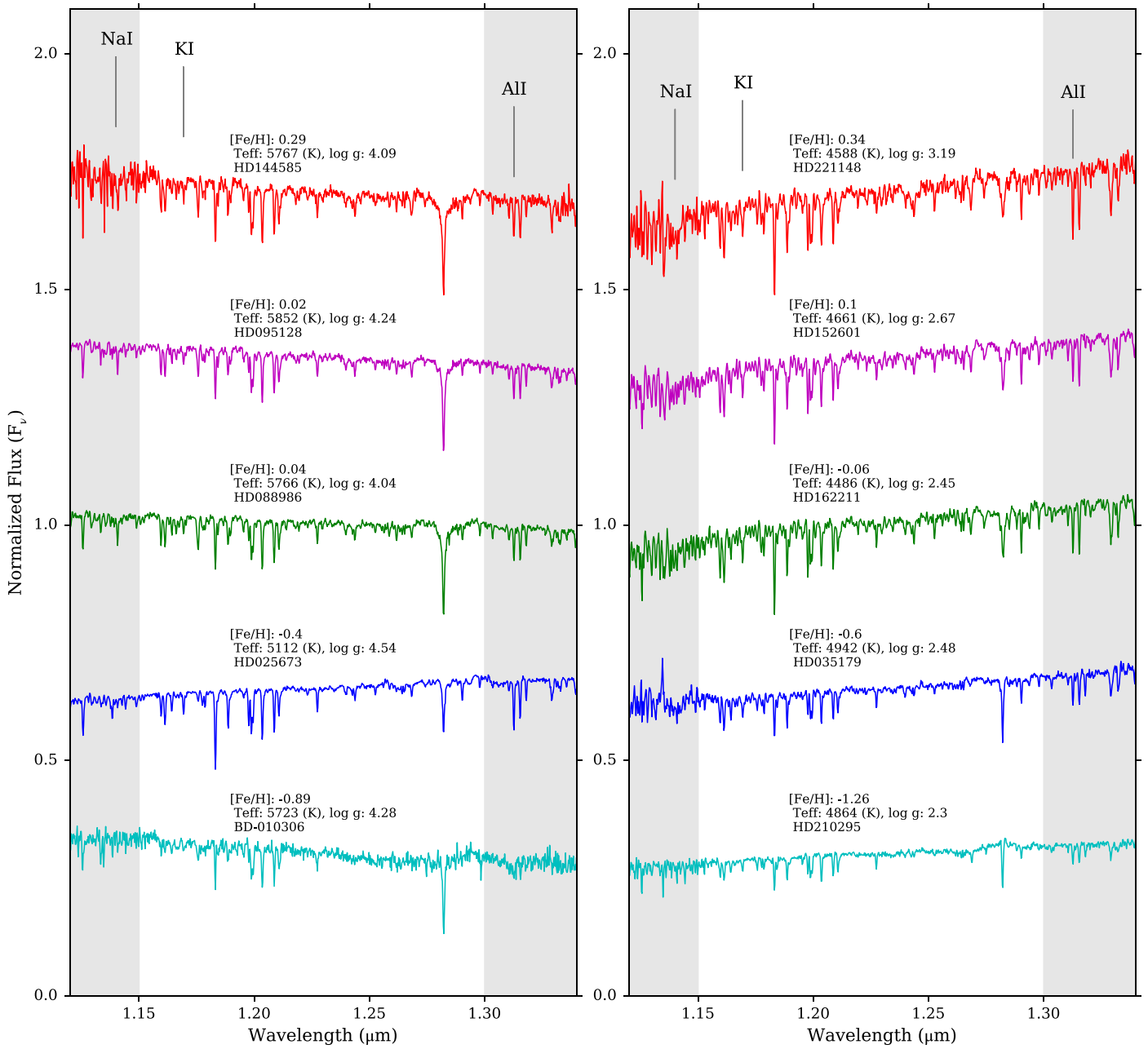

Figure 7. Same as Figure 5, except over the *J* band (1.12–1.34 μm). The vertical gray bands mark regions of poor transmissivity as a result of telluric absorption.

extend to wavelengths as blue as ours. This issue is addressed further in Section 3.

We explore the reliability of the flux calibration of the blue end of the SpeX spectra by comparing the Extended IRTF library stars with the Next Generation Spectral Library (NGSL Gregg 2001), which spans 1680–10000 Å. The NGSL spectra were observed on the STIS instrument on the *Hubble Space Telescope* (*HST*), therefore we can use these spectra as flux standards. There are 35 Extended IRTF Library stars that are also in NGSL. To measure how consistent the flux calibration of the Extended IRTF Library is with NGSL, we synthesized SDSS *i* and *z* photometry (the two passbands that span the blue end of the Extended IRTF Library spectra) for both the NGSL and Extended IRTF Library spectra for the 35 overlap stars. In Figure 13 we show the residuals between the NGSL *i*–*z* colors and the IRTF *i*–*z* colors. The mean residual is smaller than 1%, with a scatter on the order of a few percent, indicating consistency between the flux calibration of the NGSL spectra and the IRTF spectra.

The shape of the spectra is important for computing bolometric luminosities and in creating stellar population models. Consistency at the level of absorption lines between the old and new IRTF spectra is also important as that will change equivalent widths and affect the accuracy of fitting stellar features using these spectra. From Figure 12 we can see that the differences between the Rayner et al. (2009) stellar features and the stellar features in the spectra from this work are 1%–2%, much smaller than the overall shape and flux level differences.

In Figure 14 we show a small sample of stars in the library. They are ordered from cool (upper left corner) to hot (lower right corner). The reduced, redshift corrected, and absolutely

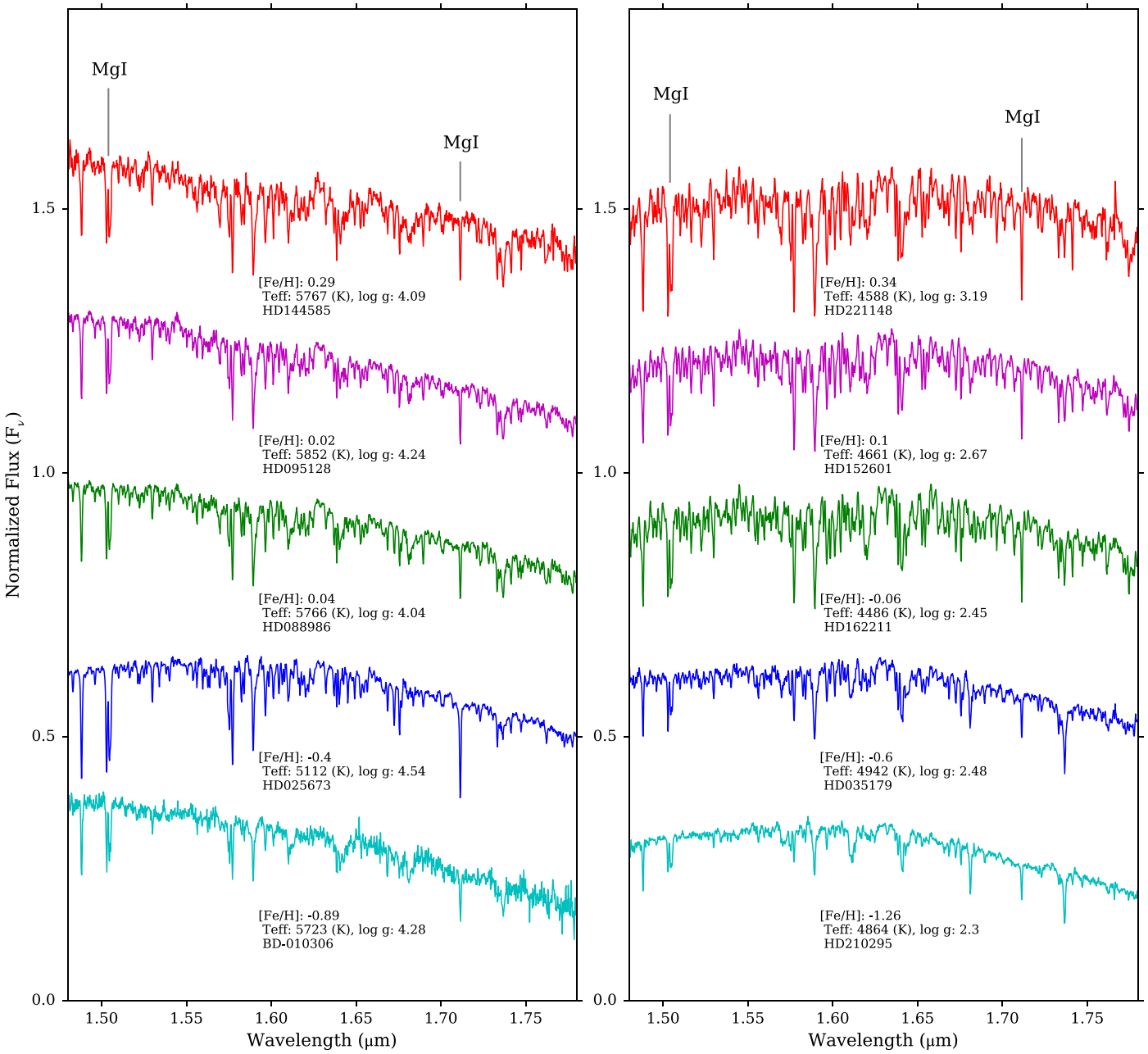

Figure 8. Same as Figure 5, except over the *H* band (1.48–1.78 μm).

flux-calibrated spectra for all the stars observed as part of the Extended IRTF library are available at the IRTF website http://irtfweb.ifa.hawaii.edu/~spex/IRTF_Spectral_Library/.

2.5. Combining the Extended IRTF Library with MILES

The wavelength solution for the SpeX data is not linear and so there is no constant $\Delta\lambda$ between pixels. In practice this means that the spectra for the different stars in the library are on different wavelength grids. The first step to combining the SpeX spectra with the MILES spectra is to place all the Extended IRTF Library stars on the same wavelength grid. We did this by finding the wavelength range that is shared by all the stars in the library, $\lambda_{\rm min} = 0.713$ μm and $\lambda_{\rm max} = 2.559$ μm with 7408 wavelength points (with spacing between the pixels as $\Delta\lambda = 2.495$ Å), and interpolated every spectrum onto that grid.

With the Extended IRTF Library spectra all on a uniform wavelength grid, we combine them with the MILES spectra (where we have converted the MILES wavelengths from being in air to being in vacuum) as follows: for each star, we took the weighted average between the MILES and the Extended IRTF spectra between 0.713 and 0.743 μm using a linear ramp function. The Extended IRTF Library spectra between 0.713 and 0.743 μm were placed on the MILES wavelength grid. At 0.728 μm, the blend is half MILES and half IRTF. The final combined spectrum is a concatenation of the MILES spectrum at $\lambda \leqslant 0.713$ μm, the blended section, and the IRTF spectrum at $\lambda \geqslant 0.743$ μm.

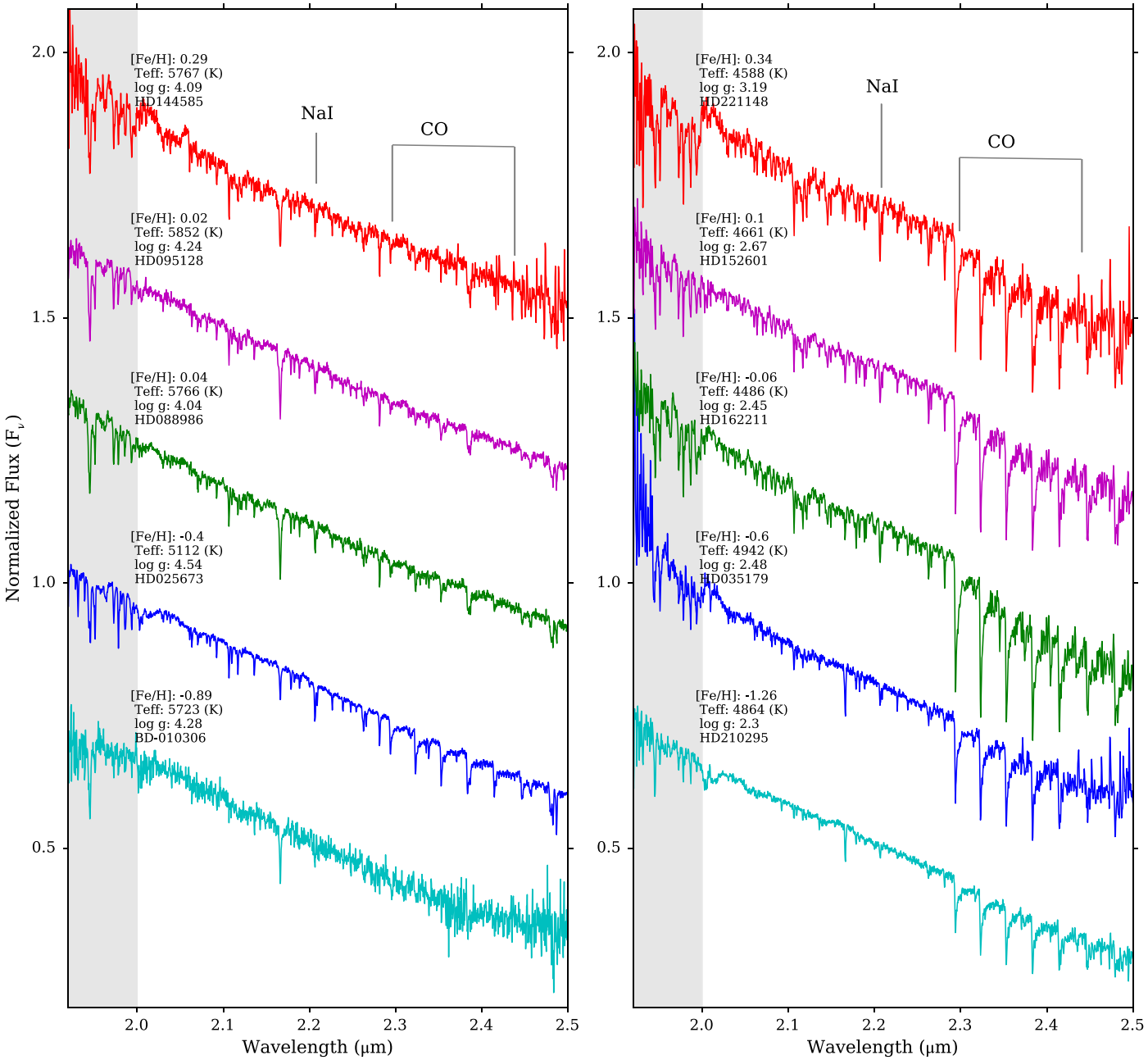

Figure 9. Same as Figure 5, except over the *K* band (1.92–2.50 μm). The vertical gray band marks a region of poor transmissivity as a result of telluric absorption.

2.6. Bolometric Luminosity

To compute the bolometric luminosity for each star, we extended the combined MILES and IRTF spectrum to 0.03 μm and 20 μm using the C3K stellar grid, and integrated the extended spectrum to obtain the bolometric flux. For most of the stars we used parallax-based distances to convert from bolometric flux into bolometric luminosity. For the cluster stars we used cluster distances as a proxy for distance to the star (for NGC 6791, Grundahl et al. 2008; Harris 1996, 2010 edition, for the rest).

Fourteen stars or 5% have neither parallaxes nor known distances, and so the bolometric luminosity cannot be computed for them.

2.7. Resolution

The nominal resolution of the SpeX instrument is $R \sim 2000$. In this section we characterize the wavelength-dependent SpeX resolution, which is essential for using these spectra to model observational data. We also re-measure the MILES spectral resolution for comparison.

The spectral resolution of the MILES/IRTF data was measured by fitting theoretical stellar spectra to these data with the Prospector code. Briefly, for each wavelength regime of each star we calculate a posterior probability distribution for the line spread function (LSF) width and residual velocity, marginalized over the stellar parameters. The log-likelihood for the data given these parameters is calculated by simple χ^2

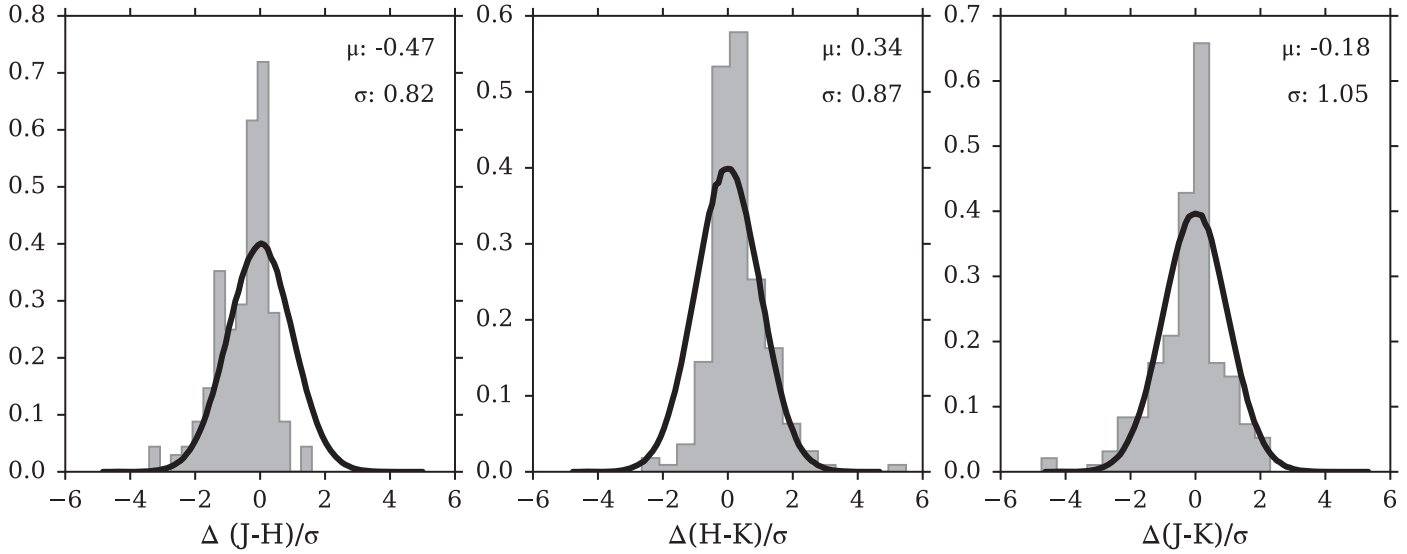

Figure 10. Normalized histogram of the residuals between the observed and synthesized 2MASS $J - H$, $H - K_S$, and $J - K_S$ colors for a subset of the library stars without quality issues, shape issues, or stellar parameter issues (see later discussion and Table 2) divided by the uncertainty. We have indicated the mean offset, μ, and standard deviation, σ. A Gaussian distribution with $\sigma = 1$ is also shown.

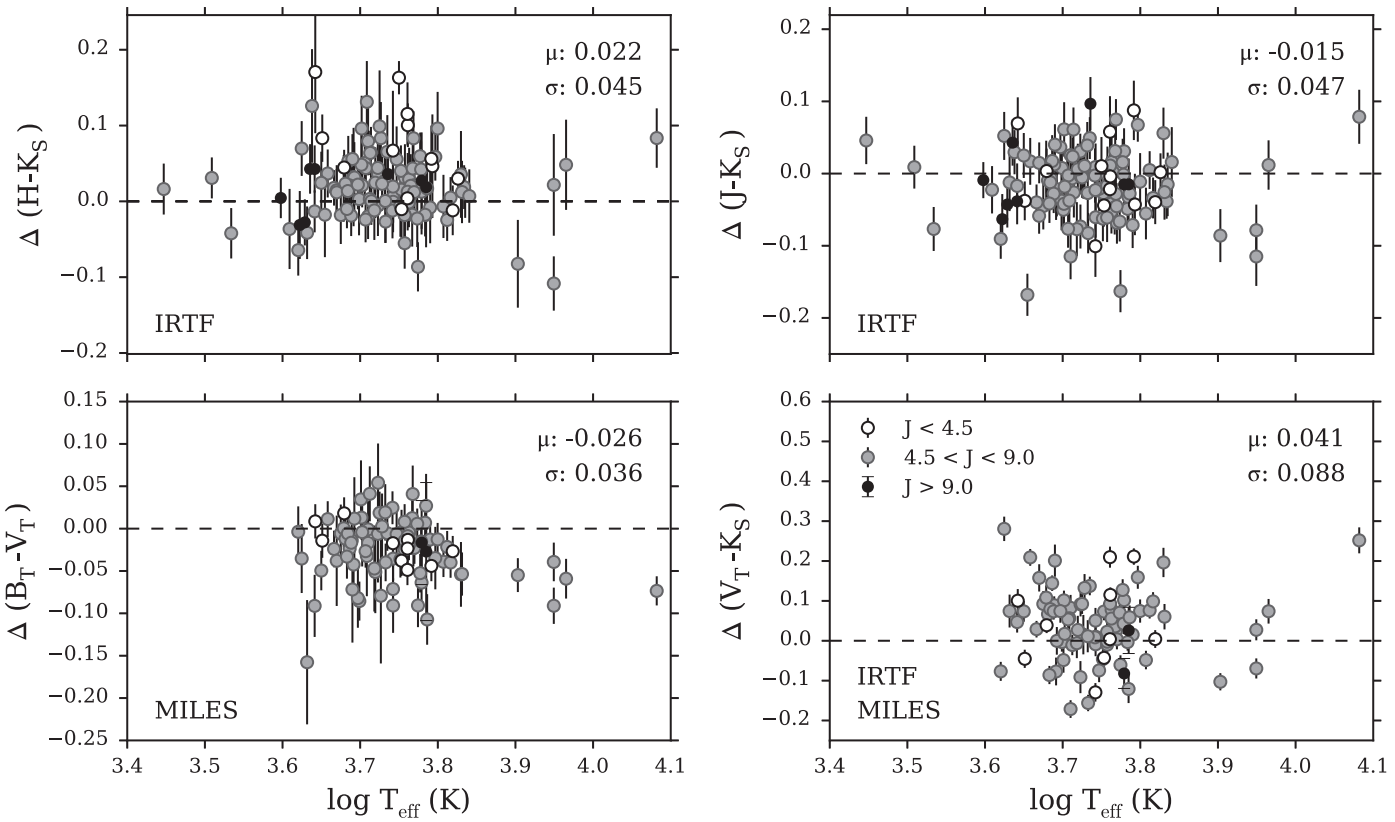

Figure 11. Computed residuals between the observed and synthesized 2MASS $H - K_S$, $J - K_S$, optical $B_T - V_T$, and $V_T - K_S$ colors of 124 library stars with relatively good (uncertainty $\leqslant$3%) 2MASS photometry. The plotted error bars show the 2MASS and Tycho errors in magnitudes. The $V_T - K_S$ colors are a test of how well the MILES and IRTF stars were stitched together.

between the data and the smoothed theoretical model. This model is constructed by tri-linear interpolation of a high-resolution version of the C3K theoretical stellar library in the stellar parameters log $T_{\rm eff}$, log$g$, and [Fe/H], which is then smoothed to a fixed resolution in $\Delta\lambda$(FWHM Å) using fast Fourier transforms, and interpolated to the wavelength scale of the data after shifting in velocity. This smoothing assumes a Gaussian LSF with rms width $\Delta\lambda/2.355$. To minimize template mismatch, the stellar parameters log$g$, log $T_{\rm eff}$, and [Fe/H] are allowed to vary from the Prugniel et al. (2011) parameters within some tolerance. The velocity and instrumental resolution $\Delta\lambda$ (Å) have uniform priors within some

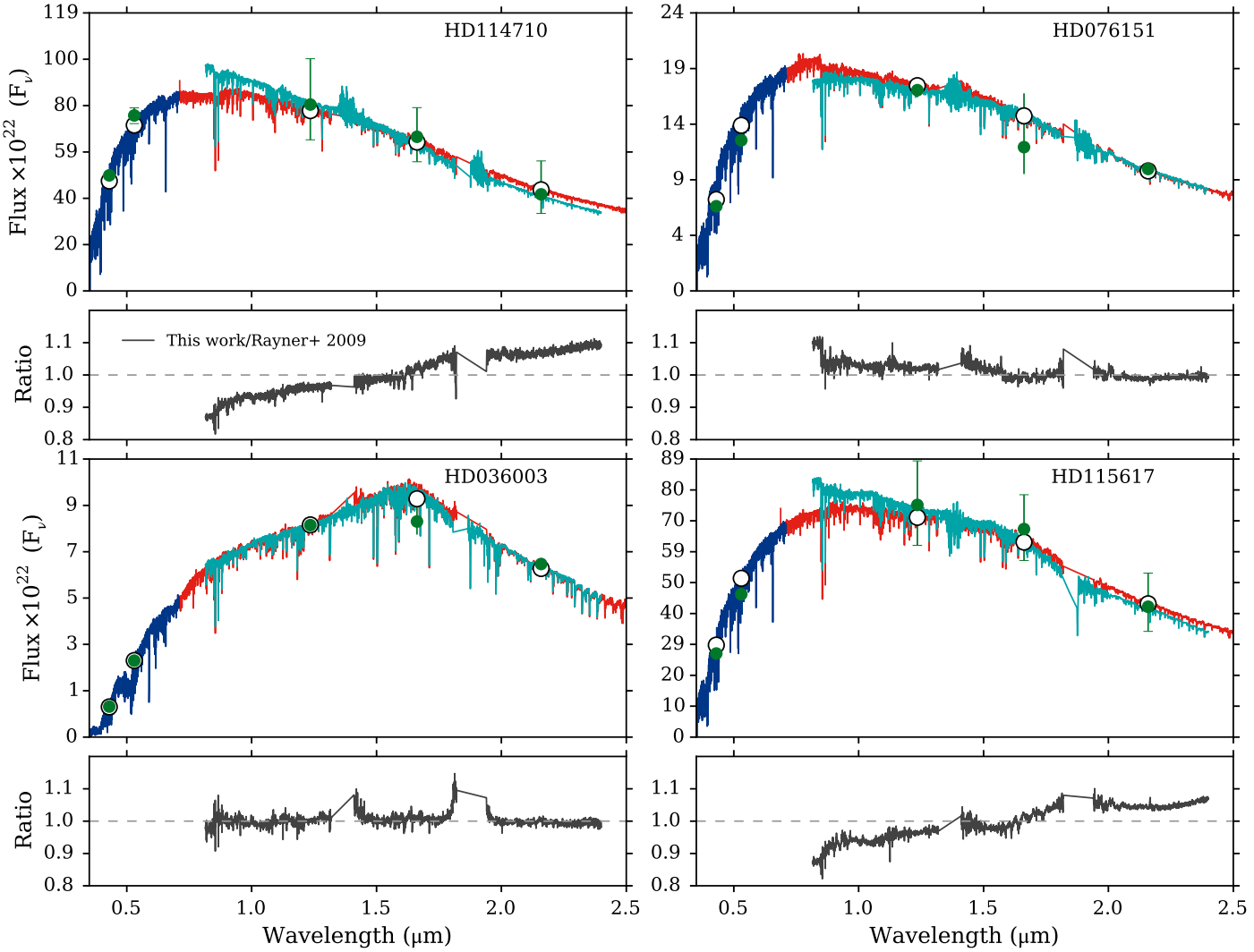

Figure 12. Comparison of new spectra presented in this work (red), spectra from the Rayner et al. (2009) library (turquoise), and the MILES spectra (blue) for four stars. Also plotted is the observed photometry (green circles) and synthetic photometry (open circles) derived from the spectra. The shapes of the spectra presented in this work match the shape of the MILES spectra in the overlap region well and also the observed JHK_S photometry. Below each spectral comparison we plot the ratio of the IRTF spectra presented in this work and the spectra from Rayner et al. (2009).

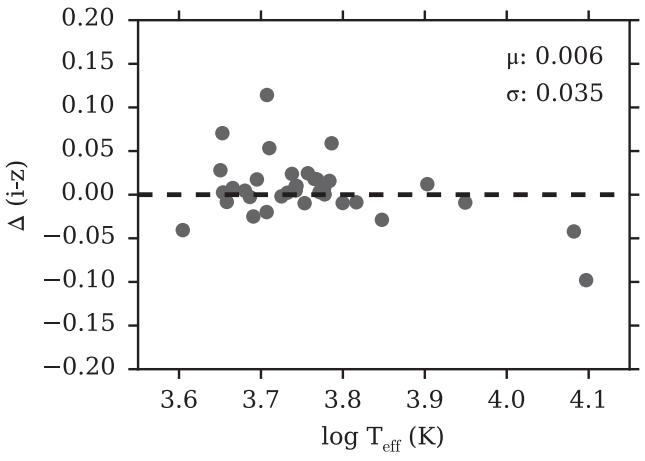

Figure 13. Computed residuals between the NGSL and IRTF synthetic SDSS $i - z$ colors for 35 stars that are in both libraries.

reasonable range for each segment. The residual velocities are consistent with zero. This posterior probability is then sampled using MCMC techniques, specifically the ensemble sampling algorithm (Goodman & 2010; Foreman-Mackey et al. 2013). The resulting maximum a posteriori values are reported, corrected for the resolution of the theoretical library.

These fits are made separately for several wavelength regions of the spectrum of each star; the optical spectra are split into six regions each 400 Å wide, while six regions in the IRTF spectra are defined around prominent spectral features and avoiding regions of low atmospheric transmission.

In Figure 15 we show the median resolution (solid line) for 135 warm ($3980\,K < T_{\rm eff} < 6300$ K) stars and the scatter (shaded region) over 12 wavelength segments spanning the full Extended IRTF spectra. In the top panel we show the wavelength segments for the part of wavelength space covered by the MILES spectra, and in the bottom panel we show the wavelength segments for the wavelength space covered by the IRTF spectra. In the top panel we show a constant line at $\Delta\lambda = 2.54$ (Å), the revised resolution found by Beifiori et al. (2011). The median resolution we find over the different wavelength regions of the MILES spectra is $\Delta\lambda = 2.54$ (Å) $\pm$ 0.19 ($R \sim 1970$ at 0.5 μm), consistent with the Beifiori et al. (2011) value. In the bottom panel we show a constant line for $R \equiv \lambda/\Delta\lambda = 2000$. The median resolution we find over

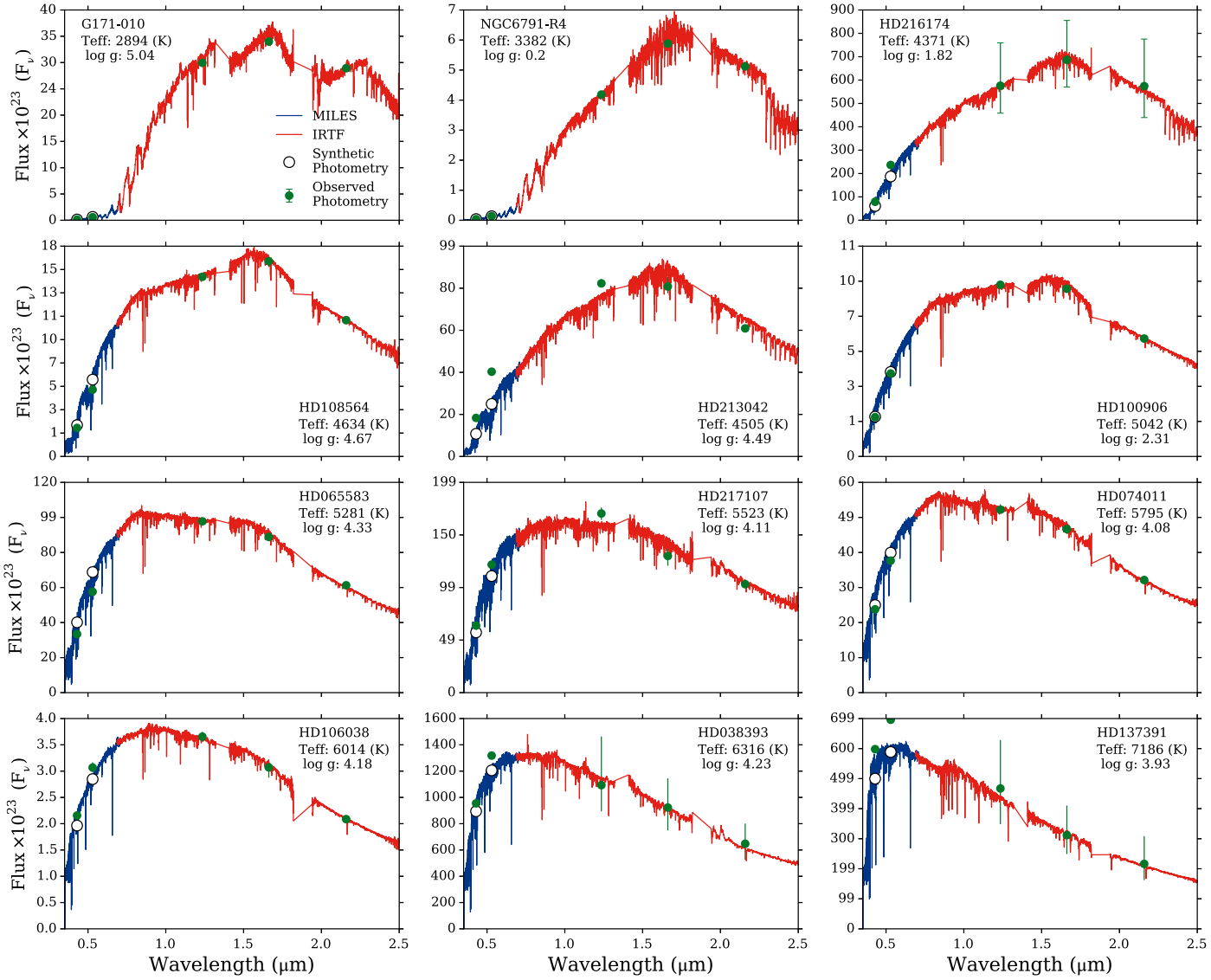

Figure 14. IRTF spectra (red) for a small subset of the library stars plotted with the MILES spectra (blue), observed photometry (green circles), and synthetic photometry (open circles).

the different wavelength regions for the IRTF spectra is $R = 2020 \pm 230$, consistent with the quoted value for the SpeX instrument.

3. Spectral Polynomial Interpolator

Interpolators have long been used in conjunction with stellar libraries. What began as "fitting functions" for specific indices (e.g., Gorgas et al. 1993; Worthey et al. 1994) has now evolved to full spectral interpolators (e.g., Vazdekis et al. 2003; Prugniel et al. 2011; Ness et al. 2015; Sharma et al. 2016; Dries et al. 2016). Broadly speaking, interpolators are either "global," where a polynomial is fit to the input sample points, or "local," which essentially averages the nearby data, e.g., the linear or spline interpolation is a weighted average of only the data closest in parameter space. Global interpolation is appropriate when the surface is smooth and can be approximated by a (relatively) simple function. The interpolators of Vazdekis et al. (2003) and Dries et al. (2016) are local interpolators, while the interpolators described in Prugniel et al. (2011), Ness et al. (2015), and Sharma et al. (2016) are global.

In this same spirit, as a companion to the Extended IRTF library, we created the Spectral Polynomial Interpolator (SPI[8]). With SPI we create a data-driven, global interpolator that we can use to retrieve a spectrum for a set of arbitrary stellar parameters. In this section we describe the input to SPI, how we construct the model, the quality of interpolation, and example uses for SPI.

3.1. The Training Set

SPI works by fitting polynomial functions of $T_{\rm eff}$, $\log g$, and [Fe/H] to the $L_{\rm bol}$-normalized flux of all the stars included in the training set. These fits are carried out independently of the fluxes at each wavelength. Then, for any set of stellar parameters, these polynomial functions can be used to predict or approximate the flux at a given wavelength.

The primary input into SPI is the IRTF Extended Library, limiting the sample to stars with computed bolometric luminosities (see Section 2.4.1), high-quality spectra, and

[8] http://github.com/bd-j/spi

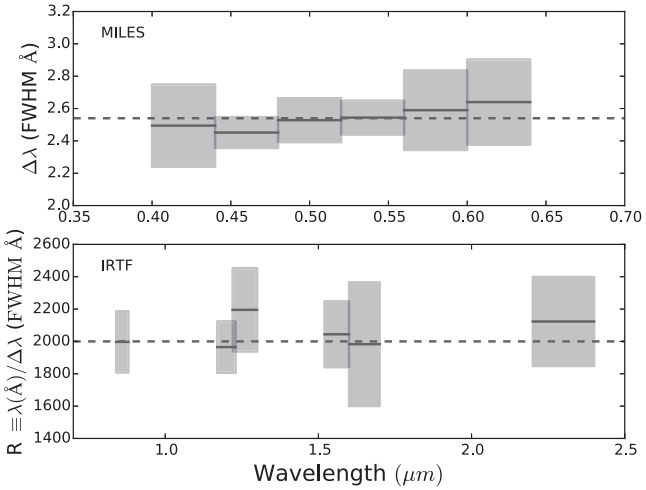

Figure 15. Median resolution (solid line) for 135 stars and the scatter (shaded region) over 12 wavelength segments. The top panel is the wavelength range of the MILES spectra with the resolution quoted as $\Delta\lambda$ (FWHM Å), the commonly quoted unit for MILES spectral resolution. We plot a constant line at $\Delta\lambda = 2.54$ Å, the revised resolution found in Beifiori et al. (2011). The bottom panel is the wavelength range of the IRTF spectra, and the resolution is quoted in $R \equiv \lambda/\Delta\lambda$. We plot a constant line at $R = 2000$, the quoted resolution for SpeX. For the MILES spectra we measure a median $\Delta\lambda = 2.54$ Å $\pm$ 0.19, and for the IRTF spectra we measure a median $R = 2020 \pm 230$.

accurate stellar parameters (more on the latter two later; see also Table 2). The library stars that made the final cut to be included in the training set are shown as red points in Figure 16. We have augmented the SPI training set in several ways, which we describe below. In total, 194 Extended IRTF Library stars were included in the final SPI training set.

We include the wavelength-dependent uncertainties for every star in the training set and weight the fluxes in the training sample by the corresponding uncertainty.

3.1.1. Additions to the Cool Dwarf Regime

We can see from Figure 1 that there is a paucity of cool dwarf stars in the MILES library and subsequently the library presented in this work. Having few cool dwarf stars would have hindered our ability to build an accurate polynomial model in this regime. We therefore included 76 M dwarf stars presented in Mann et al. (2015) in the SPI training set (purple points in Figure 16), excluding stars with low S/N. We also found that 4 stars had strong chromospheric Balmer emission lines, which we removed from the training set.

The spectra from Mann et al. (2015) are a combination of SNIFS (0.3–0.95 μm) and pre-detector upgrade SpeX (0.8–2.4 μm). The resolution of the SNIFS data is coarser ($R \sim 1000$) than the resolution of the MILES data. To place the SNIFS data on the same spectral resolution scale as the MILES data, we used a high-resolution ($R \sim 10{,}000$) version of C3K to deconvolve the SNIFS portion of the Mann et al. (2015) data to the resolution of the MILES data. We did this by producing a spectrum using the stellar parameters of a given star in the Mann et al. (2015) sample and made two models, one each for the MILES and SNIFS resolutions. We took the ratio of these two models, interpolated it onto the MILES wavelength grid, and multiplied the Mann et al. (2015) spectrum by this correction factor. Visual comparison of a SNIFS and MILES star of the same stellar parameters led us to conclude that this procedure was effective.

We use the stellar parameters as presented in Mann et al. (2015) with the surface gravity given by

$$\log g = \log_{10}\left(\frac{6.6743 \times 10^{-8} \times M \times 1.989 \times 10^{33}}{(R \times 6.955 \times 10^{10})^2}\right), \quad (5)$$

where M and R represent the stellar mass and radius in solar units.

We note that while we use the surface gravity to make the parameterization of the M-dwarf stars consistent with the other regimes, surface gravity is not a commonly used metric in M-dwarf research. M dwarfs do not age on a Hubble time, and so the surface gravity can be uniquely determined by effective temperature and metallicity.

3.1.2. Support for Extrapolation

To preserve the quality of the interpolator at the edges of the empirical parameter space, we supplement the training set with spectra from the theoretical C3K library (gray points in Figure 16) degraded to the SpeX resolution. We only added C3K spectra for stellar parameters outside the convex hull (a hull being the set of planes that encloses all the training points) of the MILES stars. The C3K spectra are normalized in the same way as the observed spectra.

Our goal is for the C3K library to keep the polynomial terms "well-behaved" at the boundaries of parameter space for the empirical spectra, but we do not wish for the fits to be driven by the large numbers of C3K stars. We therefore weight the C3K spectra in the fits by a factor of 10^{-2} times the median S/N of the empirical spectra. This factor was chosen after considering a range of values and inspecting the resulting polynomial behavior.

3.2. Training the Model

The library contains a wide range of spectral types, with stellar temperature being the primary driver of the shape of the spectra. Modeling all the stars together is not feasible since it is difficult to specify a polynomial model that can encompass such a diverse set of stars. We therefore partition the library into five subsets based on temperature and surface gravity, essentially making five global interpolators that we use in conjunction with each other to span the entirety of parameter space. For each subset we define the polynomial terms we use to create the model ($t \equiv \log T_{\rm eff}$, $z \equiv$ [Fe/H], $g \equiv \log g$):

1. Cool Dwarfs

$$\begin{aligned}\log F_\nu = {} & a_0 + a_1 t + a_2 z + a_3 g + a_4 z^2 + a_5 t^2 + a_6 g^2 \\ & + a_7(t \times z) + a_8(t \times g) + a_9(z \times g) + a_{10} z^3 \\ & + a_{11} t^3 + a_{12} g^3 + a_{13}(t^2 \times z) + a_{14}(z^2 t) \\ & + a_{15}(g \times t^2) + a_{16} t^4 + a_{17} z^4 + a_{18}(t^2 \times z^2) \\ & + a_{19}(t^3 \times z) + a_{20} t^5. \end{aligned} \quad (6)$$

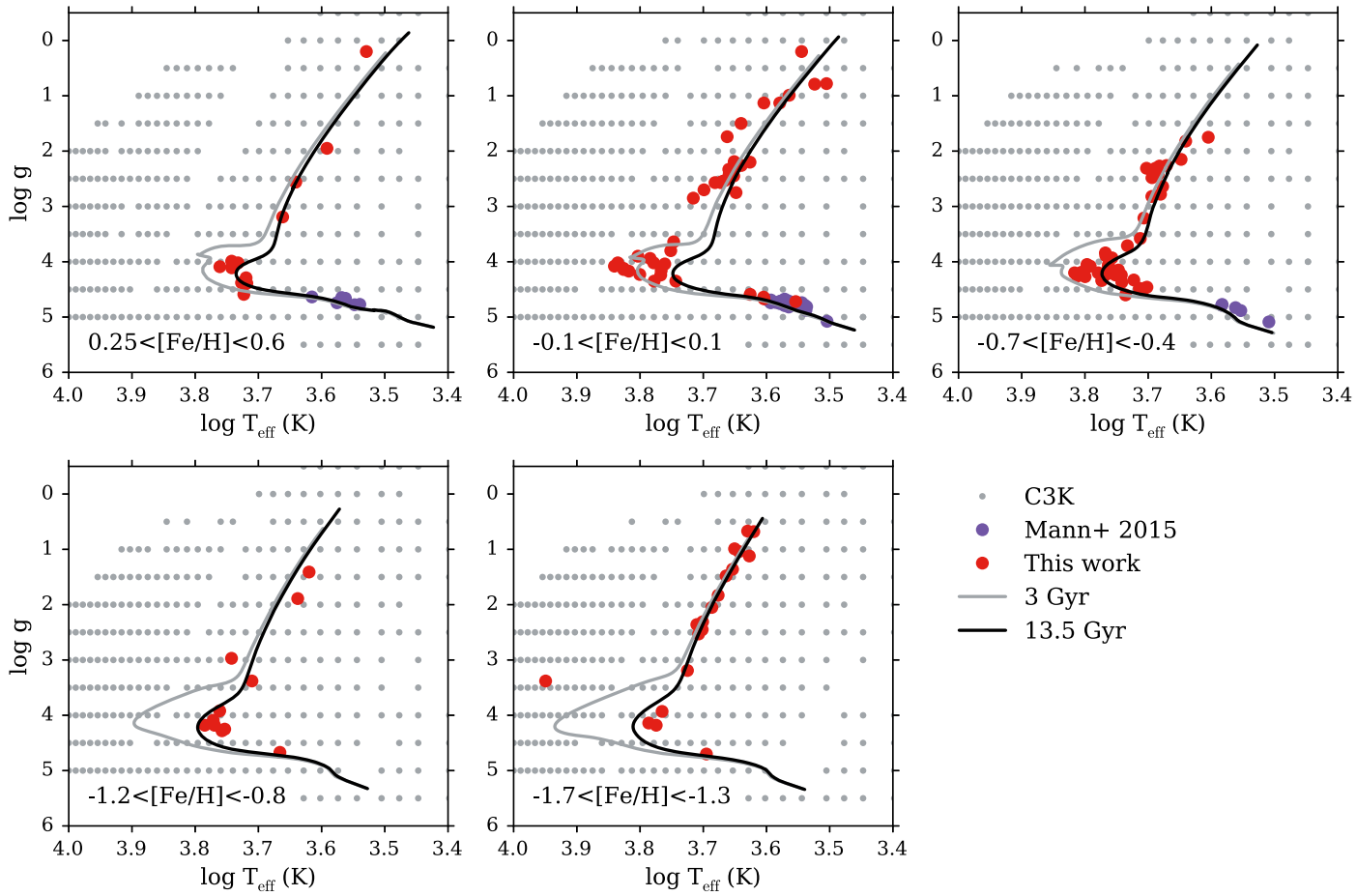

Figure 16. Location of all the stars included in the SPI training set in $T_{\rm eff}$ vs. log$g$ space including the stars from the Extended IRTF library (red circles), the M dwarfs from Mann et al. (2015) (purple circles), and the C3K theoretical spectra (gray dots). We only use the C3K theoretical spectra outside the convex hull determined by the empirical spectra. Isochrones are the same as in Figure 1.

2. Cool Giants

$$\begin{aligned}\log F_\nu = {} & a_0 + a_1 t + a_2 z + a_3 g + a_4 t^2 \\ & + a_5 g^2 + a_6 z^2 + a_7 (z \times g) + a_8 (t \times g) \\ & + a_8 (t \times z) + a_9 t^3 + a_{10} g^3 + a_{11} z^3 \\ & + a_{12} (t \times g \times z) + a_{13} (t \times t \times z) \\ & + a_{14} (t \times t \times g) + a_{15} (z^2 \times t) + a_{16} (z^2 \times g) \\ & + a_{17} (t \times g^2) + a_{18} (z \times g^2) + a_{18} t^4. \end{aligned} \quad (7)$$

3. Warm Dwarfs

$$\begin{aligned}\log F_\nu = {} & a_0 + a_1 t + a_2 z + a_3 g + a_4 t^2 + a_5 g^2 + a_6 z^2 \\ & + a_7 (t \times z) + a_8 (t \times g) + a_9 t^3 + a_{10} (t \times g^2) \\ & + a_{11} z^3 + a_{12} (t^2 \times g) + a_{13} (t^2 \times z) + a_{13} (t \times z^2) \\ & + a_{14} (t \times g \times z) + a_{15} (g \times z^2) + a_{16} t^4 + a_{17} g^4 \\ & + a_{18} (t^3 \times g) + a_{20} (z \times t^3) + a_{21} (z^2 \times t^2) \\ & + a_{21} (z^3 \times t) + a_{22} (t^2 \times g)^2) + a_{23} (z \times t^2 \times g) \\ & + a_{24} t^5. \end{aligned} \quad (8)$$

4. Warm Giants

$$\begin{aligned}\log F_\nu = {} & a_0 + a_1 t + a_2 z + a_3 g + a_4 t^2 + a_5 g^2 + a_6 z^2 \\ & + a_7 (t \times z) + a_8 (t \times g) + a_9 (g \times z) + a_9 t^3 \\ & + a_{10} g^3 + a_{11} z^3 + a_{12} (t^2 \times z) + a_{13} (t \times z^2) \\ & + a_{14} (g \times t^2) + a_{15} (g^2 \times t) + a_{16} t^4 + a_{17} z^4 \\ & + a_{18} (t^2 \times z^2) + a_{19} (t^2 \times g^2) + a_{20} (z^2 \times g^2) \\ & + a_{21} t^5. \end{aligned} \quad (9)$$

5. Hot Stars

$$\begin{aligned}\log F_\nu = {} & a_0 + a_1 t + a_2 z + a_3 g + a_4 t^2 + a_5 z^2 + a_6 g^2 \\ & + a_7 (t \times g) + a_8 (t \times z) + a_9 (g \times z) + a_{10} t^3 \\ & + a_{11} g^3 + a_{12} z^3 + a_{13} (t \times g \times z) + a_{14} (t^2 \times z) \\ & + a_{15} (t^2 \times g) + a_{16} (z^2 \times g) + a_{17} (t \times g^2) \\ & + a_{18} (z \times g^2) + a_{19} t^4. \end{aligned} \quad (10)$$

The maximum likelihood coefficients for each regime are determined by weighted linear least squares. The glut of

Table 1
Valid Ranges for SPI Interpolation

Regime	Training			Interpolating		
	$T_{\rm eff}$	log$g$	[Fe/H]	$T_{\rm eff}$	log$g$	[Fe/H]
Cool Dwarfs	1100–5500	3.5–6.5	−2.5–0.6	2500–4000	−0.5–3.5	–2.0–0.6
Cool Giants	1100–4500	–1.0–2.75	–2.5–0.6	2500–4000	>3.5	–2.0–0.6
Warm Dwarfs	3000–6500	3.0–5.75	–2.5–0.6	4000–6000	–0.5–3.5	–2.0–0.6
Warm Giants	3500–6500	–0.75–4.0	–2.5–0.6	4000–6000	>3.5	–2.0–0.6
Hot Stars	5500–12,500	2.5–5.5	–2.5–0.6	6000–12,000	<5.0	–2.0–0.6

polynomial terms is a classic problem in polynomial regression modeling. As we are concerned with the ability to predict spectra (which we assess later in Section 3.3) rather than the values of the coefficients themselves, we do not make an effort to simplify the polynomial functions using, e.g., L1 regularization. Furthermore, the oscillatory behavior of extrapolations that can result from unregularized high-order polynomial regression is mitigated by our use of theoretical spectra near the boundaries of the valid parameter space.

In Table 1 we show the "training" ranges for $T_{\rm eff}$, log$g$, and [Fe/H], i.e., the stellar parameter limits for the training set stars in each regime and the "interpolating" ranges for $T_{\rm eff}$, log$g$, and [Fe/H], i.e., the stellar parameter limits for safe interpolation. We have the same range in metallicity for the training bounds of all the stellar regimes. The ranges were determined by minimizing the rms difference between the observed and interpolated spectra in the training set. The overlap in the $T_{\rm eff}$ training ranges is meant to mitigate the effect of five separate, disjoint hulls having a smaller volume than the hull for all the library points. For most regimes the overlap in $T_{\rm eff}$ is 500 K, but for the cool dwarf regime we extend the training sample to 5500 K. We do this to compensate for the paucity of low-metallicity cool dwarfs in the empirical library. If we had not extended the training sample to 5500 K, the metallicity dependence for the cool dwarf regime would end at [Fe/H] ~ -0.7, which would bias the interpolation to lower metallicities. With the extended temperature range of the training sample, SPI is able to pull information from the warmer low-metallicity stars, which mitigates the effects of the lack of observed low-metallicity cool dwarfs.

3.2.1. Culling the Extended IRTF Library

Only the highest quality spectra should be included in the SPI training set. Any star used in the training set needs to have accurate stellar parameters and a reliably flux-calibrated observed spectrum. Based on visual inspection, we removed stars with spectra that were either of poor quality or appeared to have flux calibration issues that severely affected the shapes. We removed 51 stars following these criteria (see the Quality Flag and Shape Flag columns in Table 2).

Furthermore, since the interpolation relies on having like-spectra grouped by like-stellar parameters, we need to ensure that our stellar parameters are accurate. SPI provides an opportunity to check the accuracy of the stellar parameters associated with each of the stars in the library. If there is significant discrepancy between the observed spectrum of the star and the interpolated spectrum given by SPI, it might be indicative of an issue with the stellar parameters associated with that star. A similar technique was used by Vazdekis et al. (2010) to remove 60 stars from the MILES library in creating stellar population models.

In Figure 17 we show an example of three stars where the SPI predicted spectra (purple) using the stellar parameters from Prugniel et al. (2011) and Sharma et al. (2016) are not consistent with the observed data (both spectroscopy, shown by the red line, and photometry, plotted as green circles). The consistency between the observed photometry and observed spectra for these stars suggests that the problem is not exclusively associated with the flux calibration, but with the stellar parameters. To further emphasize this point, we also show two C3K spectra corresponding to different effective temperatures in each panel. For the dark gray spectra we used the effective temperatures computed using the González Hernández & Bonifacio (2009) $J - K_S$-metallicity relations. For the light gray spectra we used the effective temperatures from Cenarro et al. (2007). For HD 219978 (left) and HD 173819 (middle) the overall shape of the spectra using the $J - K_S$ derived temperatures are more consistent with the observed data than SPI and the spectra corresponding to the Cenarro et al. (2007) spectra. For HD 076813 (right) the spectrum corresponding to the temperature from Cenarro et al. (2007) is most consistent.

This test both demonstrates the possible range in derived stellar parameter values and that there are available stellar parameters that would better match the observed spectra and photometry, and thus the problem lies in the Prugniel et al. (2011) and Sharma et al. (2016) stellar parameters. These stars were flagged for having an exceptionally high rms difference between the observed and SPI predicted spectra. We flagged 9% of our observed sample as having incorrect stellar parameters and do not include them in the SPI training set. The differences in the temperatures determined using different methods for these stars are large compared to the bulk of the library stars. This indicates that in general the stellar parameters from Prugniel et al. (2011) and Sharma et al. (2016) are consistent with the observations.

This test does not mean that any issue with the data is exclusively an issue with the stellar parameters. Several of the stars flagged as potentially having incorrect stellar parameters also have flux calibration issues or other quality issues as indicated by their Quality and Shape Flags (see Table 2). For example, we still see the effects of prominent telluric absorption for HD 173819 (the middle panel) that is indicated in Table 2. However, the SPI predicted spectrum is not consistent with the shape of the observed spectrum, but the predictions based on the Cenarro et al. (2007)

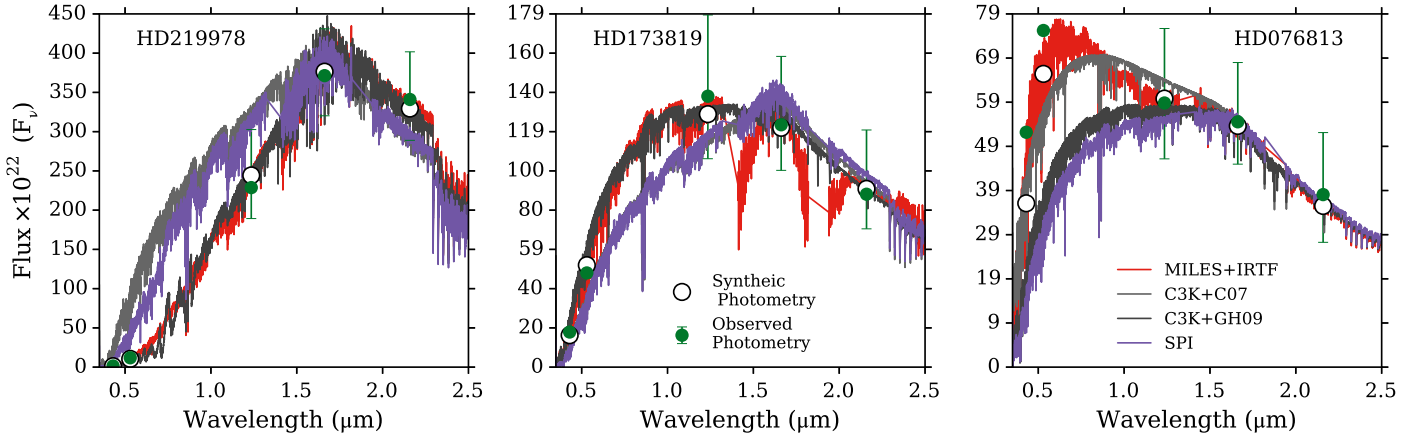

Figure 17. Comparison of data (spectroscopy in red and photometry as green circles) with the SPI model (purple) and theoretical spectra using two choices for effective temperature (gray lines). Synthetic photometry is shown for clarity (open symbols). For the dark gray line the temperature used was derived from the metallicity-color relations of González Hernández & Bonifacio (2009). The temperature used for the light gray line is the value from Cenarro et al. (2007). This shows the spread in $T_{\rm eff}$ values, and thus the spread in expected spectral shape, from different methods for each star. For the stars shown the spectral shape expected from the Prugniel et al. (2011) and Sharma et al. (2016) values is not consistent with the observed spectral shape.

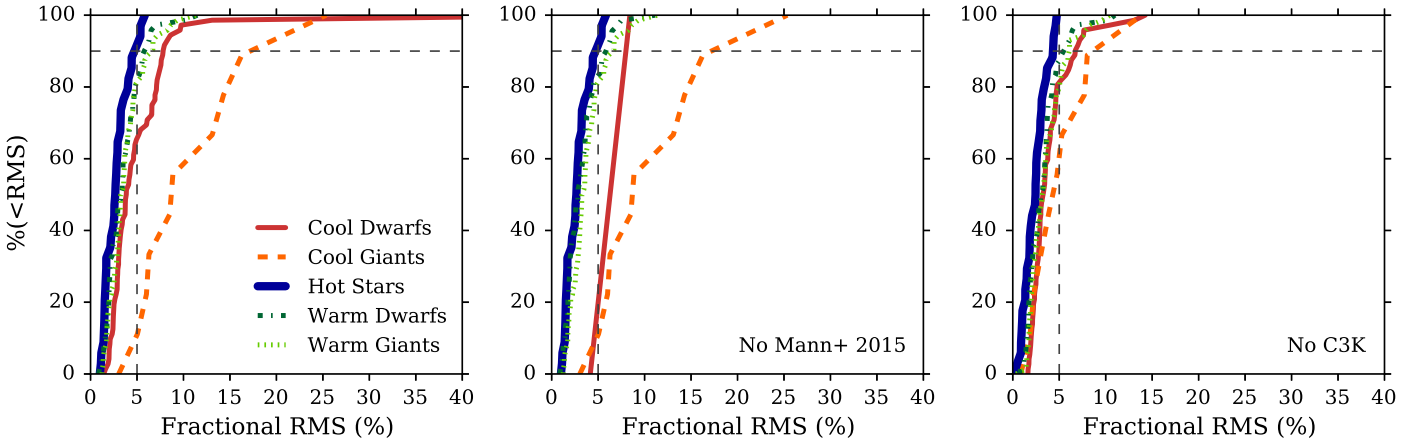

Figure 18. Cumulative distribution functions of the fractional rms differences between the observed spectra and interpolated spectra in the cool dwarf (red), cool giant (orange), hot (blue), warm dwarf (green), and warm giant (lime) regimes. To aid interpretation, a fractional rms difference of 5% is marked with a vertical dashed line and 90% of the sample is marked with a horizontal dashed line.

temperature and temperature from the González Hernández & Bonifacio (2009) relations are consistent with the observed shape.

Thus, we can use SPI as a way to flag stars that need more accurate stellar parameters but otherwise have good data (in the future we will use SPI to rederive stellar parameters in an iterative approach). We removed 27 stars following these criteria and rederived the SPI parameters with these stars removed (see "Parameter Flag" column in Table 2).

3.3. Quality of Interpolation

We can assess the quality of the interpolation by examining how well SPI can recover the spectra of the stars in the training sample (including both the data presented in this work and the Mann et al. (2015) data). For each star we compute the fractional rms between an observed spectrum in the empirical training set and the corresponding interpolated spectra from SPI. In Figure 18 we show the cumulative distribution of this fractional rms. In each panel we show results separately for the cool dwarf stars (red), cool giant stars (orange), hot stars (blue), warm dwarf stars (dark green), and warm giant stars (light green). Also plotted in each panel is a horizontal line showing where 90% of the stars are placed on the cumulative distribution and a vertical line marking 5% fractional rms. In the left panel we show the distributions when using the complete training set in the model, in the middle panel we show the distributions when we exclude the Mann et al. (2015) spectra from the training set, and in the right panel we show the distributions that result when we exclude the C3K spectra from the training set. Note that the rms is insensitive to overall offsets between the two spectra. Note that SPI is not an interpolator in the strictest sense of exactly reproducing the input spectrum at the input points, and so there is no guarantee that the rms should be small.

The most important insight gained from Figure 18 is that for all the regimes the recovery of the training set spectra is very good. For cool dwarfs, warm dwarfs, warm giants, and the hot stars the recovery is better than 10% for 90% of the stars. When

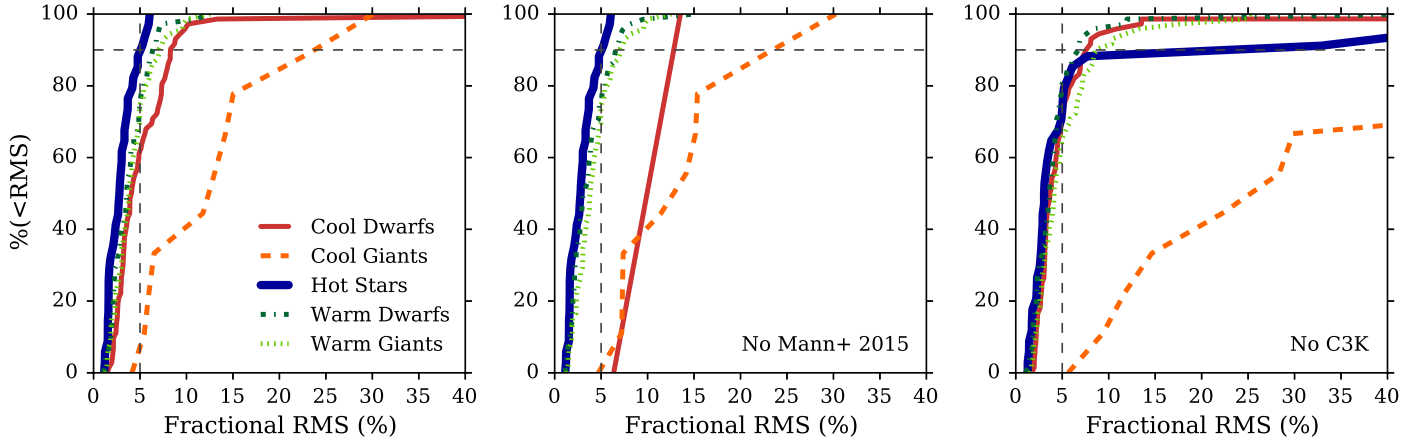

Figure 19. Same as Figure 18, but now the interpolated spectra are the result of the leave-one-out ("jackknife") test where each star in the training sample was removed from the model in turn before the interpolation. Including the C3K spectra reduces the dependence of the model on the presence of any one star, especially the cool giant stars and hot stars. The inclusion of the Mann et al. (2015) M dwarfs also helps mitigate issues in the cool dwarf regime.

we exclude the Mann et al. (2015) M dwarfs from the training set, the recovery for the cool dwarfs is worse. The recovery of the cool giants is worse than the other regimes and counter-intuitively improves when we exclude the C3K spectra from the training set. This could be an effect of the problems theoretical spectra have in the cool giant regime (see Bertone et al. 2008).

Since SPI relies on stars with similar stellar parameters having similar stellar spectra, we can look at stars for which SPI fails to recreate the spectra as stars with possible issues with the stellar parameters. Since we see in Figure 18 that for most of the library (∼90%) the rms difference between the observed and interpolated spectra is <5%, we can feel confident that the stellar parameters from Prugniel et al. (2011) and Sharma et al. (2016) are internally self-consistent. We looked at Figure 18 separately for the MILES and IRTF spectra and found that the recovery is about the same for the majority of the stars.

Figure 19 is the same as Figure 18, but now the interpolated spectra are the result of leave-one-out validation. The leave-one-out test consists of going through all the stars in the training sample, taking one out of the training sample at a time, retraining the function such that the information from that star is no longer included in the model, and then comparing the SPI prediction for that spectrum to the actual spectrum.

The leave-one-out test is an assessment of how sensitive the model is to the presence of any one star and demonstrates the utility of including the C3K spectra in the training set. This figure shows that by including the C3K spectra in the training set, we are mitigating the bias a single star can introduce in the model, especially for the cool giant stars and hot stars, where the number of empirical stars is low. We see that the Mann et al. (2015) data have a similar effect in the cool dwarf star regime. This figure demonstrates that the inclusion of the Mann et al. (2015) and C3K spectra is important for the interpolation of stars outside the confines of the training set.

3.4. Applications of SPI

As discussed previously, SPI can be used to flag stars with potentially inaccurate stellar parameters. More generally, stars that are outliers with respect to their SPI prediction could be used to uncover other unusual behavior, such as variability or peculiar abundance patterns.

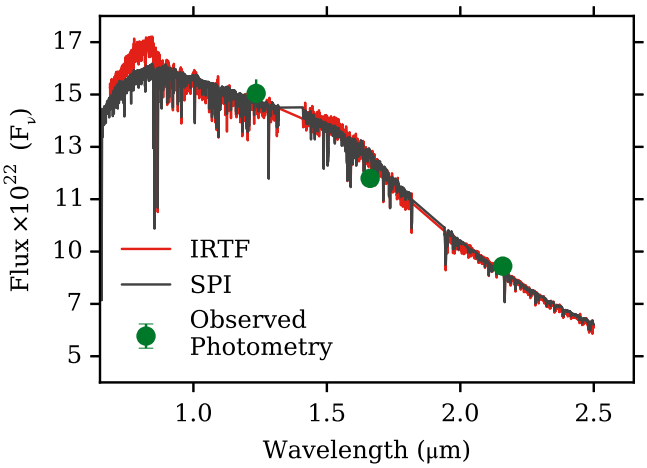

Figure 20. Demonstration of the "self-calibration" possibilities with SPI. The observed spectrum (red) for the star, HD 004307, has an unphysical artifact at ∼0.8 μm that is due to nebulosity near the standard star. Since this issue only affected a small subset, 4%, of the stellar library, we can use SPI to obtain a spectrum for HD 004307 and others like it without the unphysical feature. This is shown in the interpolated spectrum (black) that is largely the same as the observed spectrum, but without the bump at ∼0.8 μm.

SPI also allows for "self-calibration" of the observations. By this we mean that because SPI uses the information of all the stars in the library it is possible to remove artifacts that affect a small fraction of the library stars. As we mentioned earlier, some of the stars observed for this library have an unphysical bump from standard stars with unusual spectra. Since most stars were not affected in this way, we can remove this artifact by using the model to interpolate for a spectrum for the stars that are affected. In Figure 20 we show the observed spectrum (red) for the star HD 004307 and the interpolated spectrum (black). The interpolated spectrum is consistent with the observed spectrum except for the bump seen at 0.8 μm in the observed spectrum, where the interpolated spectrum produces a more sensible behavior. In

future work we will use the self-calibration capabilities of SPI to rederive the stellar parameters for the stars presented in this work.

We emphasize that any library can be used as input for SPI. The new metallicity coverage of the Extended IRTF Library allows us to interpolate to a larger metallicity range than is possible with the original IRTF library (Rayner et al. 2009). Furthermore, the library presented in this work can be augmented with NGSL, for example. The inclusion of UV data into SPI could potentially help with modeling planet atmospheric properties.

4. Behavior of the Stellar Libraries

The main feature of the Extended IRTF Library is the expansion of near-IR coverage into the sub- and super-metallicity regimes. We would like to highlight various spectral features in the data and explore how these features depend on not just surface gravity and effective temperature, but also on metallicity. This is also an opportunity to examine the behavior of SPI beyond its ability to simply reproduce the training set spectra. Also of interest is how the empirical trends compare with the theoretical models. To explore the behavior of SPI and C3K, we computed spectra for stellar parameters along a 3 Gyr (for metallicities >-0.7) and a 13.5 Gyr (for metallicities <-0.7) MIST isochrone.

Sharp boundaries where the five different polynomial models that make up SPI join together is a concern. To ensure smoothness we took the weighted average of the different predicted fluxes for the evolutionary points (EPs) that have temperatures that are in the overlap between the cool and warm dwarf and the cool and warm giant training bounds. This means that for EPs with $\log g > 4.0$ and temperatures between 3500–4500 K we generated a flux using both the warm giant and dwarf giant models and averaged the fluxes together as weighted depending on the temperature. We did the same for the EPs with $\log g < 4.0$ and temperatures between 3000–5500 K.

In this section we analyze the metallicity dependence of key stellar features using equivalent widths. The limitations of equivalent widths are well known—they are sensitive to the definition of the psuedocontinuum, and each index is a blend of features from more than one element. Here we use equivalent widths as a way to compress the information to explore broad trends. All the equivalent widths quoted in this work are in units of Å and all wavelengths are in vacuum. We present a combination of a selection of the Lick indices defined in Table 1 Worthey et al. (1994) and Table 1 of Conroy & van Dokkum (2012).

We computed equivalent widths using the following equation,

$$\mathrm{EW} = \lambda_2 - \lambda_1 - \int_{\lambda_1}^{\lambda_2} \frac{F_i}{c_b + (\lambda_i - \lambda_b)\left(\frac{c_r - c_b}{\lambda_r - \lambda_b}\right)} d\lambda, \quad (11)$$

where λ_1 and λ_2 are the blue and red wavelength boundaries of the feature definition, λ_b and λ_r are the average wavelengths of the blue and red continuum definitions for each feature. The blue and red continuum values c_b and c_r are the integral of the flux over the wavelength range that defines the blue and red continuum.

For the observations, we made 100 realizations of each spectrum by Monte Carlo sampling the noise. For each realization we used Equation (11) to compute the equivalent width. The errors for the equivalent widths are given by the 1σ confidence values from the distribution of equivalent widths.

In Figures 21 and 22 we show equivalent-width strength versus effective temperature for different spectral features (columns) and different metallicity bins (rows). In every panel dwarf stars ($\log g > 4.0$, red) are distinguished from giant stars ($\log g \leqslant 4.0$, black). The equivalent widths for the stars in the Extended IRTF Library are shown as empty circles, the equivalent widths from the Mann et al. (2015) data are shown as empty diamonds, the SPI equivalent widths are shown as solid lines, and the C3K equivalent widths are shown as the dashed line. All data points have error bars, although in most cases, the error bars are smaller than the symbols. We do not expect a perfect match between the lines and the data points, especially for the hot effective temperatures where there can be a range of $\log g$ for fixed $T_{\rm eff}$ in the data.

4.1. Data and Empirical Trends

In this section we focus on the observations and the SPI predictions. The theoretical predictions are discussed in the following section.

Several spectral features were highlighted in Conroy & van Dokkum (2012) as means to distinguish between dwarf and giant stars: NaI0.82 μm, CaT, FeH0.99 μm KI1.17 μm, CaI1.98 μm, and CO2.30 μm (see also, e.g., Spinrad 1962; Wing & Ford 1969; Cohen 1978; Frogel et al. 1978; Kleinmann & Hall 1986; Diaz et al. 1989; Ivanov et al. 2004; Rayner et al. 2009). This ability was only assessed for solar metallicity stars, and it is of interest to know whether this behavior holds for an extended metallicity range.

In Figure 21 we show the temperature-dependent equivalent-width trends for several near-IR spectral features separated by dwarfs and giants. For the three highest-metallicity bins we can see the clear separation between dwarf and giant stars from the data alone. In all of these features there is a metallicity dependence on the temperature range over which the separation between dwarf and giant stars occurs. All of the sodium lines, NaD, NaI0.82 μm, NaI1.14 μm, and NaI2.21 μm, have equivalent widths that increase among the dwarf stars with decreasing temperature. For the dwarf stars in the $-0.7 < [\mathrm{Fe/H}] < -0.4$ this is a precipitous increase for the coolest dwarf stars, while at high metallicity there is a steadier increase over a large range in temperature.

The CO2.30 μm spectral feature remains a clear discriminator between giant and dwarf stars for the whole metallicity range, and the temperature at which the separation occurs does not qualitatively change over the metallicity range. Likewise, the overall temperature-dependent trend does not appear to change significantly for the KI1.17 μm and CaT features. The strong FeH0.99 μm feature remains *unique* to the cool dwarf stars for the entire metallicity range.

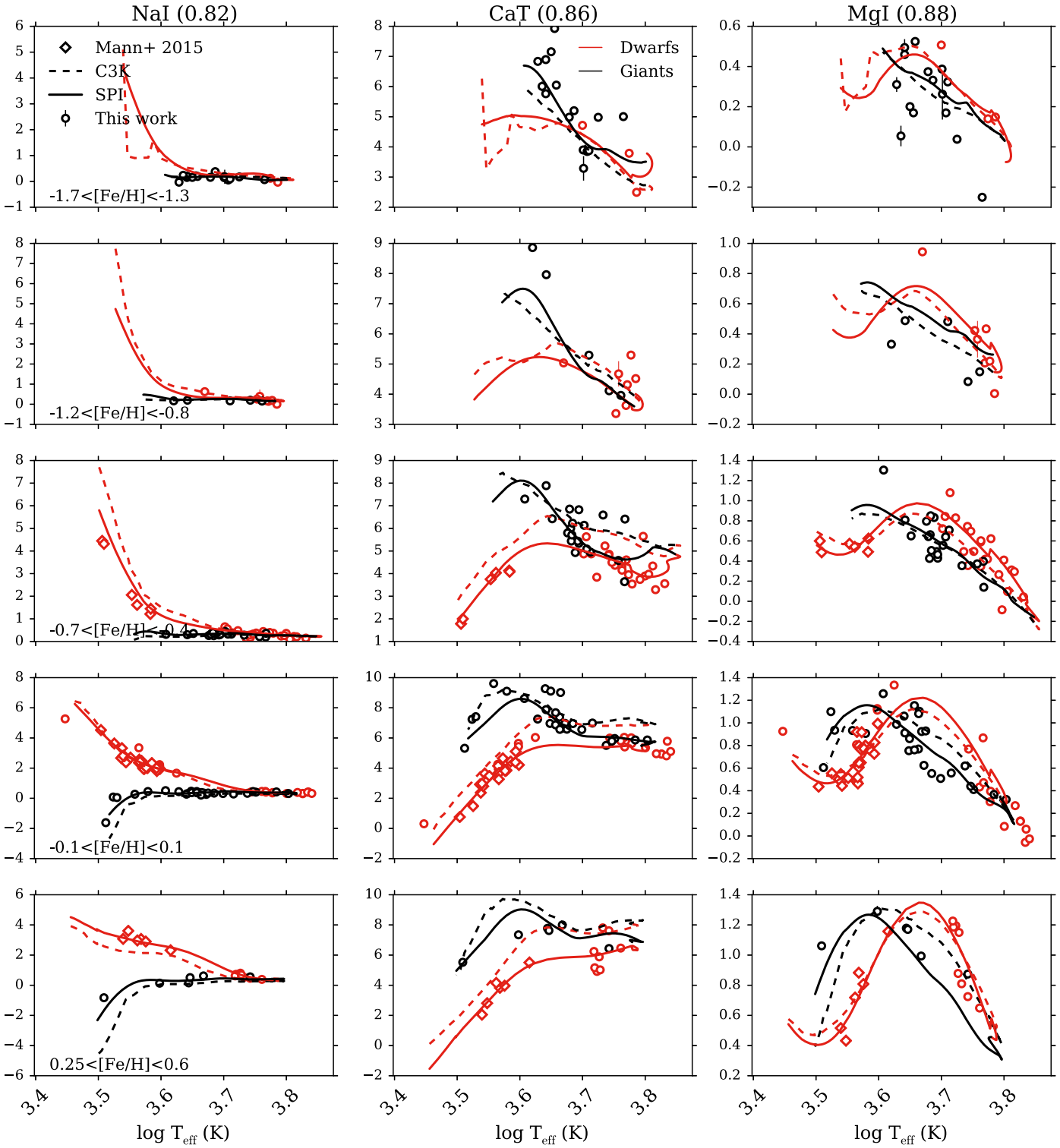

Figure 21. Dependence of selected spectral indices on effective temperature for dwarfs (log$g$ > 4.0, red) and giants (log$g$ ⩽ 4.0, black). Plotted are index strengths using the IRTF data from this work (open circles), data from Mann et al. (2015) (open diamonds), empirical prediction from SPI (solid lines), and theoretical predictions from C3K (dashed lines).

In addition to the near-IR features, we show some of the Lick indices (Worthey et al. 1994) (Figure 22) that are the classic indicators of stellar population characteristics (e.g., age and metallicity). For some spectral features there is a noticeable difference in the temperature-dependent equivalent-width trends from metallicity bin to metallicity bin (e.g., Fe4383, 4531, 5015, 5335, 5270, 5406, and 5782 Å, Ca4455 Å, Hβ, C4668 Å). However, for other spectral features (Hγ, Hδ,

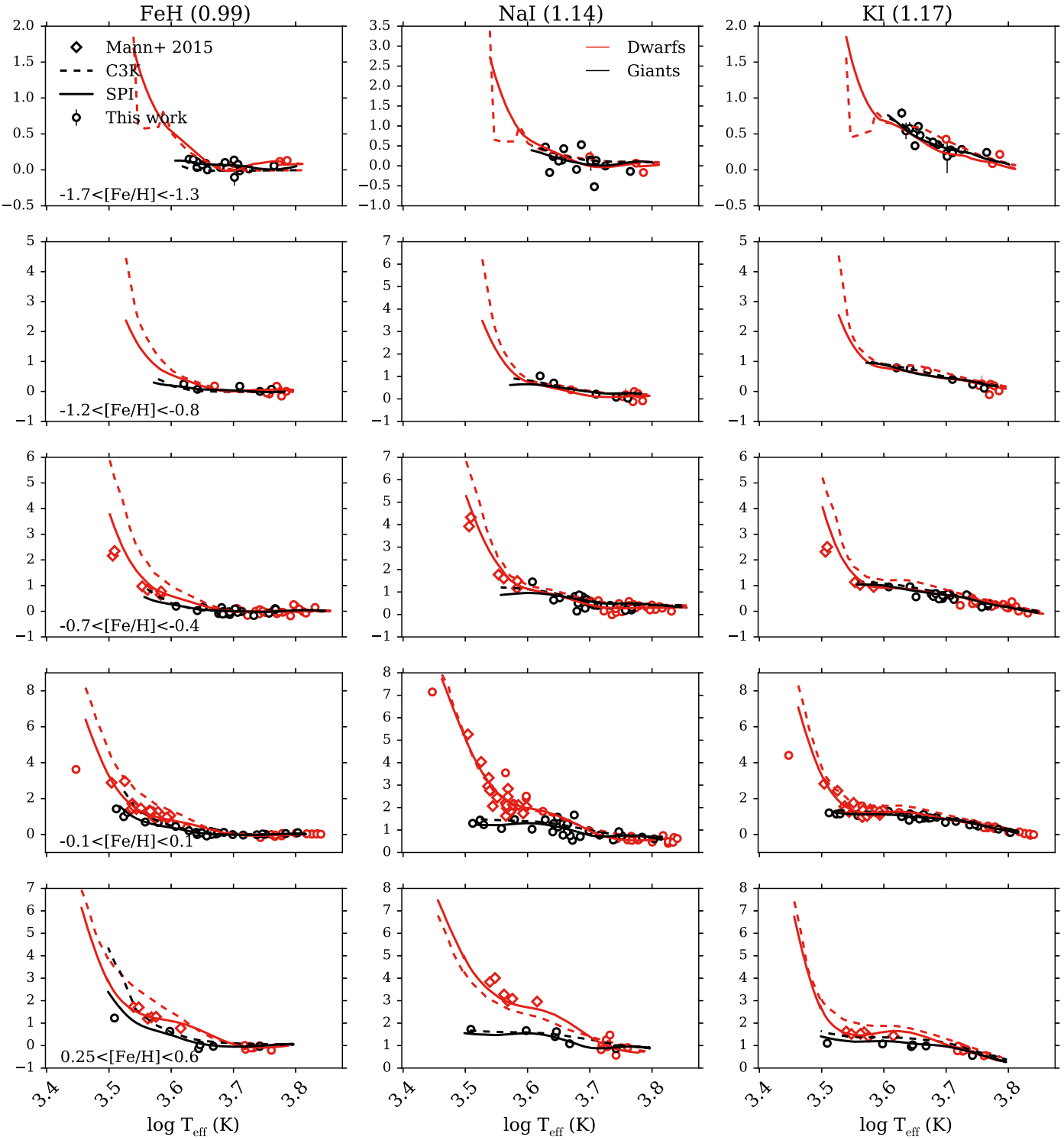

Figure 21. (Continued.)

Ca4277 Å, G4300 Å, and MgI0.88 μm), the temperature-dependent trends remain similar from metallicity bin to metallicity bin.

As we would expect from the quality assessment given in Section 3.3, SPI is consistent with the behavior of the data. Even for sparse data, e.g., the low-metallicity warm dwarf regime, SPI appears to make reasonable predictions of the behavior of all the spectral features displayed in Figures 21 and 22.

As shown in Figure 16, there are no dwarf stars cooler than 5000 K for $-1.7 < [\mathrm{Fe/H}] < -0.8$. This makes it impossible to know how accurate the SPI predicted spectra

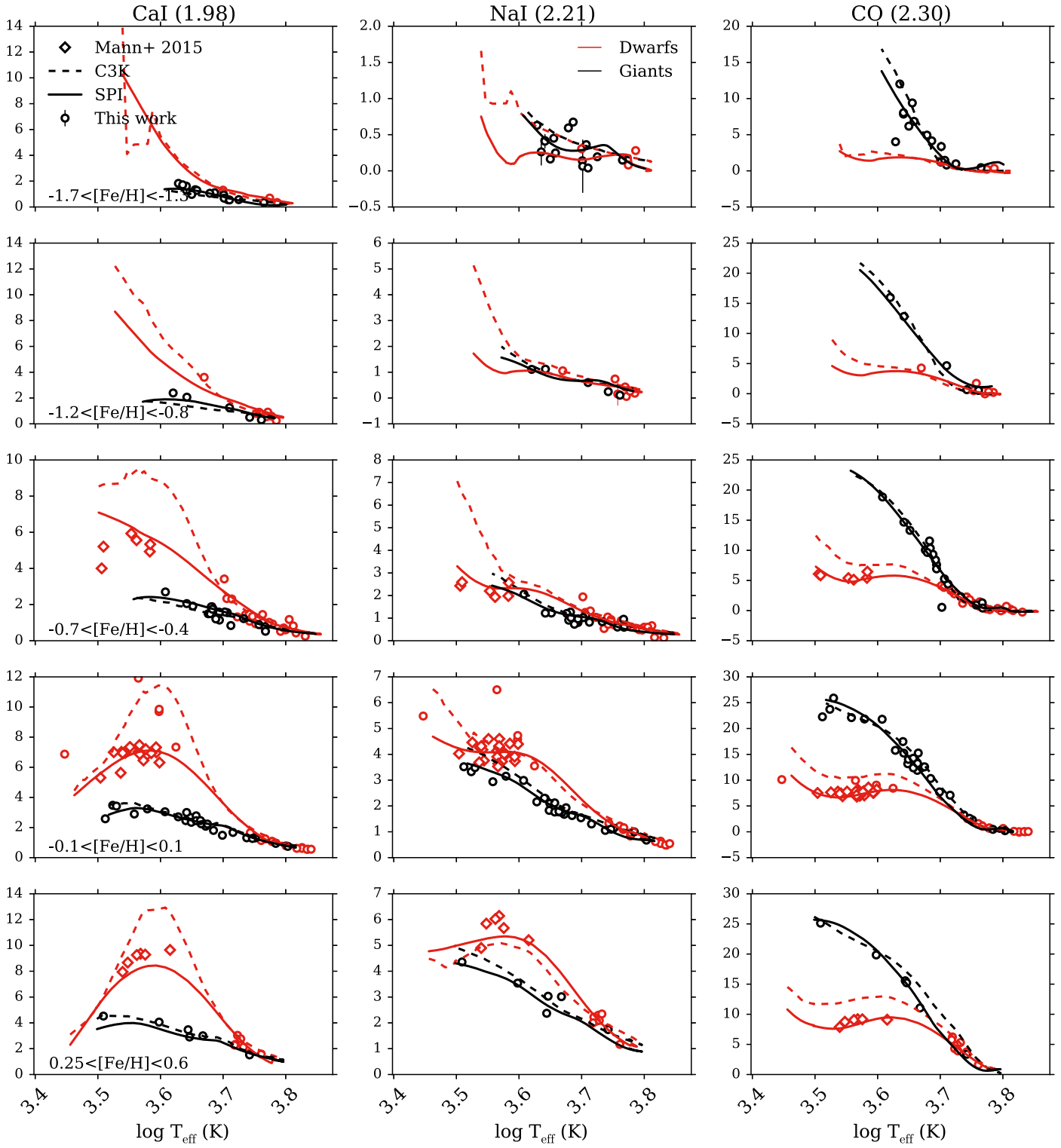

Figure 21. (Continued.)

in this regime are. However, as described earlier, the training and interpolating ranges are optimized so that SPI is able to use all three stellar parameter dimensions to make a prediction for this regime. That is, SPI is able to pull information from the predictions of both the hot and warm dwarf stars with $-1.7 < [Fe/H] < -0.8$ and the higher metallicity cool dwarf stars. Indeed, the cool dwarfs in the lowest metallicity bins have temperature-dependent trends that appear consistent with the trends in the higher metallicity regimes.

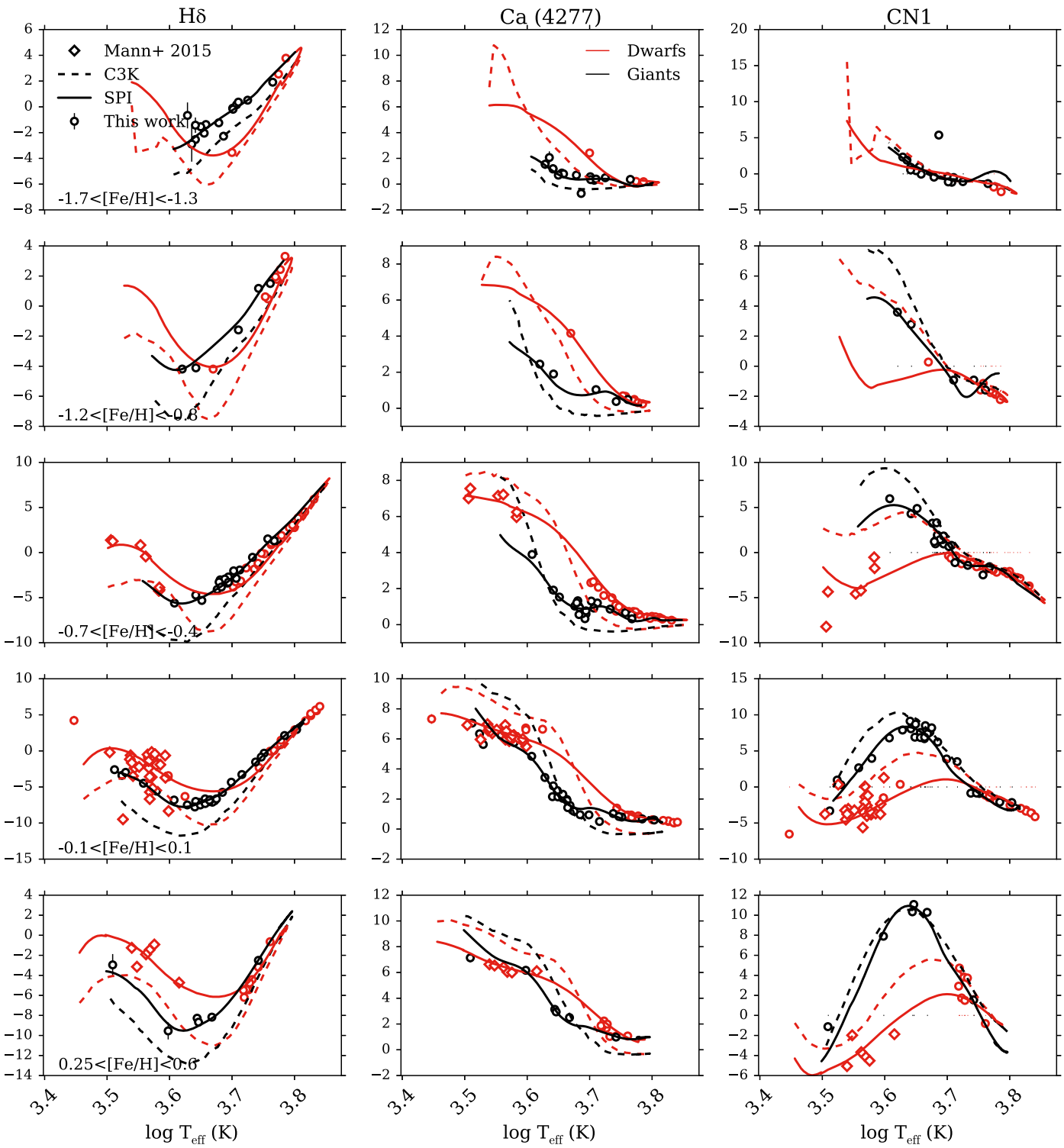

Figure 22. Continuation of Figure 21, but now using the corresponding MILES spectra for the stars in the Extended IRTF Library.

4.2. Comparison with Theoretical Trends

We now turn to a comparison between the theoretical C3K models and the empirical trends. Comparisons between models and observations have been made previously. Martins & Coelho (2007) compared the ATLAS9 (Castelli & Kurucz 2003), MARCS (Gustafsson et al. 2003), and PHOENIX (Brott & Hauschildt 2005) theoretical stellar libraries to various empirical stellar libraries. Bertone et al. (2008) compared the ATLAS9 library to the ELODIE catalog (Prugniel & Soubiran 2001), and Conroy & van Dokkum (2012) compared equivalent-width trends between theoretical and empirical stellar libraries. However, there are limitations to these studies that we can now overcome. Martins & Coelho (2007) and Conroy & van Dokkum (2012) were limited to solar metallicity stars and could not reach the coolest M dwarfs. The sample

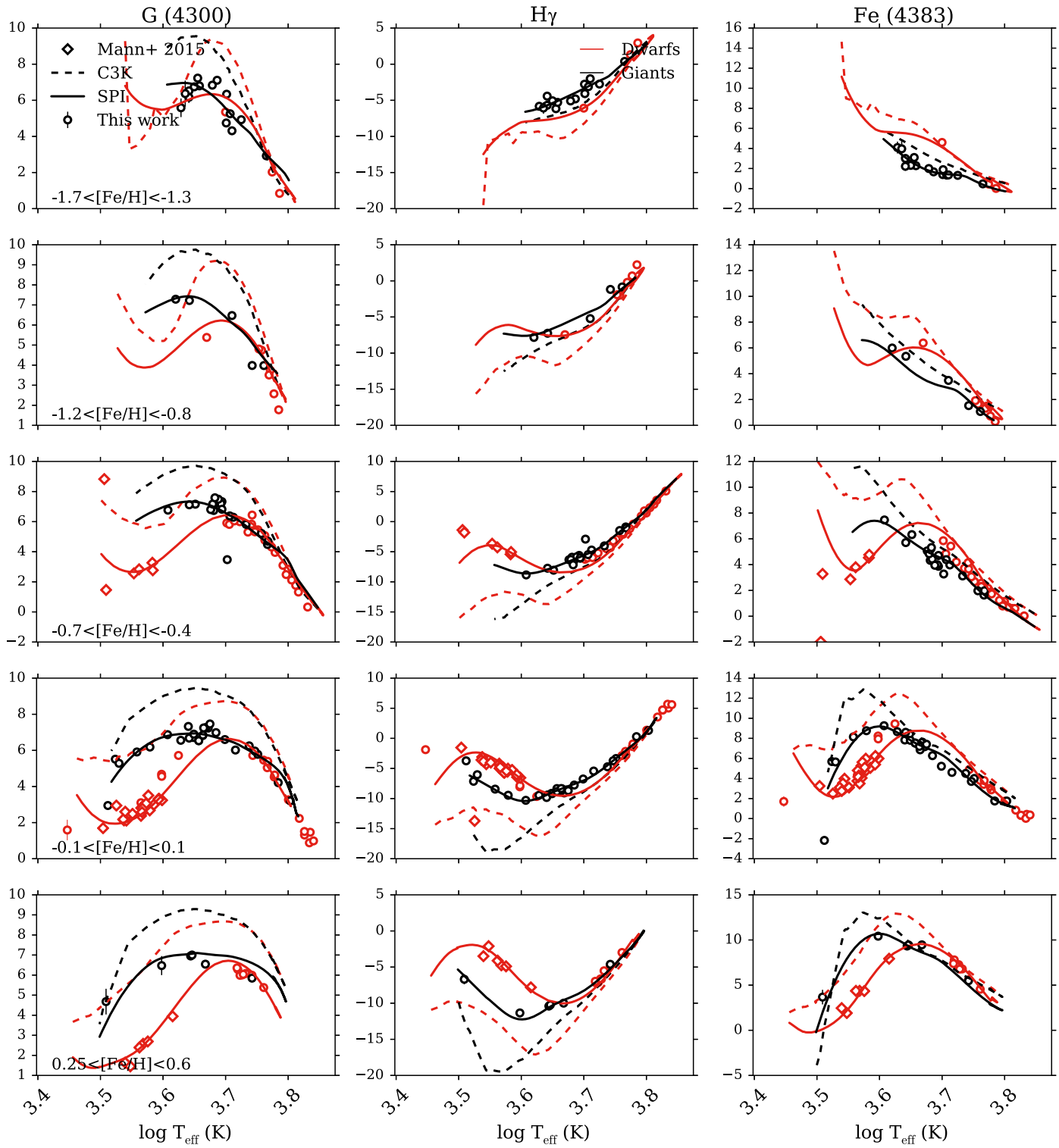

Figure 22. (Continued.)

from Bertone et al. (2008) spanned a wide range of metallicity, but was limited to stars with $T_{\rm eff} > 4000$ K and Bertone et al. (2008) did not compare specific feature strengths.

In the present case we have extended the library and the interpolator into the cool dwarf regime, and cover a much wider range in metallicity in the near-IR than was previously available. This means that we can now make explicit comparisons between the theoretical and empirical behavior in this regime.

Starting our comparison with near-IR features of the solar metallicity stars (fourth row from the top in Figure 21), we see that the theoretical predictions are consistent with the empirical trends

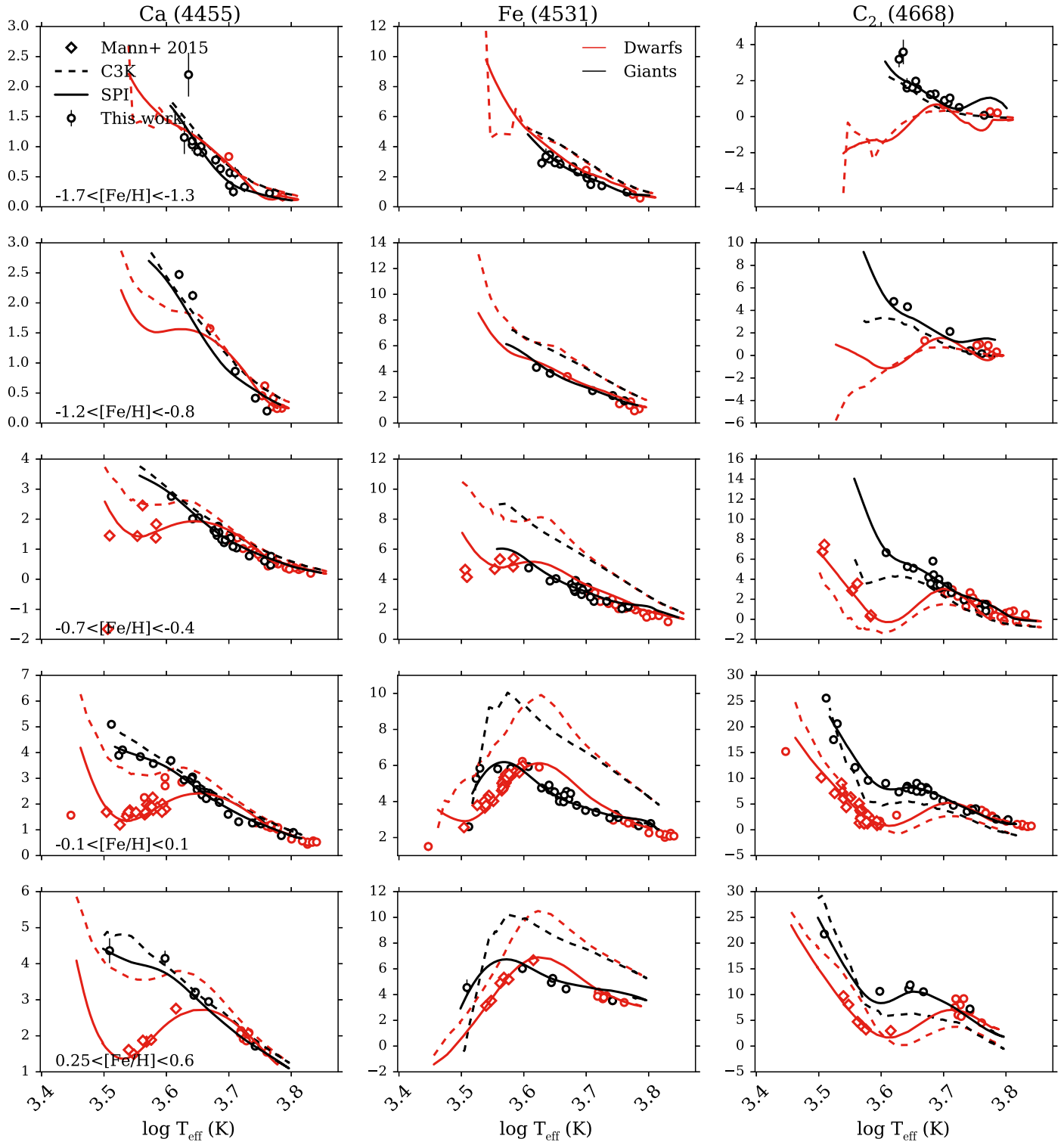

Figure 22. (Continued.)

for the NaI0.82 μm, MgI0.88 μm, NaI1.14 μm, KI1.17 μm, and NaI2.21 μm features. There is discrepancy between the theoretical predictions and empirical trends for the CaT, FeH, CaI1.98 μm, and CO2.30 μm features. With the exception of the warm dwarf regime in the CaI1.98 μm feature, however, the discrepancies are relatively small offsets in strength of the feature, with an overall similar trend with effective temperature. Furthermore, the discrepancies tend to be in the dwarf stars rather than the giant stars.

We find some small differences when comparing the consistency between the empirical and theoretical trends shown in Figure 21 with Conroy & van Dokkum (2012). First, the

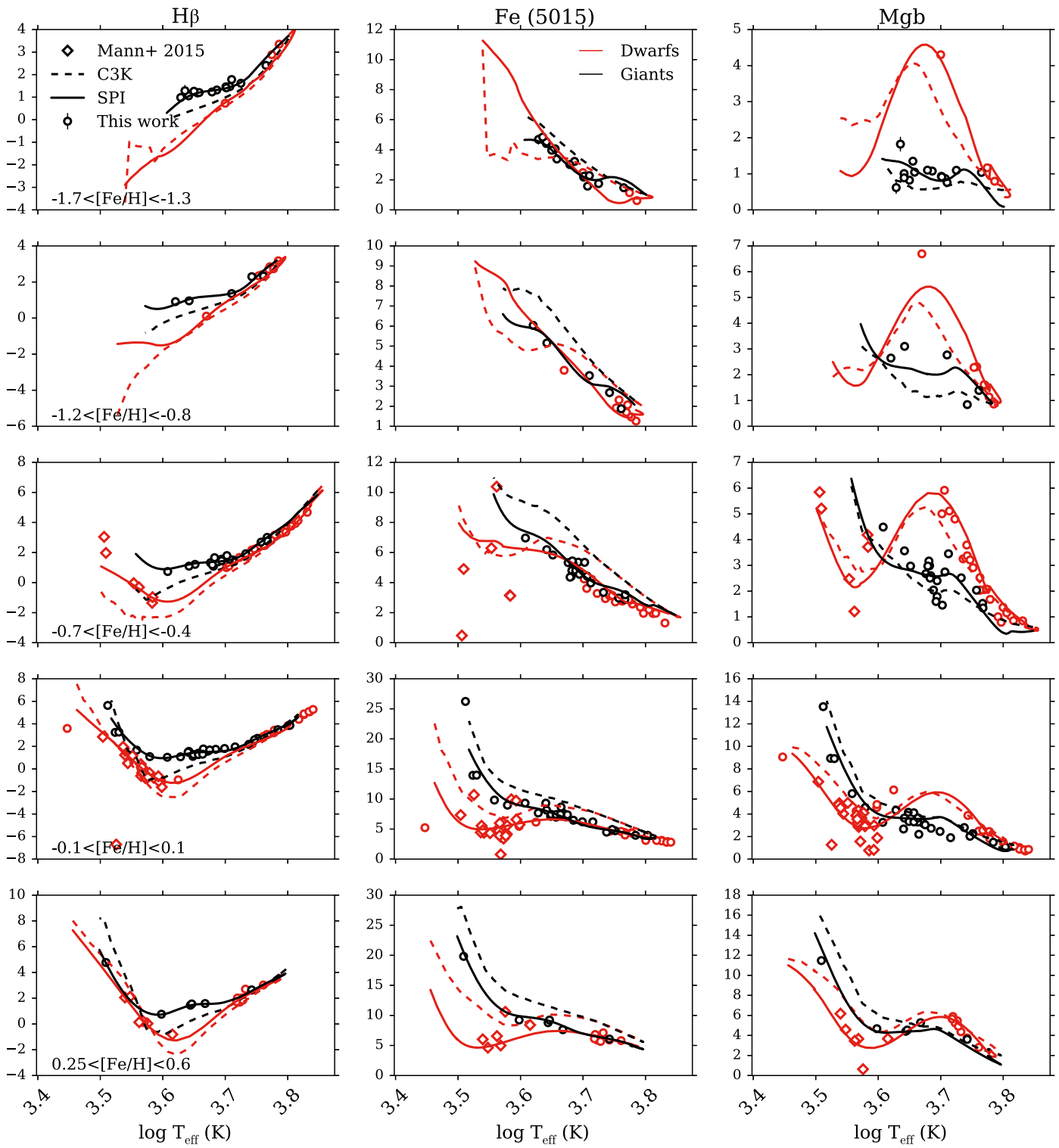

Figure 22. (Continued.)

isochrones used in this work extend to cooler temperature than those used in Conroy & van Dokkum (2012), which means we can now compare the equivalent widths of the coolest dwarfs to the theoretical libraries. For NaI0.82 μm the prediction for the equivalent widths of the coolest dwarfs is inconsistent with the data. However, the prediction for NaI0.82 μm feature strength in this work is completely consistent with the empirical trend. Similarly, in Conroy & van Dokkum (2012) the theoretical prediction for the CaT was consistent with the data and here the CaT is slightly overpredicted. This is most likely due to the modest changes that have occurred in the theoretical libraries since Conroy & van Dokkum (2012).

For solar metallicity stars in the optical, Figure 22, we find that the theoretical predictions fare worse in the optical than

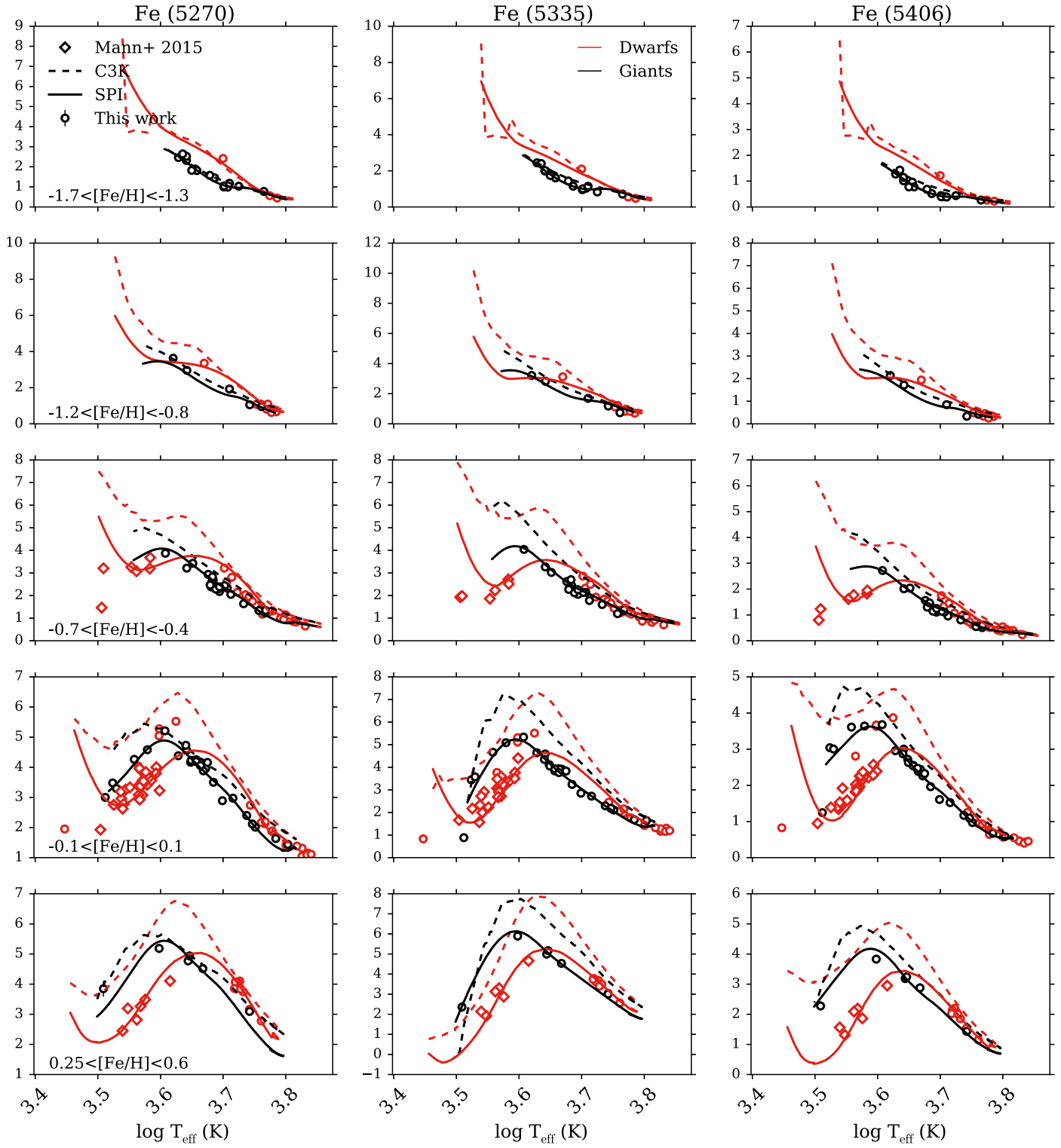

Figure 22. (Continued.)

the near-IR. We show that in the optical the overall trends predicted by the theoretical library are consistent with the empirical trend, but are often offset in predicted strength. Martins & Coelho (2007) compared the strengths of Lick indices of various empirical and theoretical libraries, and we compare the discrepancies of that work with those shown here. Here we focus on the comparison between the theoretical models from Martins et al. (2005) and the MILES library.

The C3K models underpredict the index strength for all the Balmer lines: Hδ, Hγ, and Hβ with the Hβ difference being less severe than the former two. This is consistent with the result from Martins & Coelho (2007). Furthermore, C3K overpredicts the G4300 Å band, which is again consistent with Martins &

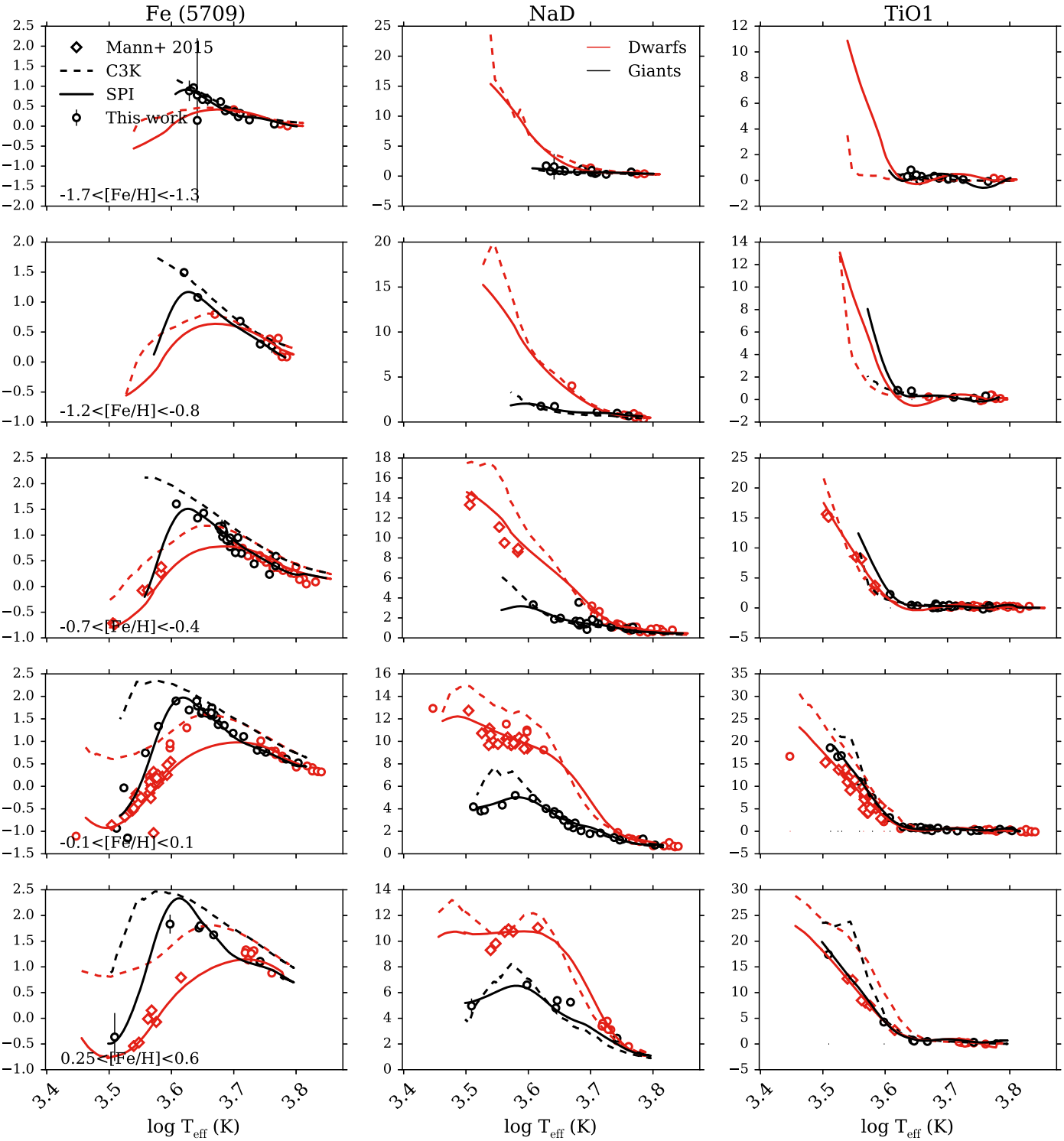

Figure 22. (Continued.)

Coelho (2007). The theoretical predictions for the iron lines are also stronger than what is observed (with the exception of the feature at 5782 Å). However, Martins & Coelho (2007) found that the inconsistency between the theoretical and empirical predictions for the iron lines was worse at cooler temperatures, which is not consistent with what we find in our comparison. Additionally, we find good agreement between the C3K predictions for the line strength of MgI0.88 μm and Mgb at temperatures where Martins & Coelho (2007) find disagreement in the magnesium lines at cool temperatures. While both C3K and the theoretical stellar spectra in Martins et al. (2005) use the ATLAS model atmospheres, C3K uses ATLAS12 and Martins et al. (2005) uses ATLAS9, so it is not unexpected that the comparisons in Martins & Coelho (2007) are different.

We now turn to a comparison of the metallicity dependence of the models and observations. For the near-IR features the consistency seen at solar metallicity holds at the other metallicities, with the exception of some of the coolest stars, particularly dwarf stars, and especially at low metallicity. For instance, the theoretical predictions for the low-metallicity cool dwarf stars is different from the empirical trend for the CaT, NaI (at 0.82 and 1.14 μm), FeH0.99 μm, CaI1.98 μm, and KI1.17 μm features. However, there is good consistency over this same regime for the CO2.30 μm and MgI0.88 μm features.

The theoretical predictions for the NaD feature are consistent with the empirical trends over all the metallicity bins, albeit slightly overpredicted in the solar metallicity bin. For some of the optical features the theoretical predictions seem to improve at lower metallicities. This includes many of the iron lines, CN1, G4300 Å, and the Balmer lines, with the exception of the coolest dwarf stars. The theoretical predictions for the TiO band are in agreement with the empirical trends at solar metallicity, but that agreement worsens at lower metallicities for the cool dwarf stars.

We emphasize that SPI is not well constrained for the low-metallicity cool dwarf regime, and therefore apparent disagreement between the models and the data should not be overinterpreted. However, the pattern of discrepancy in feature strengths for the low-metallicity cool dwarf stars does suggest that caution should be employed when supplementing the cool dwarf regime in empirical libraries with theoretical spectra. We note that the stellar population models of Conroy & van Dokkum (2012) and Lick index models (e.g., Trager et al. 2000; Thomas et al. 2003; Schiavon 2007) use theoretical models only differentially, calculating relative changes with respect to a fiducial model (the response functions), and so they are less sensitive to the absolute limitations of the models.

5. Summary

In this paper we presented a new spectroscopic stellar library, the Extended IRTF Library, which in its entirety consists of 284 stars covering a wide range of stellar parameter space, including both low and high metallicities. The stars were observed on the SpeX instrument and the spectra cover a wavelength range of 0.7–2.5 μm. All the stars included in this library were selected from the MILES optical library, providing continuous coverage from 0.35 to 2.5 μm.

In addition to the new library, we have also created a Spectral Polynomial Interpolator (SPI). This is a tool that generates a data-driven model from a subset (194 out of 284) of the highest quality library stars and can be used to produce a stellar spectrum for arbitrary values for $T_{\rm eff}$, log$g$, and [Fe/H]. With the Extended IRTF Library and SPI, we achieved the following results.

1. We find good agreement between observed and synthesized colors for all of the colors explored, including 2MASS H–K_S, J–K_S, Tycho B_T–V_T, and V_T–K_S. This agreement means that we are recovering the overall spectral shapes to within 1%–4% percent, on average.
2. We find that the empirical uncertainty of the spectra is ∼0.5% with the exception of regions that are heavily contaminated by telluric absorption or regions in the A0 V standard star that are heavily contaminated by hydrogen absorption lines. In these cases, the uncertainty is on the order of 1%–2% percent.
3. We measured the wavelength-dependent SpeX instrument resolution and found the median resolution of the stars in the library to be consistent with the nominal value of $R \approx 2000$. We also independently measured the MILES resolution and found it to be consistent with the updated value from Beifiori et al. (2011).
4. We find that stellar features retain their characteristic properties at non-solar metallicities. This includes lines sensitive to the surface gravity, such as NaI (at 0.82 μm and 1.14 μm), CaT, FeH0.99 μm, KI1.17 μm, and CO2.30 μm.
5. We find the theoretical predictions for the spectral features qualitatively agree with the observed trends. The C3K theoretical spectra in many cases reproduce the trends quantitatively as well, especially in the near-IR. Nonetheless, there are many features that show significant quantitative discrepancies between models and observations, especially in the optical.

The authors wish to recognize and acknowledge the very significant cultural role and reverence that the summit of Maunakea has always had within the indigenous Hawaiian community. We are most fortunate to have the opportunity to conduct observations from this mountain. A.V. is supported in part by a NSF Graduate Research Fellowship. C.C. acknowledges support from NASA grant NNX15AK14G, NSF grant AST-1313280, and the Packard Foundation. The authors would like to thank M. Cushing for helpful discussion and P. Sánchez-Blázquez for generously sharing data. This research has made use of the SIMBAD database, operated at CDS, Strasbourg, France, the VizieR catalog access tool, CDS, Strasbourg, France, of Astropy, a community-developed core Python package for Astronomy (Astropy Collaboration et al. 2013), matplotlib, a Python library for publication quality graphics (Hunter 2007), and of SciPy (Jones et al. 2001). The atmospheric transmission spectra was provided by Gemini Observatory.

Appendix

In Table 2 we list all the stars in the Extended IRTF Library along with their corresponding MILES ID numbers. We also include the name and spectral type of the standard star used to telluric correct and flux calibrate each library star. We give basic properties of the stars including Right Ascension and Declination, the metallicities estimated by Prugniel et al. (2011) and Sharma et al. (2016), and the 2MASS K_S magnitude. The extinction values listed in the "$E(B-V)$" column are from the values compiled in Sánchez-Blázquez et al. (2006). We also list the velocities and bolometric luminosities we computed for this work. Finally, we indicate whether each star has been flagged for potential quality, stellar parameter, or shape issues.

Table 2
The Library Stars

Name	MILES ID	Standard Star	R.A. hh	mm	ss	+/−	Decl. dd	mm	ss	[Fe/H]	K_S (mag)	$E(B-V)$ (mag)	Velocity (km s^{-1})	log L_{bol} ($L_\odot$)	Q^1 Flag	P^2 Flag	S^3 Flag
HD 225239	0003F	HD 007215-A0V	00	04	53.7603	+	34	39	35.259	−0.51	4.44	0.050	−48.2	0.75	0	0	1
HD 000448	0009F	CCDM J00209+1059AB-A0V	00	09	02.4241	+	18	12	43.066	0.02	3.32	0.025	−15.9	1.55	0	1	0
BD+130013	0010F	HD 007215-A0V	00	12	30.3109	+	14	33	48.678	−0.75	6.24	0.011	−24.0	−0.15	0	0	0
HD 001326B	0012F	HD 001561-A0Vs	00	18	25.498	+	44	01	37.64	−0.57	5.95	0.001	−7.3	−2.45	1	0	0
HD 001461	0013F	HD 013936-A0V	00	18	41.8672	−	08	03	10.802	0.19	4.9	0.044	−37.7	0.08	0	0	0
HD 001918	0014F	HD 001561-A0Vs	00	23	43.2412	+	45	05	20.892	−0.4	5.23	0.037	59.5	2.05	0	0	0
HD 003567	0022F	HD 001154-A0V	00	38	31.9474	−	08	18	33.395	−1.14	7.89	0.000	−41.4	0.22	0	0	0
HD 003546	0023F	HD 006457-A0Vn	00	38	33.3461	+	29	18	42.313	−0.66	2.07	0.000	−58.0	1.68	0	0	0
HD 003574	0024F	HD 001561-A0Vs	00	39	09.8946	+	49	21	16.521	0.01	1.6	0.048	−13.9	3.82	0	0	0
HD 004307	0028F	HD 015130-A0V	00	45	28.6878	−	12	52	50.914	−0.24	4.62	0.000	−25.2	0.44	0	0	0
HD 004744	0033F	HD 006457-A0Vn	00	49	52.7904	+	30	27	01.028	−0.74	4.93	0.010	−148.3	1.61	0	0	0
HD 004906	0034F	HD 006229-G5III	00	51	14.0528	+	18	47	25.153	−0.66	6.77	0.028	−127.4	0.65	0	0	0
NGC288-77	0897C	HD 004329-A0V	00	52	43.00	−	26	27	28.0	−1.32	10.01	0.030	−31.8	2.85	0	0	0
HD 005384	0036F	HD 013936-A0V	00	55	42.3993	−	07	20	49.742	0.18	2.42	0.012	−49.1	2.5	1	0	0
HD 005780	0038F	CCDM J00209+1059AB-A0V	00	59	23.3126	+	00	46	43.563	−0.71	4.22	0.000	−90.0	2.41	0	0	1
HD 006229	0043F	HD 006457-A0Vn	01	03	36.4553	+	23	46	06.377	−1.14	6.57	0.000	−103.5	1.51	0	0	1
HD 006497	0045F	HD 223386-A0V	01	07	00.1738	+	56	56	05.904	0.04	3.88	0.014	−75.5	1.42	0	0	0
HD 006834	0049F	HD 007215-A0V	01	09	35.2623	+	39	46	51.765	−0.58	7.29	0.005	7.8	0.38	0	0	1
HD 006755	0050F	HD 223386-A0V	01	09	43.0646	+	61	32	50.190	−1.58	5.66	0.060	−286.6	1.19	0	0	0
HD 006833	0051F	HD 001561-A0Vs	01	09	52.2648	+	54	44	20.278	−0.84	4.04	0.047	−241.6	1.95	0	0	1
HD 007106	0052F	HD 007215-A0V	01	11	39.6364	+	30	05	22.690	−0.02	2.15	0.011	19.1	1.59	0	0	0
HD 007351	0053F	HD 007215-A0V	01	14	04.9061	+	28	31	46.471	−0.35	1.64	0.048	−8.7	3.32	0	0	0
HD 007672	0056F	CCDM J00209+1059AB-A0V	01	16	36.2886	−	02	30	01.321	−0.42	3.38	0.076	23.7	1.55	0	1	0
HD 008724	0057F	HD 006457-A0Vn	01	26	17.5949	+	17	07	35.127	−1.63	5.64	0.020	−112.8	1.97	0	1	0
HD 009919	0064F	HD 006457-A0Vn	01	37	05.9152	+	12	08	29.518	−0.35	4.58	0.006	38.4	0.72	0	0	0
HD 010700	0067F	HD 013936-A0V	01	44	04.0833	−	15	56	14.926	−0.46	1.79	0.004	−23.4	−0.32	1	0	1
HD 011397	0072F	HD 021875-A0V	01	51	40.5274	−	16	19	03.526	−0.58	7.27	0.070	2.7	−0.16	0	0	0
BD+290366	0077F	BD+320409-A0V	02	10	24.5278	+	29	48	23.669	−0.95	7.22	0.00	45.0	−0.1	0	0	0
HD 013520	0080F	HD 013869-A0V	02	13	13.3238	+	44	13	53.954	−0.27	1.33	0.020	−46.7	2.77	0	0	0
BD-010306	0081F	HD 018571-A0V	02	14	40.2986	−	01	12	05.119	−0.89	7.52	0.000	18.0	−0.11	0	0	0
HD 013783	0082F	HD 012468-A0V	02	16	49.2129	+	64	57	09.380	−0.49	6.59	0.000	−31.8	−0.21	0	0	0
HD 014802	0084F	HD 017224-A0V	02	22	32.5464	−	23	48	58.779	−0.07	3.74	0.000	−14.2	0.47	0	1	0
HD 016673	0092F	HD 015130-A0V	02	40	12.4215	−	09	27	10.361	0.0	4.53	0.005	−10.2	0.26	0	0	1
HD 017361	0098F	HD 013869-A0V	02	47	54.5414	+	29	14	49.613	0.02	2.1	0.020	−18.9	1.6	0	0	0
HD 017491	0099F	HD 013936-A0V	02	47	55.9222	−	12	27	38.322	−0.15	0.36	0.034	−11.7	3.33	0	0	0
HD 017548	0101F	HD 021686-A0Vn	02	48	51.8520	−	01	30	34.747	−0.53	6.76	0.008	−35.5	0.13	0	0	0
HD 018191	0103F	HD 016811-A0V	02	55	48.4980	+	18	19	53.902	−0.05	−0.87	0.164	81.8	3.15	0	0	0
HD 019373	0108F	HD 021038-A0V	03	09	04.0198	+	49	36	47.799	0.11	2.72	0.034	56.3	0.29	0	0	0
HD 020893	0114F	HD 023258-A0V	03	22	45.2400	+	20	44	31.438	0.07	2.19	0.031	−21.6	2.08	0	0	0
BD+430699	0115F	HD 021038-A0V	03	23	33.4875	+	43	57	26.222	−0.38	6.54	0.007	6.6	−0.69	0	0	0
HD 021017	0116F	HD 023258-A0V	03	24	18.4745	+	24	43	26.617	0.07	2.89	0.004	−24.5	1.45	1	0	0
HD 021197	0117F	HD 025175-A0V	03	24	59.7314	−	05	21	49.523	0.13	5.12	0.072	−36.8	−0.6	0	0	1
HD 021581	0118F	HD 018571-A0V	03	28	54.486	−	00	25	03.11	−1.51	6.41	0.000	100.5	1.35	0	0	0
HD 022879	0123F	HD 031295-A3Va	03	40	22.0641	−	03	13	01.124	−0.8	5.18	0.000	118.6	0.05	0	0	0
HD 023439A	0127F	HD 021038-A0V	03	47	02.113	+	41	25	38.06	−0.9	6.12	0.010	34.5	−1.0	0	0	0
HD 023439B	0128F	HD 021038-A0V	03	47	02.636	+	41	25	42.56	−1.09	6.35	0.010	27.3	−1.0	0	0	0
HD 023841	0130F	HD 021686-A0Vn	03	48	30.7665	+	09	38	45.410	−0.66	3.8	0.053	−94.1	2.42	0	0	1

Table 2
(Continued)

Name	MILES ID	Standard Star	R.A. hh	mm	ss	+/−	Decl. dd	mm	ss	[Fe/H]	K_S (mag)	$E(B-V)$ (mag)	Velocity (km s^{-1})	log L_{bol} ($L_\odot$)	Q^1 Flag	P^2 Flag	S^3 Flag
HD 024341	0133F	HD 029526-A0V	03	54	51.1901	+	52	25	11.526	−0.62	6.11	0.023	99.2	0.3	0	0	0
HD 024421	0134F	HD 029526-A0V	03	55	37.0801	+	52	13	36.550	−0.29	5.47	0.003	−56.4	0.32	0	0	0
HD 025673	0138F	HD 021875-A0V	04	04	20.3036	−	04	39	18.471	−0.4	7.46	0.006	81.3	−0.48	0	0	0
HD 026297	0139F	HD 021875-A0V	04	09	03.4176	−	15	53	27.063	−1.79	4.63	0.017	25.1	2.73	0	0	0
HD 284248	0143F	HD 023258-A0V	04	14	35.5155	+	22	21	04.261	−1.55	7.87	0.000	303.3	0.09	0	0	0
BD-060855	0144F	HD 025792-A0V	04	14	58.1083	−	05	37	48.856	−0.69	8.79	0.01	324.8	−0.54	0	0	0
HD 027126	0147F	HD 025152-A0V	04	18	29.5492	+	35	59	30.080	−0.38	6.64	0.000	−56.5	−0.09	0	0	1
HD 027371	0149F	HD 032358-B6V	04	19	47.6038	+	15	37	39.515	0.15	1.52	0.014	65.2	1.94	0	0	0
HD 027771	0150F	HD 025175-A0V	04	23	32.3310	+	14	40	13.717	0.27	7.14	0.000	20.1	−0.33	0	0	0
HD 285773	0153F	HD 025175-A0V	04	29	31.6067	+	17	53	35.466	0.25	7.05	0.000	9.8	−0.37	0	0	0
BD+501021	0158F	HD 029526-A0V	04	38	07.8341	+	51	10	12.467	−0.65	8.28	0.060	−31.8	−0.55	0	0	0
HD 030649	0162F	HD 031069-A0V	04	51	43.5572	+	45	50	02.971	−0.48	5.44	0.000	20.0	0.08	0	0	0
HD 031128	0163F	HD 034868-A0V	04	52	09.9101	−	27	03	50.950	−1.45	7.74	0.000	85.1	−0.11	0	0	0
HD 031295	0166F	HD 031411-A0V	04	54	53.7287	+	10	09	02.995	−0.73	4.42	0.100	−17.0	1.15	0	1	0
HD 031767	0167F	HD 034317-A0V	04	58	32.9021	+	01	42	50.458	−0.02	1.34	0.101	4.4	3.36	0	0	0
HD 033608	0173F	HD 031411-A0V	05	11	19.1768	−	02	29	26.817	0.21	4.82	0.000	62.2	0.62	0	0	0
HD 034411	0176F	HD 031069-A0V	05	19	08.4742	+	40	05	56.582	0.08	3.04	0.000	32.8	0.27	0	0	0
HD 035179	0178F	HD 035505-A0V	05	22	21.0066	−	14	23	50.061	−0.6	7.1	0.000	13.7	1.96	0	0	0
M79_153	0915C	HD 040972-A0V	05	24	09.1300	−	24	34	16.1000	−1.6	9.61	0.010	−19.9	−1.0	0	0	1
M79_160	0916C	HD 040972-A0V	05	24	09.4000	−	24	33	29.9000	−1.6	10.26	0.010	216.4	3.06	0	0	0
M79_223	0917C	HD 040972-A0V	05	24	18.4860	−	24	31	43.3800	−1.6	9.83	0.010	188.7	3.19	0	0	0
HD 035296	0180F	HD 035036-A0V	05	24	25.4638	+	17	23	00.716	0.01	4.04	0.000	78.5	0.1	0	0	1
HD 035620	0181F	HD 035036-A0V	05	27	38.8860	+	34	28	33.212	0.1	2.1	0.115	52.2	2.48	0	1	0
HD 036003	0182F	HD 037887-B9.5V	05	28	26.0960	−	03	29	58.399	−0.15	4.88	0.011	−19.9	−0.71	0	0	0
HD 036395	0183F	HD 037887-A0V	05	31	27.3959	−	03	40	38.031	−0.05	4.04	0.006	−24.3	−1.27	0	0	0
HD 037160	0184F	HD 035656-B9V	05	36	54.3881	+	09	17	26.409	−0.64	1.81	0.000	124.2	1.47	0	0	0
HD 037828	0187F	HD 035505-A0V	05	40	54.6451	−	11	12	00.191	−1.41	4.06	0.020	188.5	2.55	0	0	0
HD 037984	0189F	HD 034317-A0V	05	42	28.6327	+	01	28	28.665	−0.52	2.21	0.010	80.4	2.02	0	0	0
HD 038393	0191F	* 10 lep-A0V	05	44	27.7908	−	22	26	54.180	−0.09	2.51	0.000	−17.8	0.28	0	0	0
HD 039364	0196F	* 10 Lep-A0V	05	51	19.2961	−	20	52	44.723	−0.74	1.4	0.000	81.9	1.54	0	0	0
HD 039833	0198F	HD 039953-A0V	05	55	01.958	−	00	30	28.69	0.18	6.15	0.010	6.8	0.08	0	0	0
HD 041312	0203F	HD 042729-A0V	06	03	15.6045	−	26	17	04.355	−0.75	1.69	0.030	149.4	2.43	1	0	0
HD 042543	0211F	HD 046553-A0Vnn	06	12	19.0986	+	22	54	30.642	0.18	0.81	0.606	51.6	5.19	0	0	0
HD 043380	0215F	HD 045105-A0V	06	18	16.8650	+	46	21	37.593	−0.05	3.65	0.019	−27.5	1.74	1	0	0
HD 044007	0216F	HD 038206-A0V	06	18	48.5271	−	14	50	43.425	−1.53	5.7	0.000	162.1	1.3	0	0	1
HD 044030	0219F	HD 046553-A0Vnn	06	20	35.3327	+	25	36	29.306	−0.51	4.14	0.107	−132.7	2.65	0	0	0
HD 045282	0222F	HD 045137-A0V	06	26	40.7734	+	03	25	29.794	−1.42	6.09	0.000	281.2	1.11	0	0	0
HD 045829	0223F	HD 043583-A0V	06	30	02.2945	+	07	55	16.009	0.11	3.35	0.228	58.3	4.06	0	0	0
HD 047914	0227F	HD 045105-A0V	06	43	04.9710	+	44	31	28.022	0.04	1.71	0.033	−43.7	2.2	1	0	0
HD 048682	0232F	HD 045105-A0V	06	46	44.3381	+	43	34	38.726	0.11	4.13	0.000	−1.0	0.13	0	1	0
HD 054719	0245F	HD 058296-A0V	07	11	08.3704	+	30	14	42.583	0.13	1.68	0.020	−2.6	2.3	0	0	0
HD 055496	0246F	HD 056341-A0V	07	12	11.3771	−	22	59	00.619	−1.48	5.93	0.020	305.7	2.15	0	0	0
HD 056274	0249F	HD 067725-B8V	07	15	50.7956	−	13	02	58.131	−0.53	6.2	0.079	80.9	−0.07	0	0	1
HD 058551	0255F	HD 064648-A0Vs	07	26	50.2521	+	21	32	08.320	−0.42	5.24	0.000	14.3	0.25	0	0	0
HD 059374	0257F	CCDM J07274+1519AB-A0V	07	30	29.0172	+	18	57	40.620	−0.82	6.98	0.000	75.7	−0.05	0	0	1
HD 059984	0259F	HD 067725-B8V	07	32	05.7628	−	08	52	52.776	−0.68	4.48	0.023	14.9	0.37	0	1	0
BD-011792	0266F	HD 079107-A0V	07	39	50.1104	−	01	31	20.372	−0.81	7.04	0.000	56.8	0.89	0	0	0

Table 2
(Continued)

Name	MILES ID	Standard Star	R.A. hh	mm	ss	+/−	Decl. dd	mm	ss	[Fe/H]	K_S (mag)	$E(B-V)$ (mag)	Velocity (km s^{-1})	log L_{bol} ($L_\odot$)	Q^1 Flag	P^2 Flag	S^3 Flag
HD 061935	0270F	HD 056525-A0V	07	41	14.8325	−	09	33	04.071	−0.06	1.64	0.015	16.9	1.74	0	0	0
BD+002058A	0272F	HD 079108-A0V	07	43	43.9549	−	00	04	00.899	−1.22	8.84	0.02	−54.4	−0.07	0	0	0
BD-182065	0278F	HD 067213-A0V	07	52	38.0071	−	18	35	37.734	−0.71	7.27	0.000	111.3	−1.0	0	0	0
HD 063791	0281F	HD 237611-A0V	07	54	28.7238	+	62	08	10.761	−1.62	5.43	0.03	−128.8	2.89	0	0	1
HD 065583	0285F	HD 064648-A0Vs	08	00	32.1289	+	29	12	44.471	−0.65	5.09	0.000	−10.8	−0.34	0	0	0
HD 073898	0307F	HD 079290-A0V	08	39	42.4741	−	29	33	39.898	−0.56	2.9	0.043	1.2	1.75	0	0	1
HD 073394	0309F	HD 063586-A0Vn	08	40	22.5437	+	51	45	06.558	−1.49	4.96	0.002	−80.2	2.34	0	0	0
HD 074011	0312F	HD 071906-A0V	08	42	30.8192	+	34	11	15.699	−0.56	5.79	0.006	83.0	0.31	0	0	0
HD 074377	0316F	HD 071906-A0V	08	45	10.3977	+	41	40	18.615	−0.37	6.13	0.002	−9.2	−0.5	0	0	0
HD 074721	0317F	HD 075137-A0V	08	45	59.2615	+	13	15	48.607	−1.32	8.52	0.032	75.7	2.84	0	0	0
HD 074462	0319F	* 39 UMa-A0III	08	48	20.6521	+	67	26	59.893	−1.4	6.05	0.020	−206.7	2.05	0	0	0
HD 075318	0320F	HD 079108-A0V	08	49	21.2072	+	03	41	02.392	−0.13	6.08	0.000	64.0	−0.12	0	0	0
HD 075691	0321F	* eta pyx-A0V	08	50	31.9228	−	27	42	35.442	−0.16	1.14	0.033	15.0	2.11	0	0	0
HD 076151	0323F	HD 073687-A0V	08	54	17.9480	−	05	26	04.058	0.15	4.46	0.000	46.6	0.0	0	0	0
HD 076932	0325F	HD 073687-A0V	08	58	43.9331	−	16	07	57.813	−0.82	4.36	0.000	91.2	0.21	0	0	0
HD 076813	0330F	HD 071906-A0V	08	59	32.6543	+	32	25	06.809	−0.06	3.15	0.331	4.1	2.02	0	1	0
HD 077338	0331F	HD 073495-A0V	09	01	12.4941	−	25	31	37.426	0.36	6.76	0.029	8.3	−0.31	0	1	0
HD 077236	0332F	HD 079108-A0V	09	01	14.7956	−	02	33	41.689	−0.89	4.64	0.000	144.3	1.98	0	0	0
HD 078737	0337F	HD 073495-A0V	09	09	03.3696	−	27	01	49.314	−0.46	7.74	0.005	1.5	0.65	0	1	0
HD 081029	0345F	HD 079108-A0V	09	23	15.7647	+	03	30	04.997	−0.08	6.49	0.065	60.8	1.03	0	1	0
HD 081797	0347F	HD 084886-A0V	09	27	35.2427	−	08	39	30.958	0.01	−1.13	0.012	0.3	2.89	1	0	0
HD 082074	0349F	HD 079108-A0V	09	29	32.4157	−	04	14	47.887	−0.43	4.15	0.009	−50.0	0.95	0	0	0
HD 082734	0351F	HD 082724-A0V	09	33	12.4596	−	21	06	56.601	0.2	2.83	0.031	40.7	2.09	0	0	0
HD 083212	0354F	HD 083104-A0V	09	36	19.9522	−	20	53	14.756	−1.64	5.61	0.025	97.5	2.83	0	0	0
HD 083632	0358F	HD 089239-A0V	09	40	34.0571	+	26	00	13.967	−0.85	4.72	0.069	98.3	3.4	0	0	0
HD 233666	0359F	HD 092728-A0III	09	42	19.4752	+	53	28	26.156	−1.62	7.37	0.040	−63.7	2.82	0	1	0
HD 086986	0368F	HD 089239-A0V	10	02	29.5658	+	14	33	25.189	−1.7	7.5	0.030	42.5	1.24	0	0	0
HD 087141	0369F	* 39 ma-A0V	10	04	36.3229	+	53	53	30.170	0.09	4.5	0.030	−16.4	1.01	0	0	0
HD 088230	0373F	HD 099966-A0V	10	11	22.1405	+	49	27	15.256	−0.01	2.96	0.000	−64.0	−0.96	0	0	0
HD 088446	0374F	HD 023366-A0V	10	12	19.0769	+	17	17	57.044	−0.51	6.45	0.000	91.6	0.41	0	0	0
HD 088725	0375F	HD 097585-A0V	10	14	08.3341	+	03	09	04.677	−0.64	6.15	0.000	−60.1	−0.1	0	0	0
HD 088986	0378F	HD 089239-A0V	10	16	28.0831	+	28	40	56.927	0.04	4.88	0.000	27.4	0.37	0	0	0
HD 089010	0379F	HD 089239-A0V	10	16	32.2887	+	23	30	11.144	0.0	4.34	0.025	−48.0	0.53	0	0	0
HD 091347	0389F	HD 099966-A0V	10	33	50.5558	+	49	11	10.222	−0.44	6.05	0.000	−38.7	0.04	0	0	0
HD 094028	0394F	HD 088960-A0Vn	10	51	28.1244	+	20	16	38.960	−1.3	6.83	0.000	85.1	−0.03	0	0	0
BD-103166	0395F	BD+172473-G5	10	58	28.7798	−	10	46	13.386	0.42	8.12	0.077	63.0	−0.38	0	0	0
HD 095128	0396F	HD 098989-A0V	10	59	27.9728	+	40	25	48.920	0.02	3.75	0.000	18.9	0.14	0	0	0
HD 096360	0400F	* 86 UMa-A0V	11	07	52.7864	+	68	21	58.864	−0.02	2.77	0.139	−124.5	2.61	0	0	0
BD+362165	0401F	HD 097585-A0V	11	12	47.9995	+	35	43	43.899	−1.45	8.5	0.00 +	−154.7	0.32	0	1	0
HD 097916	0405F	HD 097585-A0V	11	15	54.2297	+	02	05	12.083	−0.73	8.02	0.000	61.5	0.3	0	0	1
HD 097855	0406F	HD 092728-A0III	11	16	04.0330	+	52	46	23.376	−0.39	5.28	0.021	−6.7	0.35	0	0	0
HD 098553	0408F	HD 099459-A0V	11	20	11.5950	−	19	34	40.457	−0.44	6.08	0.000	−38.0	−0.1	0	0	1
HD 099109	0409F	HD 097585-A0V	11	24	17.3588	−	01	31	44.664	0.4	7.16	0.088	81.3	−0.21	0	0	0
HD 100906	0414F	HD 101369-A0V	11	36	42.4113	−	18	58	10.585	−0.46	7.49	0.000	77.7	2.06	0	0	0
BD+511696	0419F	HD 099966-A0V	11	46	35.1545	+	50	52	54.682	−1.3	8.31	0.005	102.7	−0.26	0	0	0
HD 102328	0420F	HD 092728-A0III	11	46	55.6221	+	55	37	41.485	0.28	2.63	0.050	58.5	1.58	0	0	0
HD 102634	0421F	* 69 Leo-A0V	11	49	01.281	−	00	19	07.22	0.22	4.92	0.000	−7.4	0.53	0	0	1

Table 2
(Continued)

Name	MILES ID	Standard Star	R.A. hh	mm	ss	+/−	Decl. dd	mm	ss	[Fe/H]	K_S (mag)	$E(B-V)$ (mag)	Velocity (km s^{-1})	log L_{bol} ($L_\odot$)	Q^1 Flag	P^2 Flag	S^3 Flag
HD 103095	0423F	HD 107655-A0V	11	52	58.7693	+	37	43	07.234	−1.21	4.37	0.000	−114.5	−0.68	0	0	0
HD 104307	0427F	HD 099922-A0V	12	00	42.2223	−	21	50	15.006	−0.07	3.15	0.042	96.0	2.21	0	0	0
HD 105452	0431F	HD 110902-A0V	12	08	24.8165	−	24	43	43.950	−0.19	3.31	0.028	−16.7	0.55	0	0	0
HD 105546	0432F	HD 092728-A0III	12	09	02.7208	+	59	01	05.134	−1.46	6.67	0.000	84.0	1.57	0	0	0
HD 105740	0433F	HD 107655-A0V	12	10	16.9638	+	16	22	13.363	−0.54	5.85	0.000	−30.9	1.33	0	0	0
HD 106038	0434F	HD 107655-A0V	12	12	01.3700	+	13	15	40.622	−1.25	8.76	0.000	124.5	−0.18	0	0	0
CD-2809374	0435F	HD 112305-A0V	12	14	29.7453	−	29	35	55.677	−0.76	8.12	0.010	19.5	0.34	0	0	0
HD 107213	0438F	HD 107655-A0V	12	19	29.5259	+	28	09	24.902	0.24	5.13	0.000	5.3	0.81	0	0	0
BD+172473	0439F	HD 107655-A0V	12	23	31.021	+	16	54	09.24	−1.04	8.16	0.000	54.3	−1.0	0	0	0
BD+312360	0440F	HD 107655-A0V	12	24	17.400	+	30	46	48.73	−0.79	8.83	0.00	51.8	−1.0	0	0	0
HD 108177	0441F	HD 109309-A0V	12	25	34.9550	+	01	17	02.267	−1.41	8.35	0.000	169.6	0.08	0	1	0
HD 108564	0442F	HD 112304-A0V	12	28	19.1200	−	16	54	39.771	−1.0	6.9	0.016	78.0	−0.8	0	0	0
HD 109443	0444F	HD 101122-A0V	12	34	46.732	−	23	28	32.20	−0.6	8.16	0.035	76.6	−1.0	0	0	0
HD 110885	0450F	HD 116960-A0V	12	45	19.2569	+	01	03	21.097	−1.06	7.38	0.016	−50.6	2.89	0	0	1
HD 111786	0453F	HD 114345-A0V	12	51	57.8954	−	26	44	17.783	−1.5	5.4	0.023	−8.6	1.09	0	1	0
HD 114038	0460F	HD 109309-A0V	13	07	53.8123	−	10	44	25.476	−0.02	2.72	0.041	34.6	1.89	0	0	0
HD 114606	0462F	HD 121996-A0Vs	13	11	21.4043	+	09	37	33.519	−0.53	7.09	0.000	13.2	−0.06	0	0	0
HD 114710	0463F	HD 107655-A0V	13	11	52.3937	+	27	52	41.453	0.05	2.92	0.013	57.2	0.09	0	0	0
HD 115589	0467F	HD 112304-A0V	13	18	13.5353	−	14	34	55.555	0.28	7.62	0.082	−45.2	−0.28	0	0	0
HD 115617	0468F	HD 119786-A0V	13	18	24.3142	−	18	18	40.304	0.02	2.96	0.000	7.3	−0.06	0	0	0
HD 116316	0471F	HD 121996-A0Vs	13	22	34.1508	+	26	06	56.513	−0.51	6.42	0.002	−59.3	0.31	0	0	0
HD 117200	0473F	HD 143187-B8V	13	27	04.6096	+	64	44	07.890	0.03	5.7	0.011	−71.6	0.88	0	0	0
HD 117176	0474F	HD 121996-A0Vs	13	28	25.8086	+	13	46	43.638	−0.1	3.5	0.000	23.6	0.38	0	0	0
HD 117635	0475F	HD 116960-A0V	13	31	39.9375	−	02	19	02.602	−0.42	5.31	0.000	−48.1	0.03	0	0	0
HD 117876	0476F	HD 121996-A0Vs	13	32	48.2137	+	24	20	48.280	−0.51	3.87	0.003	20.5	1.77	0	0	0
HD 118244	0479F	HD 121880-A0V	13	35	11.4174	+	22	29	59.031	−0.46	5.63	0.020	75.8	0.49	0	0	0
HD 119228	0481F	HD 118214-A0V	13	40	44.2733	+	54	40	53.889	−0.1	0.34	0.008	−11.4	3.09	1	0	0
HD 119288	0482F	HD 121996-A0Vs	13	42	12.7599	+	08	23	18.226	−0.23	5.11	0.000	−44.2	0.51	0	0	0
HD 120136	0485F	HD 116960-A0V	13	47	15.7434	+	17	27	24.855	0.24	3.51	0.000	30.0	−1.0	0	0	0
HD 120933	0487F	HD 122945-A0V	13	51	47.4753	+	34	26	39.261	−0.15	−0.01	0.113	−108.7	3.38	1	0	0
HD 121258	0490F	HD 119752-A0V	13	54	54.6217	−	26	00	56.758	−0.2	8.8	0.283	−29.9	−1.0	0	1	0
HD 125451	0504F	HD 121996-A0Vs	14	19	16.2803	+	13	00	15.479	0.01	4.39	0.000	12.6	0.57	0	0	0
BD+012916	0505F	HD 126129-A0V	14	21	45.2615	+	00	46	59.178	−1.86	6.47	0.03	−33.8	2.05	0	0	0
HD 126141	0506F	HD 121996-A0Vs	14	23	06.8213	+	25	20	17.433	−0.05	5.23	0.000	−6.0	0.53	0	0	0
HD 126053	0507F	HD 126129-A0V	14	23	15.2849	+	01	14	29.648	−0.37	4.64	0.000	3.3	−0.11	0	0	1
HD 126614	0511F	HD 132072-A0V	14	26	48.2807	−	05	10	40.007	0.52	7.06	0.055	−53.9	0.18	0	0	0
HD 126778	0512F	HD 127304-A0Vs	14	26	54.1638	+	28	35	20.423	−0.52	5.84	0.000	−125.1	2.01	0	0	0
HD 127243	0514F	HD 121409-A0V	14	28	37.8131	+	49	50	41.458	−0.78	3.16	0.060	41.2	1.9	0	1	1
BD+182890	0516F	HD 121996-A0Vs	14	32	13.4854	+	17	25	24.290	−1.54	7.74	0.020	84.5	1.34	0	0	0
HD 128959	0521F	HD 131885-A0V	14	40	43.3622	−	26	43	46.937	−0.51	7.57	0.050	17.1	0.82	0	0	0
HD 130095	0523F	HD 119752-A0V	14	46	51.2120	−	27	14	53.958	−1.7	7.8	0.068	112.6	1.31	0	0	0
HD 130322	0524F	HD 131951-A0V	14	47	32.724	−	00	16	53.32	0.12	6.23	0.025	−43.5	−0.26	0	0	0
HD 130817	0525F	HD 127304-A0Vs	14	49	06.7425	+	37	48	40.243	−0.29	5.08	0.013	−40.4	0.64	0	0	0
HD 130705	0526F	HD 131951-A0V	14	49	26.1554	+	10	02	38.965	0.34	3.95	0.000	−53.0	1.79	0	0	0
HD 132142	0529F	HD 121409-A0V	14	55	11.0434	+	53	40	49.260	−0.37	5.8	0.000	19.3	−0.38	0	0	0
HD 132475	0534F	HD 138813-A0V	14	59	49.7651	−	22	00	45.809	−1.37	6.91	0.000	143.4	0.49	0	0	0
BD+302611	0538F	HD 127304-A0Vs	15	06	53.8278	+	30	00	36.941	−1.45	6.09	0.01	−287.5	2.47	0	0	0

Table 2
(Continued)

Name	MILES ID	Standard Star	R.A. hh	mm	ss	+/−	Decl. dd	mm	ss	[Fe/H]	K_S (mag)	$E(B-V)$ (mag)	Velocity (km s^{-1})	log L_{bol} ($L_\odot$)	Q^1 Flag	P^2 Flag	S^3 Flag
HD 134063	0539F	HD 131951-A0V	15	07	15.4405	+	22	33	51.695	−0.69	5.47	0.019	−89.7	1.49	0	0	0
HD 134083	0540F	HD 131951-A0V	15	07	18.0660	+	24	52	09.101	−0.01	3.86	0.000	−9.4	0.47	0	0	0
HD 134169	0541F	HD 140775-A0V	15	08	18.0580	+	03	55	50.128	−0.81	6.16	0.000	4.5	0.4	0	1	0
HD 134440	0542F	HD 134013-A0V	15	10	12.9689	−	16	27	46.516	−1.34	7.19	0.000	322.2	−0.84	0	0	0
HD 134439	0543F	HD 134013-A0V	15	10	13.0880	−	16	22	45.860	−1.27	7.04	0.005	289.5	−0.71	0	0	1
HD 134987	0544F	HD 138295-A0V	15	13	28.6670	−	25	18	33.646	0.26	4.88	0.026	2.9	−1.0	0	0	0
HD 136064	0545F	HD 143187-B8V	15	14	38.3401	+	67	20	48.197	0.03	3.87	0.010	−47.0	0.58	0	0	0
HD 136202	0550F	HD 140755-A2	15	19	18.7971	+	01	45	55.468	0.05	4.01	0.030	33.5	0.61	0	1	0
HD 137391	0553F	HD 127304-A0Vs	15	24	29.4283	+	37	22	37.757	0.1	3.62	0.004	−603.0	−1.0	0	0	0
HD 137471	0555F	HD 140729-A0V	15	25	47.3975	+	15	25	40.930	−0.04	1.04	0.034	−28.7	3.07	0	0	0
HD 138290	0559F	HD 140729-A0V	15	30	55.4332	+	08	34	44.737	−0.1	5.66	0.015	−35.9	0.65	0	0	0
HD 138776	0562F	HD 140775-A0V	15	34	16.9188	−	02	43	26.643	0.35	7.11	0.069	7.0	0.17	0	0	0
HD 139641	0565F	HD 127304-A0Vs	15	37	49.5979	+	40	21	12.363	−0.51	3.1	0.020	20.7	1.31	0	0	0
BD+053080	0569F	HD 140775-A2	15	45	52.4015	+	05	02	26.558	−0.44	6.88	0.00	−17.9	−0.26	0	0	0
HD 142575	0574F	HD 140775-A0V	15	55	02.8379	+	05	04	12.148	−0.7	7.51	0.019	−55.0	0.9	0	0	0
HD 142703	0577F	HD 138062-A0V	15	56	33.3736	−	14	49	45.976	−1.1	5.34	0.036	9.2	0.86	0	1	0
HD 144585	0584F	HD 148968-A0V	16	07	03.3694	−	14	04	16.665	0.29	4.8	0.014	−45.1	0.28	0	0	0
HD 145148	0586F	HD 140755-A2	16	09	11.2145	+	06	22	43.302	0.1	3.68	0.000	−0.2	0.53	0	0	0
HD 145976	0589F	HD 145122-A0Vnn	16	12	45.4709	+	26	40	14.094	−0.02	5.48	0.018	−8.3	1.04	0	0	0
BD+112998	0598F	HD 140775-A0V	16	30	16.7825	+	10	59	51.748	−1.01	7.18	0.024	69.8	1.26	0	0	0
HD 149009	0603F	HD 164899-A0Vs	16	31	13.4310	+	22	11	43.649	0.09	2.04	0.075	−28.0	2.84	1	0	0
HD 150177	0611F	HD 159415-A0V	16	39	39.1298	−	09	33	16.512	−0.58	4.98	0.000	−46.7	0.6	0	0	0
HD 152601	0616F	HD 148968-A0V	16	54	35.6932	−	06	09	14.333	0.1	2.8	0.023	−45.0	1.65	0	0	0
HD 152781	0617F	HD 149134-A0V	16	56	01.8443	−	16	48	22.553	0.08	4.26	0.048	−19.3	0.79	0	0	1
HD 154733	0620F	HD 165029-A0V	17	06	18.0476	+	22	05	02.955	−0.09	2.48	0.018	−127.4	1.98	0	0	0
HD 155763	0621F	HD 143187-B8V	17	08	47.1959	+	65	42	52.863	−0.11	3.55	0.030	23.6	2.58	0	0	0
HD 155358	0622F	HD 157778-A0Vn	17	09	34.6174	+	33	21	21.085	−0.63	5.81	0.000	15.7	0.3	0	0	1
HD 157089	0628F	HD 161289-A0V	17	21	07.0556	+	01	26	34.988	−0.57	5.42	0.000	−133.8	0.26	0	0	0
HD 157881	0630F	HD 161289-A0V	17	25	45.2326	+	02	06	41.120	−0.01	4.37	0.000	−54.4	−0.95	0	0	0
HD 159482	0636F	HD 161289-A0V	17	34	43.0609	+	06	00	51.574	−0.75	6.79	0.004	−103.1	−0.02	0	0	1
HD 160693	0639F	HD 164899-A0Vs	17	39	36.8724	+	37	11	01.506	−0.56	6.9	0.000	23.7	0.06	0	0	1
HD 161149	0641F	HD 165029-A0V	17	43	22.0221	+	14	17	42.604	0.33	5.1	0.043	−53.5	−1.0	0	0	0
HD 162211	0648F	HD 165029-A0V	17	48	49.1464	+	25	37	22.329	−0.06	2.4	0.001	−42.5	1.65	0	0	0
HD 164349	0654F	HD 165029-A0V	18	00	03.4160	+	16	45	03.309	−0.01	1.94	0.001	−35.8	2.88	0	0	0
HD 166460	0667F	HD 161289-A0V	18	10	40.2995	+	03	19	27.325	−0.05	2.58	0.023	10.1	2.15	0	0	0
HD 170737	0679F	HD 174567-A0Vs	18	29	54.1103	+	26	39	26.247	−0.77	5.95	0.025	−110.8	0.88	0	0	0
HD 171496	0683F	HD 177213-A0V	18	36	07.4940	−	24	26	11.320	−0.73	5.59	0.151	−18.1	1.55	0	0	0
HD 173740	0690F	HD 172728-A0V	18	42	46.9665	+	59	37	36.347	−0.34	5.0	0.001	16.6	−2.06	0	0	0
HD 173819	0697F	HD 170654-A0V	18	47	28.9498	−	05	42	18.541	−0.67	2.16	0.260	19.3	4.27	1	0	0
HD 174912	0699F	HD 174567-A0Vs	18	51	25.1791	+	38	37	35.654	−0.45	5.68	0.000	3.3	0.03	0	0	0
HD 175535	0703F	CCDM J19302+5639AB-A0V	18	53	13.5416	+	50	42	29.585	−0.07	2.82	0.007	−18.6	2.25	0	0	0
HD 175588	0704F	HD 174567-A0Vs	18	54	30.2833	+	36	53	55.013	−0.14	−1.25	0.000	−27.0	4.06	0	0	1
HD 175640	0706F	HD 171149-A0Vn	18	56	22.6604	−	01	47	59.505	0.17	6.25	0.044	24.4	1.84	0	0	0
NGC6791-R4	0940C	HD 174567-A0Vs	19	20	49.7000	+	37	43	41.2	0.42	7.82	0.119	−45.5	2.78	0	0	0
NGC6791-R19	0943C	HD 174567-A0Vs	19	20	52.8000	+	37	44	26.900	0.42	10.19	0.119	−41.2	2.03	0	0	0
HD 182572	0721F	HD 182761-A0V	19	24	58.2002	+	11	56	39.886	0.34	3.04	0.031	608.6	−1.0	0	0	0
CD-2415398	0723F	HD 177120-A0V	19	32	20.7821	−	23	51	12.755	−1.17	9.06	0.097	17.7	3.17	0	0	1

Table 2
(Continued)

Name	MILES ID	Standard Star	R.A. hh	mm	ss	+/−	Decl. dd	mm	ss	[Fe/H]	K_S (mag)	$E(B-V)$ (mag)	Velocity (km s^{-1})	log L_{bol} ($L_\odot$)	Q^1 Flag	P^2 Flag	S^3 Flag
HD 184499	0726F	HD 174567-A0Vs	19	33	27.0812	+	33	12	06.716	−0.54	5.08	0.000	−123.8	0.31	0	0	1
HD 185657	0730F	HD 178207-A0Vn	19	37	56.7133	+	49	17	03.902	−0.19	4.09	0.000	−55.6	1.74	0	0	0
HD 186408	0733F	HD 194354-A0Vs	19	41	48.9534	+	50	31	30.215	0.08	4.43	0.000	−54.8	0.2	1	0	0
M71_1-77	0967C	* 5 Vul-A0V	19	53	37.4000	−	1	−1	−1	−0.22	12.11	0.270	26.4	1.58	1	0	0
M71_I	0971C	* 5 Vul-A0V	19	53	44.6000	+	18	46	35.0000	−0.78	8.66	0.270	−9.0	2.71	0	0	0
HD 188510	0742F	HD 182919-A0V	19	55	09.6783	+	10	44	27.372	−1.43	7.13	0.000	−134.7	−0.39	0	1	0
HD 189558	0747F	HD 182678-A0V	20	01	00.2457	−	12	15	20.340	−1.04	6.16	0.000	−1.6	0.47	0	0	0
HD 190360	0749F	HD 192538-A0V	20	03	37.4058	+	29	53	48.494	0.21	4.08	0.000	−55.4	0.01	0	0	0
HD 190178	0752F	HD 195549-A0V	20	04	49.4677	−	28	16	25.164	−0.66	8.07	0.002	22.8	0.64	0	0	0
HD 191046	0755F	HD 192538-A0V	20	06	28.9887	+	36	13	35.918	−0.75	4.19	0.040	−84.5	2.5	0	0	1
HD 345957	0757F	HD 182919-A0V	20	10	48.1619	+	23	57	54.514	−1.2	7.36	0.000	−74.7	0.35	0	0	0
HD 192640	0759F	HD 192538-A0V	20	14	32.0333	+	36	48	22.692	−0.8	4.42	0.026	−0.6	1.18	0	0	0
HD 192909	0760F	HD 199217-A0V	20	15	28.3228	+	47	42	51.160	−0.02	0.16	0.016	−61.8	3.78	1	0	0
HD 196755	0768F	HD 198070-A0Vn	20	39	07.7843	+	10	05	10.338	−0.02	3.61	0.014	−85.0	0.76	0	0	0
BD+044551	0777F	HD 198070-A0Vn	20	48	50.7212	+	05	11	58.801	−1.26	8.25	0.00	−82.7	1.63	1	0	0
HD 199191	0779F	HD 205314-A0V	20	53	18.3149	+	54	31	05.164	−0.7	4.73	0.010	−207.3	1.54	0	0	0
HD 200527	0782F	HD 201076-A0V	21	02	24.1998	+	44	47	27.523	−0.07	1.09	0.000	−9.7	3.21	0	0	0
HD 200779	0785F	HD 210501-A0V	21	05	19.7452	+	07	04	09.477	0.02	5.31	0.003	−47.6	−0.76	0	0	0
HD 201891	0790F	HD 208108-A0Vs	21	11	59.0315	+	17	43	39.890	−1.05	5.93	0.000	−86.8	0.03	0	0	0
HD 201889	0791F	HD 210501-A0V	21	11	59.5235	+	24	10	05.389	−0.74	6.43	0.000	−83.9	0.31	0	0	1
HD 203638	0795F	HD 202025-A0V	21	24	09.5924	−	20	51	06.740	0.12	2.69	0.010	6.4	1.7	0	0	0
HD 204041	0796F	HD 198070-A0Vn	21	25	51.5837	+	00	32	03.620	−0.44	5.96	0.025	29.3	0.96	0	1	0
HD 204155	0798F	HD 20722-A0 D	21	26	42.9055	+	05	26	29.902	−0.69	7.01	0.000	−49.5	0.31	0	0	0
HD 204613	0799F	HD 205314-A0V	21	27	42.9678	+	57	19	18.861	−0.38	6.79	0.008	−102.9	0.33	0	0	0
HD 204587	0804F	HD 203893-A0V	21	30	02.7541	−	12	30	36.255	−0.11	5.88	0.004	−86.4	−0.86	0	0	0
HD 205153	0806F	HD 202941-A0V	21	34	09.1873	−	27	54	04.333	0.07	6.83	0.025	−27.5	0.97	0	0	0
HD 205512	0807F	HD 209932-A0V	21	34	46.5638	+	38	32	02.604	0.03	2.6	0.000	−108.5	1.69	0	0	0
HD 206078	0808F	HD 201184-A0V	21	37	10.4225	+	62	18	15.283	−0.59	4.72	0.002	−120.4	1.61	0	1	0
HD 206453	0811F	HD 201184-A0V	21	42	39.5071	−	18	51	58.766	−0.41	2.55	0.033	40.2	−1.0	1	0	0
HD 207222	0818F	HD 208108-A0Vs	21	46	56.2591	+	21	17	50.768	−0.36	8.37	0.057	−7.0	1.11	0	0	0
HD 210295	0825F	HD 215143–B7.5V	22	09	41.4440	−	13	36	19.478	−1.26	7.18	0.000	−23.9	0.98	0	0	0
HD 211075	0830F	HD 208108-A0Vs	22	14	20.0378	+	18	01	13.370	−0.42	5.22	0.016	33.5	2.14	1	1	0
HD 213042	0835F	HD 220455-A0V	22	29	15.2354	−	30	01	06.271	0.12	5.11	0.076	13.5	−0.63	0	0	0
HD 216174	0845F	HD 219290-A0V	22	49	46.3148	+	55	54	09.999	−0.61	2.63	0.030	−47.4	2.03	0	0	0
HD 216131	0846F	BD+3904890-A0V	22	50	00.1931	+	24	36	05.698	−0.07	1.18	0.000	87.9	1.69	0	0	0
HD 217107	0855F	HD 215143-B7.5V	22	58	15.5411	−	02	23	43.384	0.33	4.54	0.019	10.9	0.01	0	0	0
HD 218640	0861F	HD 223352-A0Vnp	23	09	54.896	−	22	27	27.44	0.36	2.95	0.021	25.0	−1.0	0	0	0
HD 219449	0867F	HD 219833-A0V	23	15	53.4948	−	09	05	15.854	0.03	1.6	0.000	−22.1	1.78	0	1	0
HD 219623	0868F	HD 211301-A0V	23	16	42.3033	+	53	12	48.510	0.07	4.31	0.000	17.0	0.1	0	0	1
HD 219615	0870F	HD 215143-B7.5V	23	17	09.9374	+	03	16	56.238	−0.57	1.39	0.000	1.8	1.81	0	0	1
HD 219734	0871F	HD 219290-A0V	23	17	44.6471	+	49	00	55.081	−0.04	0.51	0.019	12.1	3.08	0	0	0
HD 219978	0873F	HD 223386-A0V	23	19	23.7734	+	62	44	23.185	0.18	0.79	0.228	−27.4	3.92	0	1	0
HD 220009	0874F	HD 210501-A0V	23	20	20.5831	+	05	22	52.701	−0.8	1.99	0.000	85.4	2.43	0	1	0
HD 221148	0881F	HD 215143-B7.5V	23	29	32.0820	−	04	31	57.891	0.34	3.89	0.000	0.5	0.8	0	0	0
HD 221377	0883F	HD 219290-A0V	23	31	19.7259	+	52	24	38.504	−0.6	6.37	0.005	37.3	0.64	0	0	0
HD 221830	0886F	HD 210501-A0V	23	35	28.8937	+	31	01	01.830	−0.4	5.3	0.000	−71.4	0.2	0	0	0
G171-010	0890F	HD 219290-A0V	23	41	54.989	+	44	10	40.78	0.09	5.93	0.088	−36.3	−2.62	0	0	0

Table 2
(Continued)

Name	MILES ID	Standard Star	R.A. hh	mm	ss	+/−	Decl. dd	mm	ss	[Fe/H]	K_S (mag)	$E(B-V)$ (mag)	Velocity (km s^{-1})	log $L_{\rm bol}$ ($L_\odot$)	Q^1 Flag	P^2 Flag	S^3 Flag
HD 223524	0893F	HD 219833-A0V	23	50	14.7298	−	09	58	26.893	0.02	3.22	0.013	2.5	1.67	0	0	0
HD 224458	0895F	HD 006457-A0Vn	23	58	06.2501	+	29	58	35.906	−0.44	5.73	0.050	−114.2	1.55	0	0	0

Note. The quality, parameter, and shape flags are indicators of how good the spectra are. A star marked with "1" in any of those categories might have some issue: (1) The IRTF spectra are unacceptably noisy, (2) the stellar parameters seem inconsistent with the data, (3) something may be wrong with the flux calibration that is causing issues with the spectral shape.

References

Allard, F., Hauschildt, P. H., Alexander, D. R., & Starrfield, S. 1997, ARA&A, 35, 137
Allard, F., Homeier, D., Freytag, B., et al. 2013, MSAIS, 24, 128
Ardila, D. R., Van Dyk, S. D., Makowiecki, W., et al. 2010, ApJS, 191, 301
Athey, A., Bregman, J., Bregman, J., Temi, P., & Sauvage, M. 2002, ApJ, 571, 272
Beifiori, A., Maraston, C., Thomas, D., & Johansson, J. 2011, A&A, 531, A109
Bertone, E., Buzzoni, A., Chávez, M., & Rodríguez-Merino, L. H. 2008, A&A, 485, 823
Brott, I., & Hauschildt, P. H. 2005, in ESA Special Publication 576, The Three-Dimensional Universe with Gaia, ed. C. Gaia, K. S. Turon, & M. A. C. O'Flaherty, 565
Cappellari, M., & Emsellem, E. 2004, PASP, 116, 138
Castelli, F., & Kurucz, R. L. 2003, in IAU Symp. 210, Modelling of Stellar Atmospheres, ed. N. Piskunov, W. W. Weiss, & D. F. Gray (San Francisco, CA: ASP), A20
Cenarro, A. J., Gorgas, J., Cardiel, N., et al. 2001, MNRAS, 326, 981
Cenarro, A. J., Peletier, R. F., Sánchez-Blázquez, P., et al. 2007, MNRAS, 374, 664
Chen, Y.-P., Trager, S. C., Peletier, R. F., et al. 2014, Msngr, 158, 30
Choi, J., Dotter, A., Conroy, C., et al. 2016, ApJ, 823, 102
Clough, S. A., Shephard, M. W., Mlawer, E. J., et al. 2005, JQSRT, 91, 233
Coelho, P., Barbuy, B., Meléndez, J., Schiavon, R. P., & Castilho, B. V. 2005, A&A, 443, 735
Cohen, J. G. 1978, ApJ, 221, 788
Conroy, C. 2013, ARA&A, 51, 393
Conroy, C., & van Dokkum, P. G. 2012, ApJ, 760, 71
Cushing, M. C., Vacca, W. D., & Rayner, J. T. 2004, PASP, 116, 362
Diaz, A. I., Terlevich, E., & Terlevich, R. 1989, MNRAS, 239, 325
Dries, M., Trager, S. C., & Koopmans, L. V. E. 2016, MNRAS, 463, 886
Emsellem, E., Cappellari, M., Peletier, R. F., et al. 2004, MNRAS, 352, 721
Fitzpatrick, E. L., & Massa, D. 2007, ApJ, 663, 320
Foreman-Mackey, D., Hogg, D. W., Lang, D., & Goodman, J. 2013, PASP, 125, 306
France, K., Shkolnik, E., Linsky, J., et al. 2015, arXiv:1505.01840
Frogel, J. A., Persson, S. E., Matthews, K., & Aaronson, M. 1978, ApJ, 220, 75
González Hernández, J. I., & Bonifacio, P. 2009, A&A, 497, 497
Goodman, J., & Weare, J. 2010, Commun. Appl. Math. Comput. Sci., 5, 65
Gorgas, J., Faber, S. M., Burstein, D., et al. 1993, ApJS, 86, 153
Gregg, M. 2001, A Next Generation Spectral Library of Stars, HST Proposal, #9088
Grundahl, F., Clausen, J. V., Hardis, S., & Frandsen, S. 2008, A&A, 492, 171
Gunn, J. E., & Stryker, L. L. 1983, ApJS, 52, 121
Gustafsson, B., Edvardsson, B., Eriksson, K., et al. 2003, in ASP Conf. Ser. 288, Stellar Atmosphere Modeling, ed. I. Hubeny, D. Mihalas, & K. Werner (San Francisco, CA: ASP), 331
Harris, W. E. 1996, AJ, 112, 1487
Høg, E., Fabricius, C., Makarov, V. V., et al. 2000a, A&A, 357, 367
Høg, E., Fabricius, C., Makarov, V. V., et al. 2000b, A&A, 355, L27
Hunter, J. D. 2007, CSE, 9, 90
Ivanov, V. D., Rieke, M. J., Engelbracht, C. W., et al. 2004, ApJS, 151, 387
Jones, E., Hauschildt, T., Peterson, P., et al. 2001, SciPy: Open source scientific tools for Python, http://www.scipy.org/
Jones, L. 1999, PhD thesis, Univ. North Carol
Kausch, W., Noll, S., Smette, A., et al. 2015, A&A, 576, A78
Kleinmann, S. G., & Hall, D. N. B. 1986, ApJS, 62, 501
Koleva, M., Prugniel, P., Bouchard, A., & Wu, Y. 2009, A&A, 501, 1269
Lançon, A., & Wood, P. R. 2000, A&As, 146, 217
Lanz, T., & Hubeny, I. 2003, ApJS, 146, 417
Le Borgne, J.-F., Bruzual, G., Pelló, R., et al. 2003, A&A, 402, 433
Lind, K., Bergemann, M., & Asplund, M. 2012, MNRAS, 427, 50
Lord, S. D. 1992, NASA Technical Memorandum, 103957
Magic, Z., Collet, R., Hayek, W., & Asplund, M. 2013, A&A, 560, A8
Mann, A. W., Feiden, G. A., Gaidos, E., Boyajian, T., & von Braun, K. 2015, ApJ, 804, 64
Mármol-Queraltó, E., Cardiel, N., Cenarro, A. J., et al. 2008, A&A, 489, 885
Martini, P., Dicken, D., & Storchi-Bergmann, T. 2013, ApJ, 766, 121
Martins, L. P., & Coelho, P. 2007, MNRAS, 381, 1329
Martins, L. P., González Delgado, R. M., Leitherer, C., Cerviño, M., & Hauschildt, P. 2005, MNRAS, 358, 49
Meneses-Goytia, S., Peletier, R. F., Trager, S. C., et al. 2015, A&A, 582, A96
Munari, U., Sordo, R., Castelli, F., & Zwitter, T. 2005, A&A, 442, 1127
Ness, M., Hogg, D. W., Rix, H.-W., Ho, A. Y. Q., & Zasowski, G. 2015, ApJ, 808, 16
Newton, E. R., Charbonneau, D., Irwin, J., et al. 2014, AJ, 147, 20
Percival, S. M., & Salaris, M. 2009, ApJ, 703, 1123
Pickles, A. J. 1985, ApJS, 59, 33
Pickles, A. J. 1998, PASP, 110, 863
Prugniel, P., & Soubiran, C. 2001, A&A, 369, 1048
Prugniel, P., Vauglin, I., & Koleva, M. 2011, A&A, 531, A165
Rajpurohit, A. S., Reylé, C., Allard, F., et al. 2014, A&A, 564, A90
Rajpurohit, A. S., Reyle, C., Allard, F., et al. 2016, arXiv:1401.2901
Rayner, J. T., Cushing, M. C., & Vacca, W. D. 2009, ApJS, 185, 289
Rayner, J. T., Toomey, D. W., Onaka, P. M., et al. 2003, PASP, 115, 362
Astropy Collaboration, Robitaille, T. P., Tollerud, E. J., et al. 2013, A&A, 558, A33
Röck, B., Vazdekis, A., Ricciardelli, E., et al. 2016, A&A, 589, A73
Sánchez-Blázquez, P., Peletier, R. F., Jiménez-Vicente, J., et al. 2006, MNRAS, 371, 703
Schiavon, R. P. 2007, ApJS, 171, 146
Sharma, K., Prugniel, P., & Singh, H. P. 2016, A&A, 585, A64
Sharon, C., Hillenbrand, L., Fischer, W., & Edwards, S. 2010, AJ, 139, 646
Silva, D. R., & Cornell, M. E. 1992, ApJS, 81, 865
Simonian, G. V., & Martini, P. 2016, arXiv:1603.09345
Skrutskie, M. F., Cutri, R. M., Stiening, R., et al. 2006, AJ, 131, 1163
Spiniello, C., Trager, S. C., Koopmans, L. V. E., & Chen, Y. P. 2012, ApJL, 753, L32
Spinrad, H. 1962, ApJ, 135, 715
Thomas, D., Maraston, C., & Bender, R. 2003, MNRAS, 339, 897
Trager, S. C., Faber, S. M., Worthey, G., & González, J. J. 2000, AJ, 120, 165
Vacca, W. D., Cushing, M. C., & Rayner, J. T. 2003, PASP, 115, 389
Valdes, F., Gupta, R., Rose, J. A., Singh, H. P., & Bell, D. J. 2004, ApJS, 152, 251
van Dokkum, P. G., & Conroy, C. 2012, ApJ, 760, 70
Vazdekis, A., Cenarro, A. J., Gorgas, J., Cardiel, N., & Peletier, R. F. 2003, MNRAS, 340, 1317
Vazdekis, A., Koleva, M., Ricciardelli, E., Röck, B., & Falcón-Barroso, J. 2016, MNRAS, 463, 3409
Vazdekis, A., Sánchez-Blázquez, P., Falcón-Barroso, J., et al. 2010, MNRAS, 404, 1639
Villaume, A., Conroy, C., & Johnson, B. D. 2015, ApJ, 806, 82
Wing, R. F., & Ford, W. K., Jr. 1969, PASP, 81, 527
Worthey, G., Faber, S. M., Gonzalez, J. J., & Burstein, D. 1994, ApJS, 94, 687
Wu, Y., Singh, H. P., Prugniel, P., Gupta, R., & Koleva, M. 2011, A&A, 525, A71